

**UCSF**

**UC San Francisco Electronic Theses and Dissertations**

**Title**

Development of Improved 1H Magnetic Resonance Spectroscopic Imaging Techniques for Brain Tumor Patients

**Permalink**

<https://escholarship.org/uc/item/6pj385k0>

**Author**

Osorio, Joseph Anthony

**Publication Date**

2007-09-13

Peer reviewed|Thesis/dissertation

Development of Improved  $^1\text{H}$  Magnetic Resonance Spectroscopic Imaging  
Techniques for Brain Tumor Patients

by

Joseph Anthony Osorio

DISSERTATION

Submitted in partial satisfaction of the requirements for the degree of

DOCTOR OF PHILOSOPHY

in

Bioengineering

in the

GRADUATE DIVISION

of the

UNIVERSITY OF CALIFORNIA, SAN FRANCISCO

AND

UNIVERSITY OF CALIFORNIA, BERKELEY

UMI Number: 3274655



---

UMI Microform 3274655

Copyright 2007 by ProQuest Information and Learning Company.  
All rights reserved. This microform edition is protected against  
unauthorized copying under Title 17, United States Code.

---

ProQuest Information and Learning Company  
300 North Zeeb Road  
P.O. Box 1346  
Ann Arbor, MI 48106-1346

Copyright 2007

by

Joseph Anthony Osorio

Dedicated to  
Josefina Diaz  
and  
Robert Osorio

## Acknowledgements

To Sarah Nelson, for being such an amazing mentor, guiding me as a student and treating my opinions as a peer, always being so consistent as a wonderful boss, and for being extremely supportive and instrumental throughout my years as a graduate student,

to Rich Cohen, Nathaniel Beyor, Albert Pofu Chen, Meredith Metcalf, Sapun Parek, for great roommates, friends, and best of all - support outside of the lab for the past five years – HAPPY GRAD SCHOOL!,

to Duan Xu, for always supporting and advising me not only during quals but also throughout my research,

to Janine Lupo, Esin Ozturk-Isik, Inas Khayal, and Yan Li, for being great people to sit next to all these years at work,

to Jason Crane, Radhika Srinivasan, Ilwoo Park, Rebeca Choy, Forrest Crawford, Suja Saraswathy, Pieter Pels, Kate Hammond, Paul Di Camillo, Pamela Jackson, Helene Ratiney, Matt Zierhut, Colleen McGue and Wei Bian, for creating a friendly and peaceful yet fun work environment,

to Roland Krug, Julio Gamio-Caraballido, Cornelius von Morze, Suchandrima Banerjee, and Jeffrey Berman, for their help in various steps of my study and friendship,

to Annette Chan, Michael Lee, Joonmi Oh, Xiaojuan Li, for helping me adjust to my new lab with their warm welcome and support,

to Chuck Cunningham, Sue Noworolski, and John Pauly for all of their amazing help in pulse design and helpful preparation during my qualifying exam and thesis project,

to Sharmila Majumdar and Soonmee Cha, for sitting in my quals committee and reading my thesis always with a positive attitude and smile,

to Dan Vigneron, for being my academic advisor in the Bioengineering program and chairing in my qualifying exam,

to John Kurhanewicz and Marian Diamond, for teaching me about MR spectroscopy and anatomy, for their discussions during my qualifying exam preparation, and participating in my quals committee,

to Andrea Pirzkall and Susan Chang, for their help with clinical questions, useful discussions, and support,

to Bert Jimenez , Niles Bruce, and Evelyn Proctor, for their help in making the patient scans possible,

to Fady Semaan, Marvin Attallah, Chris Mora, Mike Sooter, for being amazing best friends outside of school – your support was instrumental,

to my parents, Josefina Diaz and Robert Osorio, for their love, encouragement and support,

to my brother Bob and his wife Sandra, for their love, if I wouldn't have had family in San Francisco – it wouldn't have been possible, and of course all the wonderful dinners,

to my brother Chicky and his wife Lisa, for your love, support, encouragement and keeping the flamenco guitar a part of my life,

to my sister Elisa and her husband Bob, for their love, for always keeping such a strong interest in my progress, and our daily conversations,

to my sister Jessica and her husband Jose, for their love, the amazing vacations, the baseball games, and never hesitating support,

to Anthony, Andrew, Jessica, Gabriela, Aubriana, Jose Jr., Robby, Jonathan, Aleksandra, Caden, Alijah, -- the most amazing nieces and nephews ever, you are what puts a smile on my face - daily,

THANK YOU ALL VERY MUCH – IT WOULD HAVE NEVER BEEN POSSIBLE WITHOUT ALL YOU!

Grant funding for this thesis project was provided by the NIGMS grant R25 GM56847 and the UC Discovery grants LSIT01-10107 and ITL-BIO04-10148 funded in conjunction with GE Healthcare, and NIH grants R01 CA059880, P50 CA97257 and P50 CA9729.



# **Abstract**

## **Development of Improved 1H Magnetic Resonance Spectroscopic Imaging Techniques for Brain Tumor Patients**

**by**

**Joseph Anthony Osorio**

Magnetic resonance spectroscopic imaging (MRSI) is one of the most technically demanding areas of magnetic resonance imaging. To achieve the necessary performance, current methods employ many of the recent advances in RF pulse design. Extending MRSI methods to higher field strength poses a number of additional challenges, along with a wealth of opportunity, related to the design and use of RF pulses. With the availability of 3 T whole body clinical scanners, the potential exist for improving signal-to-noise ratio (SNR), spatial resolution and/or reduction of scan-time. Brain MRSI exams are a useful clinical tool for treatment planning and monitoring glial disease, but an overriding challenge has been the amount of coverage that could be achieved using this technique.

MR spectroscopic imaging was utilized to study the biochemical changes over time, and evaluate how these changes related to conventional imaging methods, in a population of low-grade glioma patients at 1.5 T. Although we were able to note unique metabolic changes in brain cancer tissue, the study ultimately was limited by SNR and coverage.

In order to potentially address the limitations in SNR observed at 1.5-T, MRSI was implemented at 3 T. The results demonstrated the acquisition of

clinically acceptable spectra from brain tumor patients that were representative of the population encountered routinely in clinical practice. The improvements in sensitivity could be utilized either to detect more subtle differences in metabolite levels, or to reduce the spatial resolution.

Previously observed limitations in spatial coverage led to the design of the cosine-modulated very selective suppression (CM-VSS) pulse. This pulse design was not only optimized for improved coverage at 3 T, but it was also designed to allow more saturation bands in a shorter time period. With CM-VSS pulses, MRSI could now be feasibly acquired from almost all brain tissue.

The results of this dissertation demonstrate improvements in MRSI techniques that allow for better spatial characterization of brain tumors. It is expected that these improvements in data quality and tumor coverage will result in increased usage of MRSI sequences in clinical settings, and improved evaluation of brain tumor biochemistry.

Approved by Sarah J. Nelson, Ph.D.

---

Date

# Table of Contents

<b>Chapter 1: Introduction</b>	<b>1</b>
<b>Chapter 2: Background I: Brain Tumors</b>	<b>5</b>
<b>2.1 Neuroepithelial Tumors</b>	<b>5</b>
<b>2.2 Infiltrative Gliomas</b>	<b>6</b>
Astrocytic Tumors	6
Oligodendroglioma and Mixed Tumors	7
<b>2.3 Clinical Presentation of Neoplasms</b>	<b>8</b>
<b>2.4 Treatment of Neoplasms</b>	<b>8</b>
Surgical Therapy	8
Radiation Treatment	9
Systemic Chemotherapy	9
<b>2.5 Clinical Imaging of Neoplasms</b>	<b>12</b>
Tumor Detection	14
<b>Chapter 3: Background II: MR Spectroscopy</b>	<b>17</b>
<b>3.1 Magnetic Resonance Spectroscopy</b>	<b>17</b>
Physics of Magnetic Resonance Spectroscopy	17
Single Voxel Spectroscopy	19
<b>3.2 Chemical Shift Imaging</b>	<b>19</b>
MRS Localization Procedures	20
Volume Excitation	20
Water Suppression	22
Outer Volume Suppression	25
MRSI of Brain Neoplasms	30
<b>Chapter 4: Serial assessment of therapy response for low-grade glioma patients through MR diffusion, perfusion, spectroscopic, and anatomical imaging at 1.5 Tesla</b>	<b>33</b>
<b>4.1 Low Grade Glioma Background</b>	<b>33</b>
<b>4.2 Methods</b>	<b>34</b>
Patient Population	34
Treatment	34
MR Data Acquisition	35
MR Data Post-Processing	38
<b>4.3 Results</b>	<b>40</b>
Pre-Therapy	40
Follow-Up	41
<b>4.4 Discussion</b>	<b>43</b>
<b>Chapter 5: 3D <sup>1</sup>H MRSI of Brain Tumors at 3.0 Tesla using an 8-Channel Phased Array Head Coil</b>	<b>45</b>

<b>5.1 Background</b>	<b>45</b>
<b>5.2 Study Population</b>	<b>47</b>
Conventional MRI	48
<sup>1</sup> H MRSI Acquisition	48
1H MRSI Reconstruction	50
1H MRSI Volume Segmentation	52
In Vivo Metabolite Measurements	53
<b>5.3 Results</b>	<b>54</b>
Lipid Contamination	58
Metabolite Ratios	58
Abnormality Index (CNI)	60
Signal-to-Noise Ratio (SNR)	62
<b>5.4 Discussion</b>	<b>64</b>
<b>Chapter 6: Design of cosine-modulated very selective suppression pulses for 3D <sup>1</sup>H MRSI at 3.0 Tesla</b>	<b>67</b>
<b>6.1 Background</b>	<b>67</b>
<b>6.2 Methods</b>	<b>68</b>
Pulse Design	68
Data Acquisition	72
<b>6.3 Results and Discussion</b>	<b>73</b>
CM-VSS Pulse Scheme	73
Volunteer Data	75
<b>6.4 Conclusions</b>	<b>79</b>
<b>Chapter 7: Improved coverage of brain tumors with 1H MRSI using Cosine Modulated Very Selective Suppression Pulses at 3T.</b>	<b>81</b>
<b>7.1 Background</b>	<b>81</b>
<b>7.2 Methods</b>	<b>83</b>
Cosine Modulated VSS Pulse	83
Data Acquisition	83
Octagon Excitation using CM-VSS	84
Brain Tumor Coverage with Conventional VSS	86
Brain Tumor Patients with CM-VSS	87
<b>7.3 Results and Discussion</b>	<b>88</b>
Retrospective MRSI on Patient Data	88
CM-VSS Pulses in Brain Tumors	89
Brain Tumor – Maximum Coverage	90
Two- versus Three Dimensional Acquisition	91
<b>Chapter 8: Summary</b>	<b>94</b>
<b>References</b>	<b>96</b>

## List of Tables

Table 4.1. Patient treatment demographics_____	35
Table 4.2. Pretreatment T2 volumes, CNI volumes, and ADC values _____	41
Table 5.1. Acquisition times, number of excitations, and voxel sizes _____	50
Table 5.2. Signal-to-Noise ratio of metabolite levels_____	64
Table 6.1. Timing comparison for CM-VSS pulse scheme _____	74
Table 6.2. SNR comparison between CM-VSS and conventional pulse _____	78
Table 7.1. Retrospective analysis in conventional-MRSI coverage _____	89
Table 7.2. MRSI coverage in three tumor patients _____	89

## List of Figures

Figure 2.1: Schematic of cell cycle _____	11
Figure 2.2: Conventional anatomical imaging of a brain tumor _____	14
Figure 2.3: T1- image depicting regions of varying image signal intensity_	15
Figure 2.4: T2- image depicting regions of varying image signal intensity_	16
Figure 3.1: Schematic of a MR spectroscopy pulse sequence _____	21
Figure 3.2: Pulse sequence timing diagram for a PRESS MRS _____	22
Figure 3.3: Schematic example of unsuppressed water and lipid _____	23
Figure 3.4: CHES imaging sequence _____	24
Figure 3.5: Impact of varying amounts of water suppression_____	25
Figure 3.6: Spatial saturation bands around MRSI slices _____	26
Figure 3.7: Pulse timing sequence of outer volume suppression _____	27
Figure 3.8: Very selective suppression pulse_____	28
Figure 3.9: Example data set showing the efficacy of the VSS pulse _____	29
Figure 3.10: In vivo data example of outer volume suppression _____	30
Figure 3.11: In vivo magnetic resonance spectroscopic imaging _____	32
Figure 4.1: Serial time points for scan acquisitions_____	35
Figure 4.2: Conventional anatomic FLAIR and functional MR maps _____	36
Figure 4.3: FLAIR and MRSI of low-grade oligodendroglioma _____	37
Figure 4.4: FLAIR serial images of low-grade oligodendroglioma _____	38
Figure 4.5: Abnormal T2 region manual contours _____	39
Figure 4.6: Serial FLAIR images with ADC maps_____	42
Figure 4.7: Serial spectra for patient with low-grade glioma _____	43
Figure 5.1: Phantom data for a single voxel from all coil receptions _____	51

Figure 5.2: Metabolite maps of NAA peak amplitude_____	52
Figure 5.3: Example 1H MRSI data from a grade IV glioma patient _____	56
Figure 5.4: Axial multiple 1H MRSI arrays from a patient_____	57
Figure 5.5: Coronal multiple 1H MRSI arrays from a patient _____	59
Figure 5.6: Multiple 1H MRSI arrays from a grade II patient _____	61
Figure 5.7: Regional analysis of metabolic ratios _____	62
Figure 6.1: VSS RF pulse prior- to, and post- cosine-modulation_____	69
Figure 6.2: OVS section of the MRSI pulse sequence _____	71
Figure 6.3: Phantom image acquisition utilizing CM-VSS pulses_____	72
Figure 6.4: Demonstration of the functionality of the CM-VSS pulse _____	75
Figure 6.5: In vivo volunteer data with four VSS pulses_____	76
Figure 6.6: Normal volunteer with cosine modulated PRESS MRSI_____	77
Figure 6.7: MRSI data acquired with CM-VSS and conventional _____	79
Figure 7.1: Illustration demonstrating a common tumor location_____	82
Figure 7.2: Octagon configuration control variable _____	85
Figure 7.3: Phantom images acquired using the control variable _____	86
Figure 7.4: Illustrating the various approaches for utilizing the CM-VSS ____	87
Figure 7.5: Brain tumor patient with 1H MRSI using CM-VSS_____	90
Figure 7.6: Patient with grade IV glioma. Five slices of CM-VSS data _____	93

## Chapter 1: Introduction

---

Gliomas are a type of primary brain tumor that cause the third most common cancer related death in people under the age of 35. Originating from glia, the support cells for neurons, they are extremely heterogeneous, ranging from benign to highly malignant lesions. Although gliomas rarely metastasize, they are highly infiltrative in nature and typically recur within a 2-3cm margin of the original lesion (1).

Understanding the underlying biological makeup and survival mechanism of glial tumors could potentially help researchers monitor and tailor therapies for individual patients that would spare the potentially toxic effects of agents, and could have a profound prognostic impact. Typical treatment for glioma patients involves a subtotal or gross total resection, chemotherapy, and/or radiation therapy. These treatments directly affect the tissue environment and cause changes that will have an affect upon the conventional imaging. Conventional magnetic resonance imaging (MRI) examinations for glioma patients consist of  $T_1$ -weighted images, with pre- and post- injection of a paramagnetic contrast agent, and  $T_2$ -weighted images. Unfortunately, conventional MRI techniques are not able to fully characterize differences in tumor types, disease progression, and effectiveness of therapy; therefore interpretation of these data becomes highly subjective. The need clearly exists for additional techniques that may



add insight about the functional properties of the underlying changes in the tumor biology (2).

Magnetic resonance spectroscopic imaging (MRSI) is a functional *in vivo* technique capable of identifying regions of tissue that exhibit abnormal metabolism, and therefore provides additional information that is not usually seen with conventional MRI. MRSI emerges from the fact that proton ( $^1\text{H}$ ) spins within varying chemical environments experience different chemical shielding that result in variations in precession frequency, a phenomenon known as chemical shift. MRSI has been shown to provide vital information about the spatial extent and degree of metabolic activity of gliomas both within the contrast enhancing volume and in surrounding areas of hyperintensity on the  $T_2$ -weighted images (1-3). MRSI is currently limited in its ability to cover the spatial extent of the entire lesion, its relatively coarse spatial resolution, and long acquisition times. The challenge in overcoming these obstacles originates from either the lesion lying close to the edge of the brain, limited signal-to-noise ratio, or the typical field of view being smaller than the size of the head. The latter manifests in subcutaneous lipids being aliased into the brain tissue, therefore contaminating voxels in the entire spectral array. These problems often make it impossible to acquire spectra from the entire lesion. VSS pulses were created to eliminate unwanted lipid signals, and provide selective suppression to exclude unwanted regions (4). These pulses have proven to be extremely valuable, but are currently limited in the number that can be played out within the pulse sequence. These constraints still make it difficult to conform the

acquisition to irregular shaped lesions and examine regions that are close to subcutaneous lipids.

Typically, MRSI is performed using a number of RF pulses transmitted in succession, each performing a particular function, such as localizing in one spatial dimension or saturating a narrow spectral band. Because an MRSI scan uses so many different, interacting RF pulses, there are many potential pitfalls. Conversely, there is also much room for innovation, particularly when re-designing the function of RF pulses to operate at higher field.

The goal of this project was to develop and apply acquisition and RF pulse design methods to improve metabolic tissue characterization using  $^1\text{H}$  magnetic resonance spectroscopy imaging techniques for patients with brain tumors. This thesis is organized according to the following chapters that when coupled address the many aspects involved in succeeding this goal. Specifically:

**Chapter 2** provides an overview of brain tumor biology, the diagnostic imaging associated with these neoplasms and how these are coupled with patient therapies as well as the current clinical usage.

**Chapter 3** introduces MR spectroscopy from a chronological point of view; here we see how the technology was introduced and its progress, this will allow a better understanding of where the current project has succeeded.

**Chapter 4** then takes the current approach on a 1.5 Telsa and evaluates the current – most common – advantages of using MRSI as a clinical tool in the serial evaluation of patients with low grade gliomas.

**Chapter 5** takes a theoretical improvement in field strength and data receive coils, and analyzes these in a large data set of clinical patients to characterize clinically relevant improvements.

**Chapter 6** presents an improved spectroscopic imaging technique that takes advantage of pulse design developments to improve tissue coverage using MRSI. An optimal imaging protocol for MRSI at high field systems is then developed, which will utilize an improved outer volume suppression pulse for maximum lipid suppression and improved water suppression.

**Chapter 7** combines the improved outer volume suppression pulses (CM-VSS) with current MRSI and evaluates the clinical applicability of the CM-VSS pulse scheme; this was then validated in MRSI studies of supratentorial brain tissue from various head sizes, shapes, and treated brain tumor patients.

**Chapter 8** summarizes major findings of the aforementioned chapters, discusses the clinical implications, and offers new approaches for future studies.

## Chapter 2: Background I: Brain Tumors

---

*This chapter begins by providing an overview of neoplastic brain diseases with a focus on infiltrative gliomas. A review of tumor characteristics focusing on pathology, prognosis, treatment, and neuroimaging provide a foundation for the relationship between diagnostic imaging tools and how these are coupled with patient therapies as well as the current clinical usage.*

---

### **2.1 Neuroepithelial Tumors**

Primary tumors of the nervous system have had a classification and grading system that has been in a constant flux since the system was first introduced. The World Health Organization (WHO) Classification has proven to be the most widely accepted classification for neuroepithelial tumors (5,6). Among the variability seen within and between these tumors, the classification system is differentiated based focally on histological and molecular features focusing on the differences in these nervous system tumors. The category of neuroepithelial tumors is comprised of gliomas as well as neuronal differentiation and embryonal neoplasms. Among the varying distinct classifications of these tumors, overall classification can be broadly subdivided into infiltrative or non-infiltrative tumors of glial origin. Infiltrative tumors include Astrocytic, Oligodendroglial, and mixed gliomas.

Non-infiltrative tumors include ependymal tumors, choroid plexus tumors, pineal parenchymal tumors, and embryonal tumors (6).

## ***2.2 Infiltrative Gliomas***

The origin and pathogenesis of gliomas is controversial and likely to be multifactorial. Gliomas account for 70% of all primary brain tumors; about 80% of all gliomas are those of astrocytic origin. The incidence in these tumors has been shown to change with aging. The most common neoplasms in young adults are low-grade astrocytoma and oligodendroglioma; in older patients, anaplastic tumors and glioblastoma multiforme (GBM) predominate.

### *Astrocytic Tumors*

Most tumors of astrocytic lineage are described as being diffuse astrocytomas because of the infiltrative nature of these tumors to migrate and proliferate to adjacent and distant brain structures. According to the WHO classification, a low-grade (Grade II) astrocytoma is defined as an astrocytic neoplasm with a high degree of cellular differentiation, slow growth, and diffuse infiltration of neighboring brain. An anaplastic astrocytoma (Grade III) is a neoplasm that demonstrates focal or dispersed anaplasia, with increased cellularity, distinct nuclear atypia, and marked mitotic activity. Glioblastoma multiforme (Grade IV) tumors are classified as ones with a presence of endothelial proliferation and necrosis.

The prognosis of astrocytoma is mainly determined by tumor grade. Low-grade astrocytoma have the best outcome with median survivals of five to ten years (7). Anaplastic astrocytoma have median survivals of two to four years (8). GBM median survivals are by far the worst; these tumors have median survivals of nine to 12 months, and they make up 60% to 80% of the diffuse astrocytic tumors (9). There have been studies that have attempted to focus on improving these outcomes by combining treatment modalities (9). Among the varying parameters that have been considered, differences in age when the tumors arise, as well as the patient's clinical condition are among the leading prognostic factors.

#### *Oligodendroglioma and Mixed Tumors*

Oligodendrogliomas are a subset of primary brain tumors with characteristics of tumor cells that resemble normal oligodendroglial cells. Tumors that have a combination of oligodendroglial and astrocytic elements are termed as "mixed" tumors. Genetically, oligodendroglial tumors have a common occurrence of deletions of 1p and/or 19q. The detection of these deletions is now commonly undergone through genetic testing where deletions of the short arm of chromosome 1 (1p) and long arm of chromosome 19 (19q) have been identified (10). Among the differences in clinical characteristics of tumors of oligodendroglial classification is that they are significantly more responsive to chemotherapy and are associated with better outcomes when compared to other gliomas. Several chemotherapeutic

regimens have been identified to treat these tumors with favorable improvements to patient morbidity (11).

### ***2.3 Clinical Presentation of Neoplasms***

The clinical presentation of all brain tumors is dependent upon two main factors, localization of the tumor and rate of growth. Patients have presented with seizures, neurological deficits (hemiparesis, aphasia, or sensory symptoms), and headaches. These various symptoms could be a direct result from varying characteristics that can include hydrocephalus, mass effect due to tumor burden, and tissue destruction. More malignant tumors often present with focal deficits, cognitive disturbances, and increased intracranial pressure. It is most common for patients with brain tumors to present through the onset of seizures (12).

### ***2.4 Treatment of Neoplasms***

Typically, the treatment of primary brain tumors requires the combination of surgical resection, ionizing radiation, and systemically delivered drugs. The current understanding of the relative roles of radiation and chemotherapy is in a state of flux, as is the understanding of the interactions between responses to therapy and outcomes.

#### ***Surgical Therapy***

Surgical therapy is often the first line of treatment for neoplasms, and is used for the following reasons: (i) to obtain tissue for histological

diagnosis, (ii) to obtain a reduction of symptoms, and (iii) to reduce morbidity due to mass effect (13). The most frequent surgical approach would be to perform the most extensive resection possible to excise the abnormal tissue region without causing excessive neurological damage. This has been largely supported through studies that have demonstrated a favorable relationship with extensiveness of resection and outcome (14). Surgery alone is seldom curative, and the hope for long-term control lies with adjunctive therapy. After surgery is used for diagnosis and tumor debulking, radiation therapy is a mainstay.

### Radiation Treatment

Ionizing radiation therapy is a loco-regional treatment that occupies a position intermediate between surgery and chemotherapy. Radiation therapy plays a vital role in the disease management of neoplasms of the central nervous system (15). The goal is to treat regions of tissue intensively where resection of tissue may not be possible, while sparing the rest of the body from treatment-related side effects. The decision of whether or not to pursue intervention is based upon a complex set of clinical and imaging data, which aim the radiation where the tumor is, while attempting to not exceed the tolerance of the adjacent normal tissue (16).

### Systemic Chemotherapy

Modern cancer systemic therapy was first stumbled upon during World War I when chemical warfare agents were introduced – specifically that of



mustard gas. It was noted that when exposed soldiers were tested for the effects of this chemical, depleted levels of rapidly growing white blood cells were noted – introducing a cytotoxic effect. In the 1940's, the first attempts to translate this concept as a medical therapy was initially led by scientist Goodman and Gilman in the first cancer chemotherapy trial investigating the effects of this cytotoxic agent on patients suffering from advanced lymphomas. Early prognostic improvements were remarkable, and the field of chemotherapeutic drug delivery began (17). Brain tumor chemotherapy did not begin until the 1970's when Wilson and Walker independently published work on treatment of malignant brain tumors using carmustine (BCNU), a nitrosurea. An increase in survival was not measured, but clinical benefit was noted (18,19). Chemotherapy administration to neoplasms still focuses upon improving or maintaining neurologic function.

At the molecular level, chemotherapy seeks to impair the underlying limitless growth that is associated with cancer cells. The chemotherapeutic agent achieves this because of its characteristic ability to affect a cell's function in replication and division or directly affecting the genetic make-up of the cell. Affecting replication and division is associated with diminishing the activity of the cell cycle. The cell cycle consists of five phases,  $G_0$ ,  $G_1$ ,  $S$ ,  $G_2$ , and mitosis, as shown in Figure 2.1.

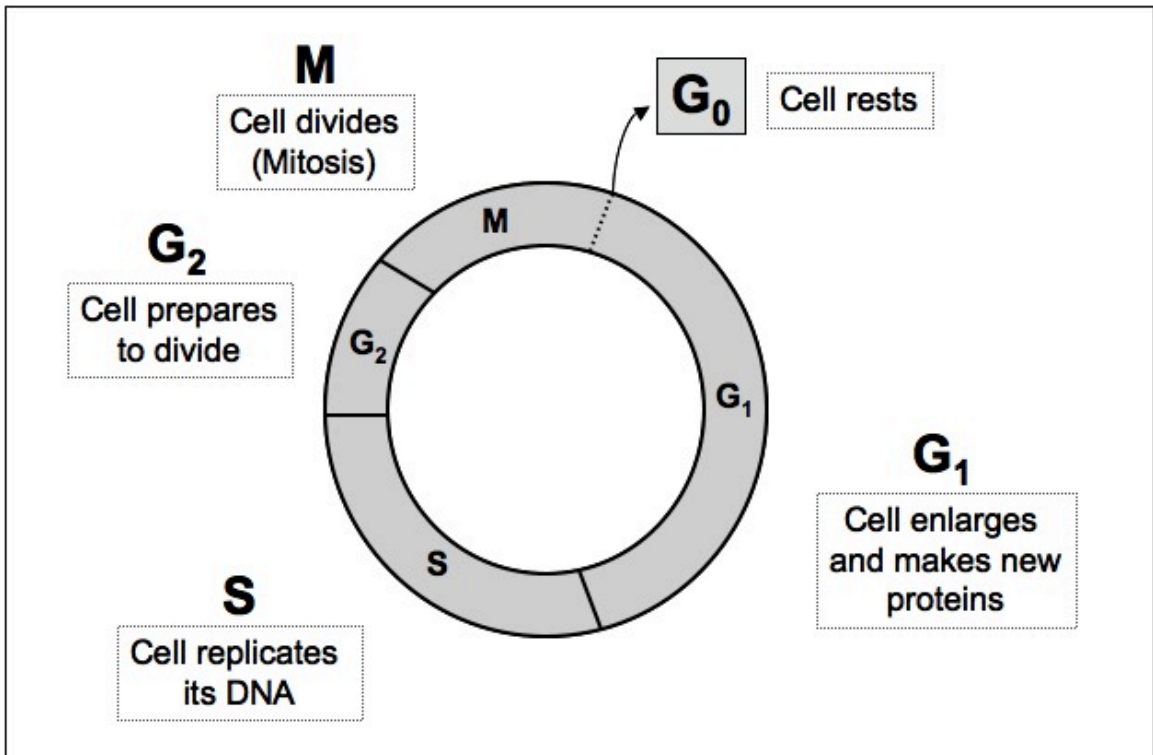


**Figure 2.1: Schematic of cell cycle. A cell could last years in the G<sub>0</sub>, the resting phase, depending on the cell type. When replication is triggered, the cell enters G<sub>1</sub>, a preparation phase for DNA synthesis. The S phase follows where actual DNA synthesis and replication occur. G<sub>2</sub> is the phase immediately prior to mitosis. The M phase is when mitosis occurs and two daughter cells are created.**

Chemotherapeutic agents are generally categorized into two classifications, cell cycle-specific or cell cycle-nonspecific agents. Cell cycle-specific drugs interfere with a particular phase of the cell cycle. For tumor cells to be affected, the cell needs to be in these phases. This is the main reason why these agents are typically being administered in divided doses or as a continuous infusion – affecting cells that are actively dividing. Cell cycle-nonspecific agents directly damage the deoxyribonucleic acid (DNA) within the cell or the enzymes that repair and regulate the DNA. This characteristic

makes these agents more toxic, therefore making this line of therapy effective in a bolus dose.

Chemotherapy may be administered to treat a tumor as a single agent or in combination with other therapies (combination or adjunctive therapy). It may be given prior to surgery to reduce tumor burden, or after surgery to attempt to destroy the remaining cancerous cells. Although prolonged survival is not exclusively noted when chemotherapy is used as an adjunctive therapy, it has been noted that it has played a critical role in maintaining the quality of life.

Although chemotherapies have shown to be effective cytotoxic agents, the brain's protective nature poses limitations that are not encountered in other organs. These limitations are associated with the brain's unique protective mechanism that creates a privileged compartment and poses a significant challenge for treatments such as chemotherapy – studies have shown this to be due to the presence of the blood-brain barrier (BBB) (20). The BBB lines the blood vessels of the brain and helps to protect the brain from toxins. This is accomplished through a layer of endothelial cells that are connected by tight junctions. The BBB prevents passive entry of water-soluble substances based on size, and limits the transport of those larger than 180 D (21).

## ***2.5 Clinical Imaging of Neoplasms***

Neuroimaging has proven to be indispensable for the management of neoplastic brain diseases. The process of detecting a tumor is most

commonly associated with clinical symptoms that are followed by image detection of an abnormality. When an abnormality is detected, the next step is to elucidate the underlying pathology and decide whether it is reason for the symptoms in question. A basic classification should be concluded that will characterize the lesion as neoplastic, vascular, of developmental origin, or inflammatory. When there are cases that have considerable differential diagnosis, imaging should serve to interpret and distinguish between subgroups. Imaging should then supply an evaluation of the grade of malignancy and the probable speed of proliferation. Treatment planning requires imaging to distinguish areas of tumor location and the extensiveness of the tumor. After any therapeutic procedure, imaging is required to monitor the effectiveness of the therapy. In the case of surgical resection (either stereotactic biopsy, subtotal resection, or total resection), imaging is used to monitor the extent of tissue excision. Follow-up examinations should detect tumor response and attempt to indicate recurrence or treatment side effects.

The imaging modality best suited for addressing most of the tasks detailed above is magnetic resonance imaging (MRI). In addition to conventional anatomical imaging that includes T1- and T2-weighted images, new methods exist that characterize the underlying functionality of the tissue. Figure 2.2 below demonstrates traditional imaging with T1- and T2-weighted images in a patient with a brain tumor. The patient example demonstrates the variability in signal intensities that exist when comparing within and between these conventional imaging modalities.

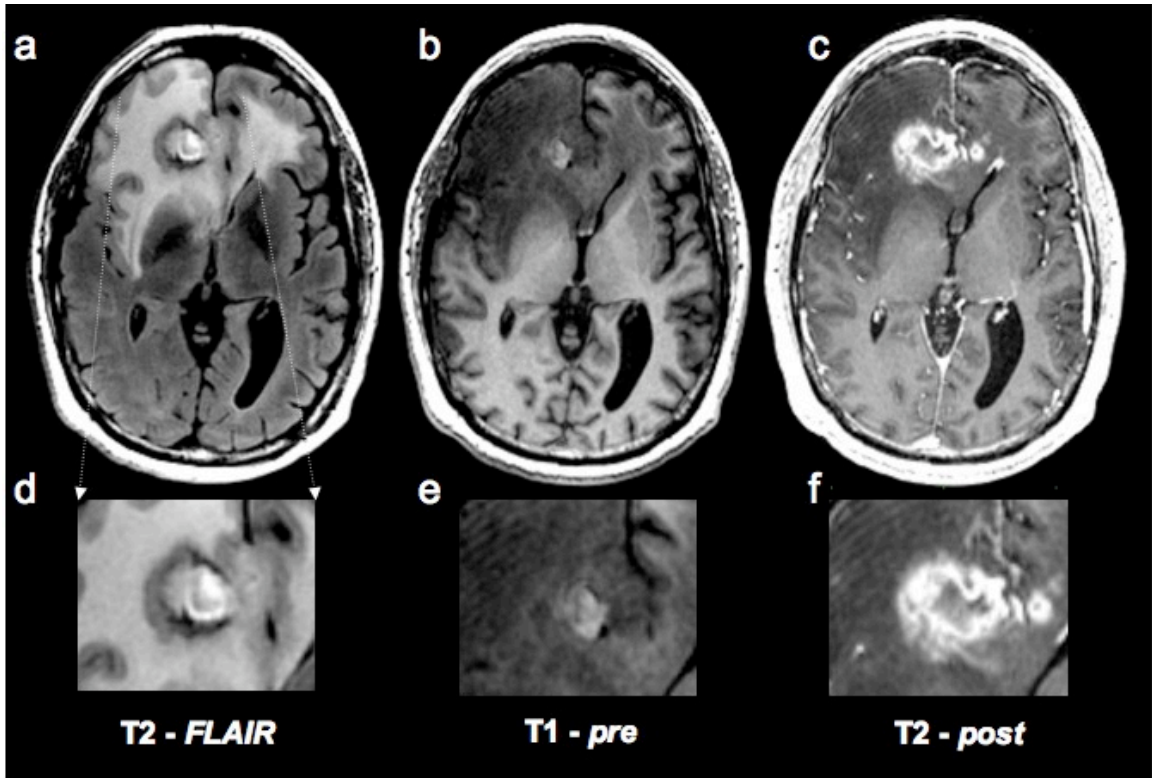


**Figure 2.2: Conventional anatomical imaging of a brain tumor. Patient was diagnosed with a grade IV glioma. (a) T2-weighted image showing a large right hyperintense lesion in the right frontal region extending through the corpus callosum into the left frontal region, (b) T1-weighted *pre*-contrast image shows diffuse hypointense signal along with intrinsic T1-shortening indicating blood products, (c) T1-weighted *post*-contrast injection shows a large area of enhancement within the large lesion demonstrating significant breakdown of the BBB. (d-f) Zoomed images of the necrotic-core portion of the tumor; zoomed images correspond to sub-regions within (a-c) respectively.**

### Tumor Detection

T1-weighted images reflect different tissue contrast between areas that have different T1 relaxation times. T1 is the relaxation time associated with the re-growth of longitudinal magnetization. Similarly, T2-weighted images reflect the tissue contrast between those areas that exhibit different

T2 relaxation times. T2 is the time that depicts the loss of transverse magnetization due to dephasing. The overall signal contrast will reflect the underlying biological structure and the state in which energy is distributed within the surrounding environment.

In T1-weighted images, varying amounts of tissue contrast are generated from tissues that have characteristically different molecular environments; molecules could be compartmentalized generally as free or bound water. These relative amounts of free and bound water within tissues will affect the energy of the molecules. The energy of the molecules in motion is proportional to the velocity of that molecule. The motional energy of the molecule, if faster, will not facilitate longitudinal relaxation, therefore magnetic equilibrium of the water molecule will recover slowly – having a longer T1. This can be shown in Figure 2.3c in the cerebral spinal fluid (CSF) relative to the other tissues.

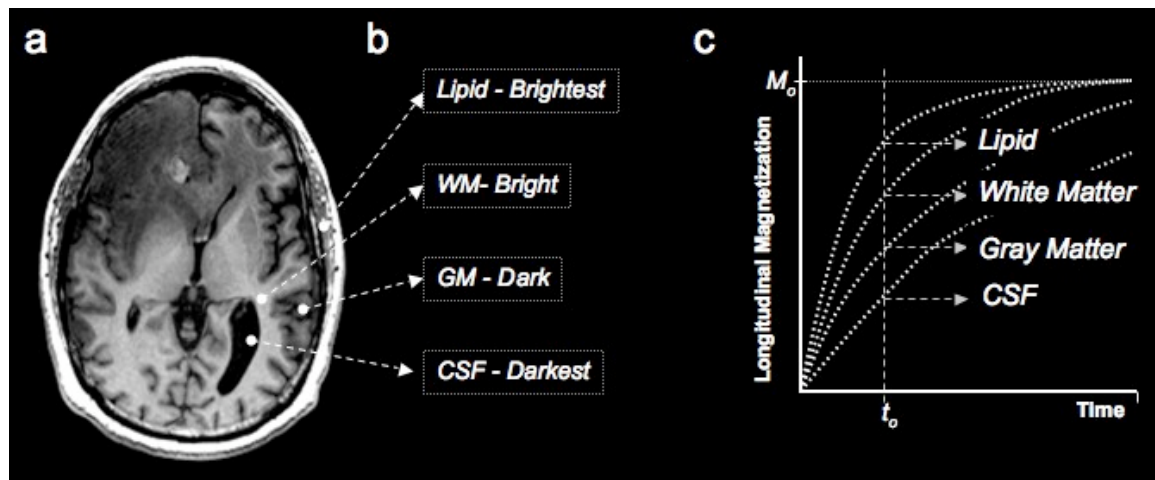


**Figure 2.3: T1-weighted image depicting regions of varying image signal intensity. (a) Axial T1-wieghted SPGR of a glioma patient. (b) Various regions with characteristic differences in signal intensity. (c) T1 relaxation curves for the regions shown in (b). The curves indicate the logarithmic recovery of the longitudinal magnetization.**

Neoplasms typically demonstrate regions of low signal intensity (hypointense signal) in the tumor region on T1-weighted images, as shown in Figure 2.3. The lack of signal, when compared relative to the other regions of normal surrounding tissue occupies a contrast intermediate to that of CSF and gray matter. The low signal intensity here is associated with the highly cellular characteristic portion of the tumor.

T2-weighted images are valuable in differentiating neoplasms because the tumor can be demarcated well because of the characteristic high signal intensity coming from the tumor region. Figure 2.4 shows a glioma patient with a fluid-attenuated inversion recovery (FLAIR) image. FLAIR images are dark fluid T2-weighted sequences that are commonly used when imaging neoplasms; this sequence limits the high signal intensity intracranially to the tumor only – rather than a classic T2-weighted sequence that would also generate high signal intensity from the CSF.

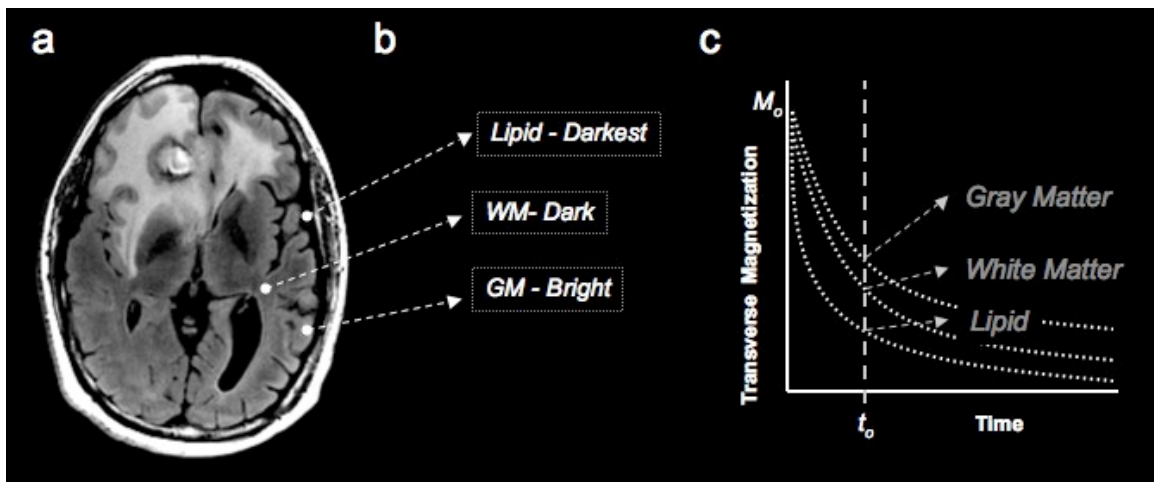


**Figure 2.4: T2-weighted image depicting regions of varying image signal intensity. (a) Axial T2-weighted FLAIR of a glioma patient. (b) Various regions with characteristic differences in signal intensity. (c) T2 relaxation curves for the regions shown in (b). The T2 decay of solid tissue (lipid) is faster than that of free water.**

## Chapter 3: Background II: MR Spectroscopy

---

*This chapter will introduce magnetic resonance spectroscopy leading up to the first in vivo techniques that formulated this application into a key characterization of biological tissue. The applications introduced incorporate the current most widely used 3D-MRSI – with a focus on brain tissue. The varying components of acquisition will allow an understanding of the importance of outer volume suppression; this will allow a better appreciation of where the current project has succeeded.*

---

### **3.1 Magnetic Resonance Spectroscopy**

#### Physics of Magnetic Resonance Spectroscopy

Magnetic resonance spectroscopy (MRS) is a functional *in vivo* technique capable of identifying regions of tissue that exhibit abnormal metabolism and provides information that is not usually seen with anatomic imaging techniques. Conventional MRI focuses on characterizing water, which can be observed separately from other compounds because of its high concentration in the body. As a first approximation, an MR signal from a biological sample can be viewed as consisting of a single peak at the resonance frequency of water. This can be further understood through the Larmor equation shown below:

$$\omega = \gamma B \tag{3.1}$$



Here B is defined as the magnetic field experience by the nucleus – in water the nucleus analyzed is a hydrogen proton ( $^1\text{H}$ ). Omega ( $\omega$ ) is defined as the precession frequency of the magnetic moment of a nucleus, and ( $\gamma$ ) is the gyromagnetic ratio of that nucleus. The B field experienced by a proton is also influenced by its immediate chemical environment as shown by the modified version of the Lamour equation below:

$$\omega = \gamma B (1 - \sigma) \quad (3.2)$$

This includes  $\sigma$ , which denotes a chemical shielding term for the nucleus in question. It is a value between 0 and 1 that specifies the amount a nuclei's chemical environment can compensate for, with respect to the external field. An  $\sigma$  of 1 refers to an environment where the nuclei's environment compensates perfectly for any external field (the nucleus itself experiences no net field), while an  $\sigma$  of 0 effectively denotes a "free" proton, which experiences the external field without any influence from other nuclei. In general, protons bound to more electronegative atoms, such as oxygen, experience less shielding due to their reduced electron density. The alteration of a nuclei's resonance frequency by its chemical surroundings is referred to as chemical shift, and means that protons within different molecules resonate at different characteristic frequencies under a given magnetic field. Therefore, if we find a way to observe resonances at a range of frequencies, we can identify and quantify different compounds within a sample. This is the goal of *in vivo* MR spectroscopy (MRS), which utilizes Fourier transformation of the time domain free induction decay (FID) to

produce a spectrum in the frequency domain allowing a way to examine the spins within different molecular environments.

### Single Voxel Spectroscopy

Single voxel spectroscopy (SVS) is a method for collecting a spectrum of data from a single volume of tissue defined by the intersection of the three orthogonal planes. Within the first clinical applications of *in vivo* spectroscopy the mainstay method was SVS because of technical advantages in short-duration acquisition times and quality of metabolic data. To obtain information about the spatial distribution of metabolites it was necessary to introduce 2D and 3D chemical shift imaging. This method aimed at improving the limited spatial coverage as well as reducing large voxel sizes that have characteristic partial-volume information, therefore complicating the interpretation of data from heterogenous tissues.

### **3.2 Chemical Shift Imaging**

Chemical shift imaging (CSI) is a method for collecting spectroscopic data from multiple adjacent voxels covering a large volume in a single measurement; this could either be from a single slice, 2D acquisition, or multiple slices, 3D acquisition. CSI is commonly referred to in the literature as magnetic resonance spectroscopic imaging (MRSI). Phase encoding is performed if one or multiple dimensions allows for one (1D), two (2D), or three dimensions (3D CSI) of data. A CSI sequence parallels that of an imaging sequence in that the only major difference in a spectroscopic

acquisition is that there is not a readout gradient applied during the data collection. If a gradient were used during the time of data collection the metabolic peaks of interest would experience peak-broadening, therefore compromising the data quality.

### MRS Localization Procedures

Localization in MR spectroscopy is the process of implementing a sequence that will allow the definition of signals coming from a small volume of interest (VOI). It should produce spectra from signals generated within the VOI and minimize the contribution from signals outside. The peaks of interest that comprise the spectrum should have good signal-to-noise ratio with well-resolved peaks that are sufficiently narrow to allow accurate quantification.

Among the various techniques that exist in achieving accurate and acceptable localization, one method that is commonly used performs water suppression and outer volume suppression prior to volume excitation. This is shown as a schematic example in Figure 3.1 where a pulse sequence diagram indicates the time placement of the various components used for this particular method of localization.

### Volume Excitation

Spatial localization is necessary for interpreting the results of *in vivo* MRS. Of the different techniques used to achieve localization, volume excitation stands as a clinical tool that can aid in the control and definition of spatially localized regions for analysis. Among the methods that exist, one

approach that has proven useful is the three-dimensional point resolved spectroscopy (PRESS) technique (22). PRESS is an approach that utilizes three slice selective pulses; one excite ( $90^\circ$  pulse), and refocus (two  $180^\circ$  pulse) pulses to allow for three orthogonal planes of excitation. The spin-echo between the two  $180^\circ$  pulses is not sampled using this approach.

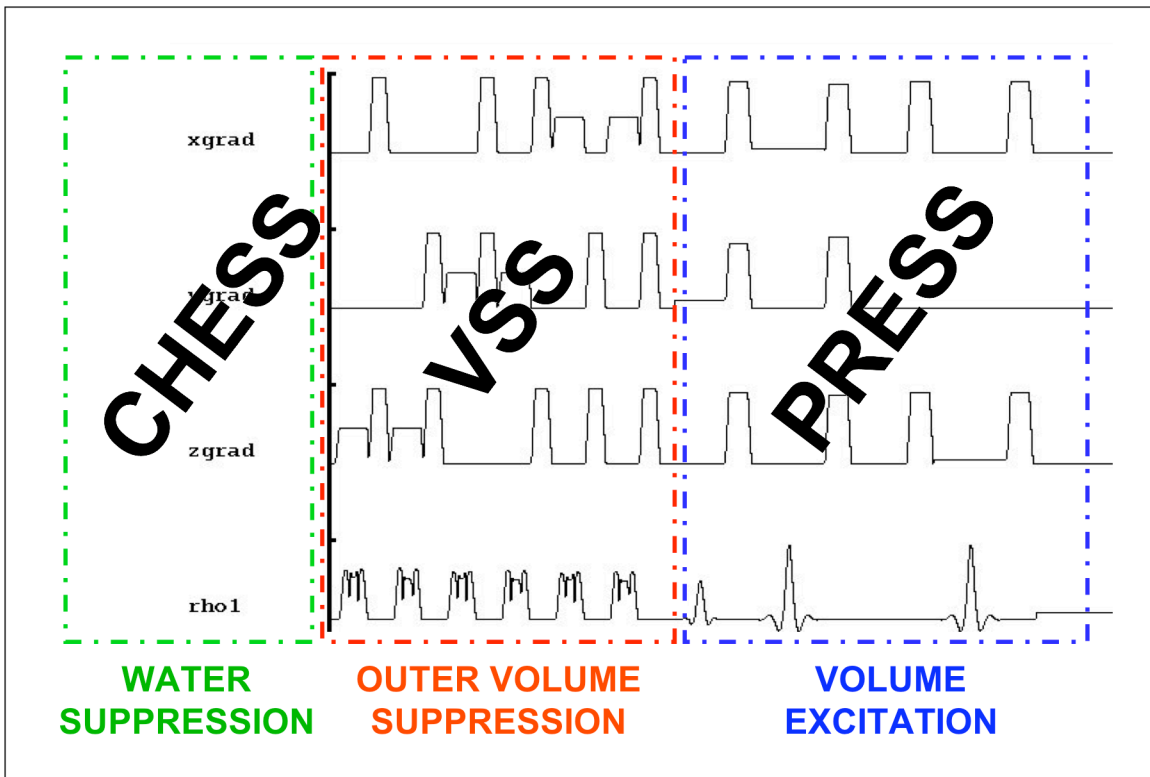


**Figure 3.1: Schematic of a MR spectroscopy pulse sequence that shows the basic order of the varying components of this commonly encountered localization technique. Within the dashed boxes are the acronyms of some commonly used methods; in the background are examples of the four components that make up the backbone of the pulse sequence: x-gradient, y-gradient, z-gradient, and the radio frequency pulses.**

The PRESS technique can be used for single voxel acquisition as well as 2D or 3D acquisitions. When it is used for chemical shift imaging (CSI), the phase encoding method is used to yield arrays of spatially resolved spectra

within the volume of interest. The total acquisition time for a CSI study using this method is proportional to the repetition time and the number of phase encodes in each of the spatial directions. Figure 3.2 shows the pulse sequence timing diagram for a PRESS excitation.

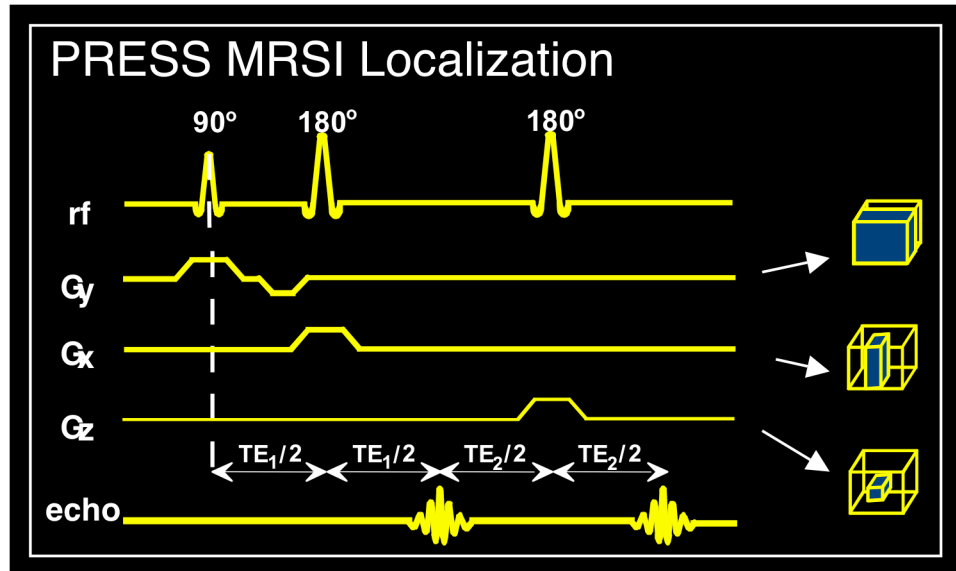


**Figure 3.2: Pulse sequence timing diagram for a PRESS MRS excitation approach. Shown above are the radio frequency pulses, gradients, and corresponding echoes. A pictorial of the spatial selection is shown on the right side of the figure.**

### Water Suppression

In MR spectroscopy, high sensitivity is critical for detecting the cellular metabolites of interest. The large water signal is the primary contributing signal to conventional anatomic MR images and is not only adjacent to the frequencies of the desired metabolite frequencies, but it also has a relative concentration that is tens of thousands of times larger than the metabolites of interest. This is shown as a schematic in Figure 3.2. Suppressing these signals is critical for obtaining spectra that are interpretable and quantitative.

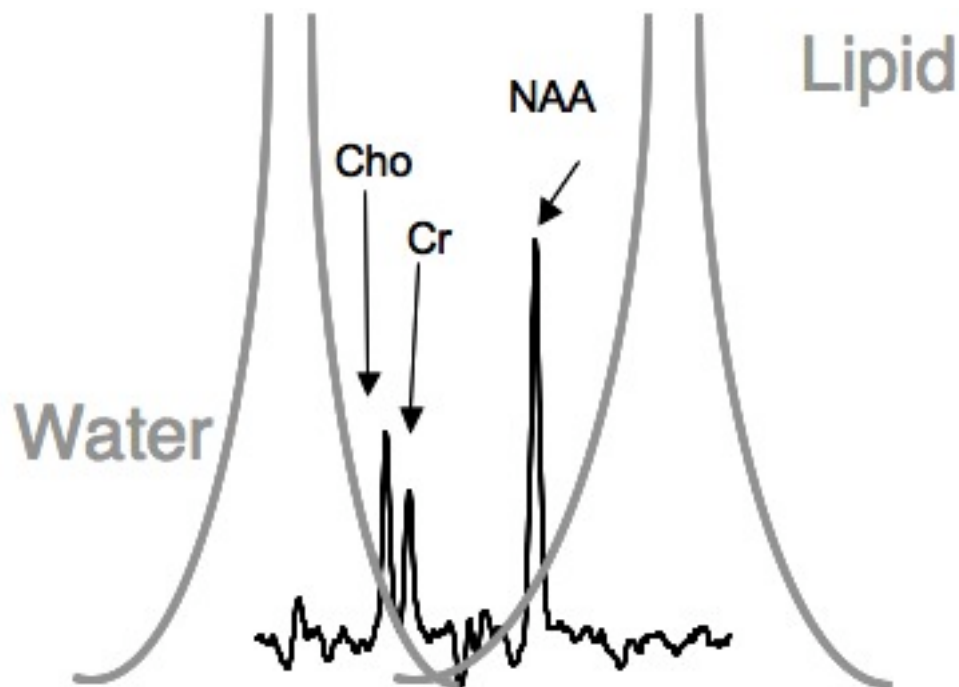


**Figure 3.3: Schematic example of expected proportions of unsuppressed water and lipid signals in brain spectra. The metabolites of interest would be completely affected and would not be interpretable.**

Chemical shift selective (CHESS) imaging technique was developed to suppress and destroy unwanted signal, such as the water shown in Figure 3.2 (23). This was shown to be possible by using a selective  $90^\circ$  excitation pulse and following it with a magnetic field gradient; the gradient would act to spoil the homogeneity of the excited signal through dephasing. The excitation pulse together with the spoiling gradient would take place immediately before the application of a conventional MRS imaging sequence (23). Figure 3.3 demonstrates this combination of the radio frequency (RF) pulse flip angle and gradient in relation to the signal and how it is affected through time. Varying the flip angle of the RF pulse can control the amount of suppression. It should also be noted that the amount of time that exists

between the CHESS RF pulse(s) is played and the excitation pulse will affect the amount of water suppression.

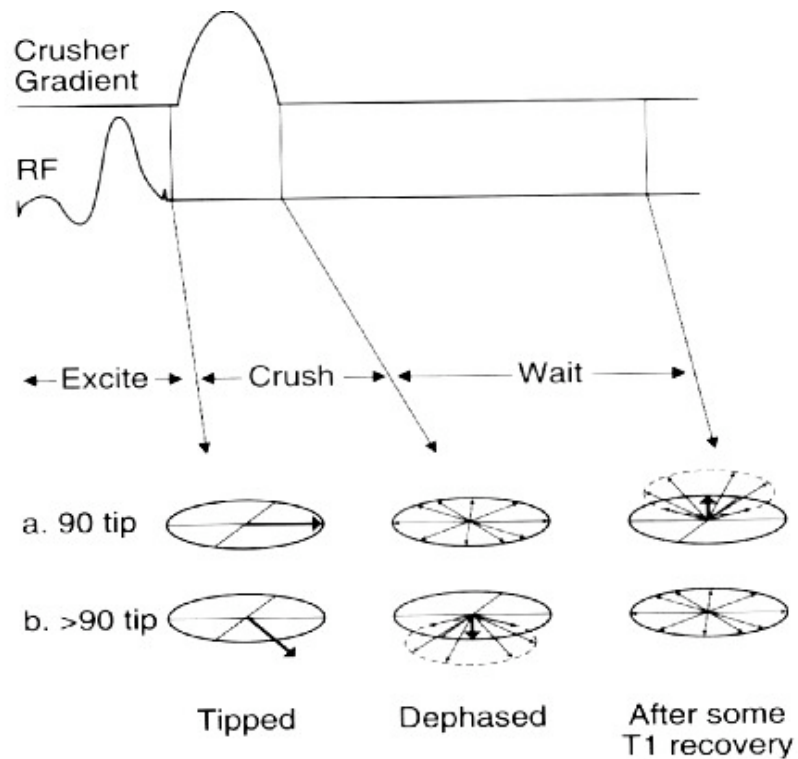


**Figure 3.4: CHESS imaging sequence shown using one radio frequency pulse and one gradient. (a) and (b) show a schematic of the signal for two different flip angles. The example demonstrates the variability that exists with varying flip angles.**

Water suppression is not only important in that it can affect neighboring frequencies from metabolites of interest, but the amount of residual water can also have an impact on the baseline in the spectrum and hence on the accuracy of quantifications. This effect is demonstrated by the spectra shown in Figure 3.4.

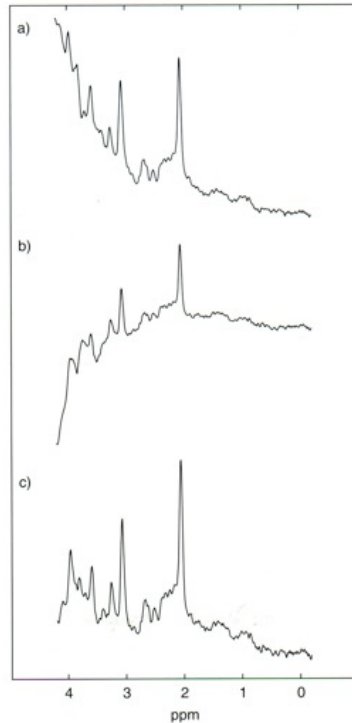


**Figure 3.5: Impact of varying amounts of water suppression. (a) Spectra demonstrating inadequate water suppression – too little. (b) Spectra demonstrating over-compensation of water suppression – too much. (c) Spectra demonstrating adequate water suppression with minimal baseline distortions.**

### Outer Volume Suppression

In proton MRS of the brain, peaks that are seen to the right of NAA, between 0 and 1 ppm, correspond to a lipid signal that may be coming from within the volume of interest (VOI), or from outside the VOI. Ideally, unwanted lipid signals should be eliminated and lipid from within the VOI should be preserved. The lipid that is unwanted (contamination), and generated from outside the VOI is known to come from scalp lipid. A technique that exists to avoid these unwanted lipid signals, spatially saturates signal from unwanted regions – this technique is called outer



volume saturation (OVS). The concept is to use a spatially selective  $90^\circ$  RF pulse to flip the longitudinal magnetization into the transverse plane. Unlike excitation RF pulses, spatial saturation pulses should result in as little transverse magnetization as possible. This pulse is immediately followed with a gradient of maximum amplitude; this gradient will cause maximal phase dispersion, with minimal time commitment. The amount of signal generated within the desired saturation region will then be minimized. An example of saturation bands is shown in Figure 3.6 around the sides of the desired MRS acquisition volume.

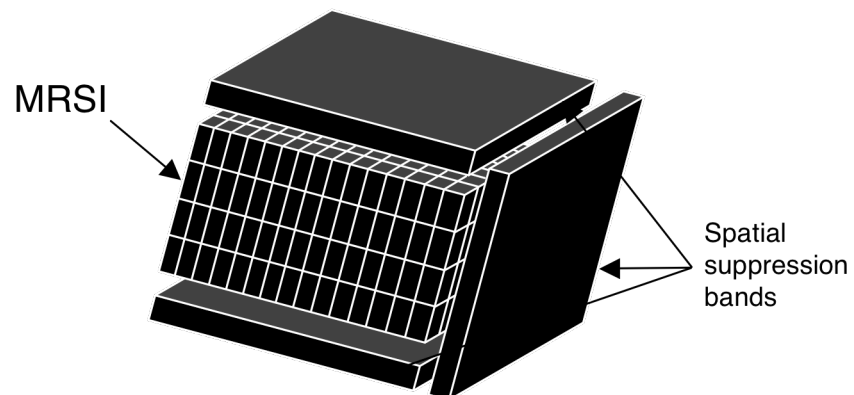


**Figure 3.6: Spatial saturation bands placed around the sides of the MRSI slices.**

The pulse timing sequence shown in Figure 3.7 highlights the OVS pulses as well as the crusher gradients. Note that for each OVS pulse there are two crusher gradients that immediately follow. Six OVS pulses are shown in succession as an example for a sequence that will generate six saturation bands for the six sides of a three-dimensional rectangular excitation volume.

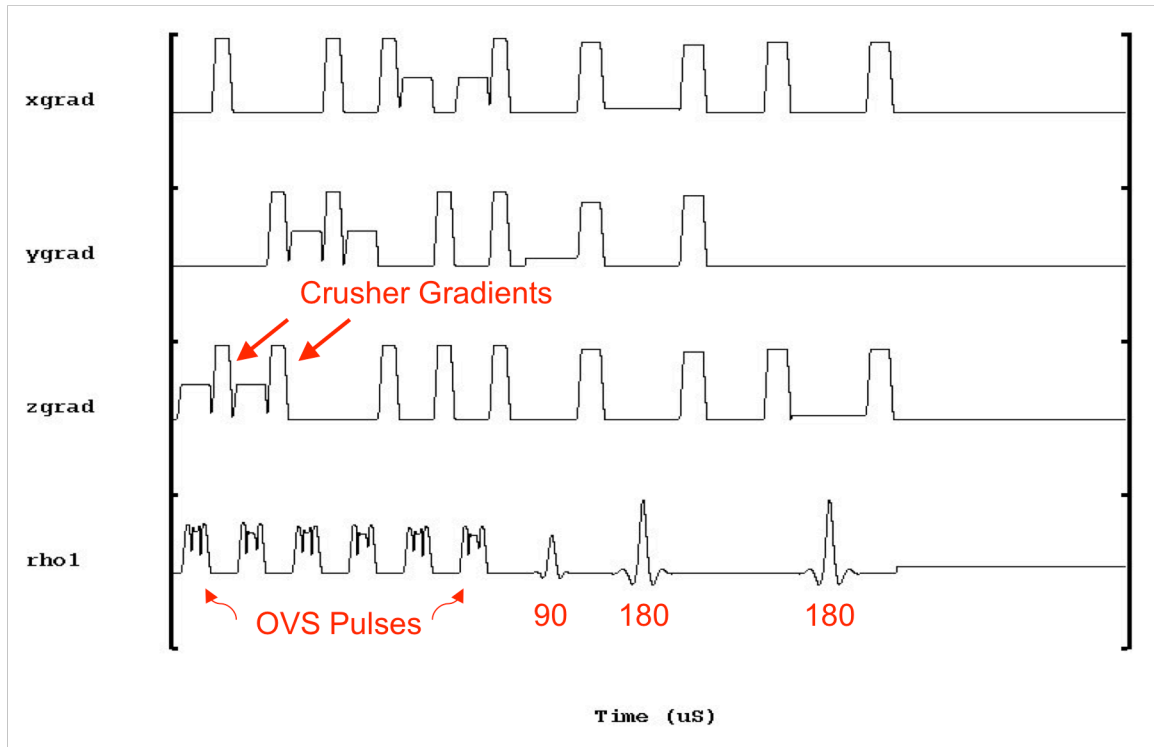


**Figure 3.7: Pulse timing sequence showing outer volume suppression (OVS) pulses as well as the crusher gradients. Note that for each OVS pulse there are two crusher gradients that immediately follow. Also shown is an example using the PRESS volume excitation pulses. Volume excitation typically follows OVS.**

As mentioned above, the RF pulse utilized for outer volume suppression is needed to minimize the maximum amount of transverse magnetization. Improved methods of outer volume suppression have accomplished this and have also increased the versatility and performance of CSI acquisitions (4). The very selective suppression (VSS) pulse introduced by Tran et al, shown in Figure 3.8, was designed as a phase-modulated radio frequency pulse that would allow high bandwidth excitation for optimal performance at minimal time cost and minimal transition band width; the phase modulated characteristic comes at the cost of a nonlinear phase response – this happens to be one of the goals of a saturation pulse.

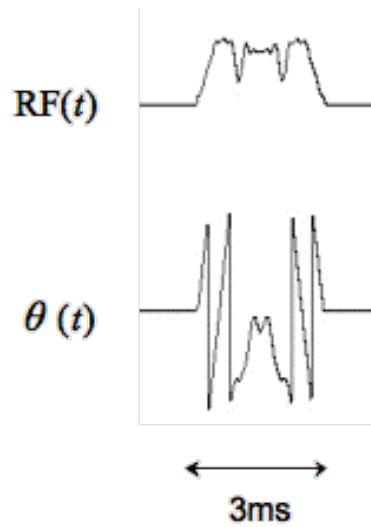


**Figure 3.8: Very selective suppression pulse. Shown above is the RF excitation pulse and below the phase modulated component of the RF pulse.**

Phantom experiments shown in Figure 3.9 using VSS pulses for outer volume suppression not only demonstrate the performance of these pulses, but also these results show that if the outer volume suppression scheme is not adequate, the data can become severely compromised and could become unusable.

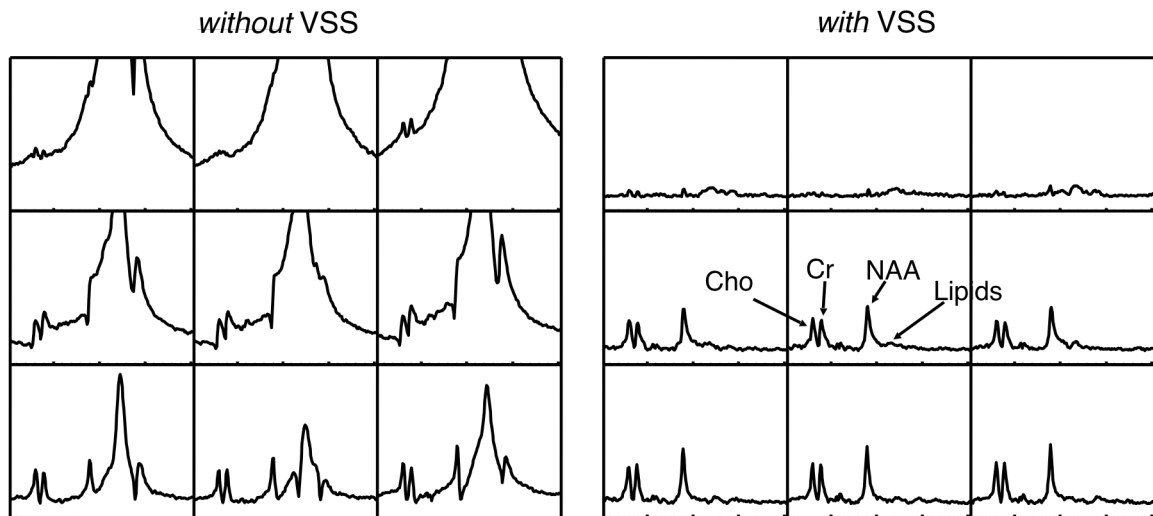


**Figure 3.9: Example data set showing the efficacy of the VSS pulse. Two example sets are shown; one set is acquired without VSS pulses and the other is acquired with VSS pulses.**

*In vivo* MRSI utilizing VSS pulses for outer volume suppression differs than experiments with data generated from phantoms. One characteristic of *in vivo* data that is not noticed in phantom experiments is the amount of residual signal within suppressed regions. VSS pulses are highly efficient, but not perfect – they are noted to have around 95% efficiency in suppressing signal from unwanted regions (4). *In vivo*, the amount of residual scalp lipid that remains at 95% efficiency is diminished sufficiently to avoid signal from contaminating the VOI. Figure 3.10 is an MRSI example from a volunteer focusing on the performance of the VSS saturation bands on the scalp lipid regions.

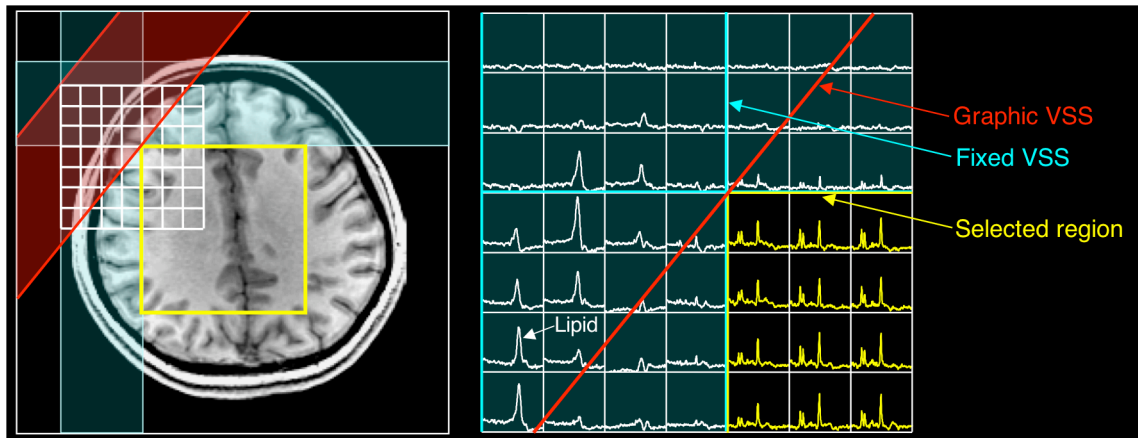


**Figure 3.10: In vivo data example of outer volume suppression using VSS pulses. Three separate suppression bands are shown schematically overlaid on a volunteer T1-weighted image. Only a small portion of the selection region is was selected to demonstrate adequate unwanted scalp lipid suppression without compromise of signal from within the volume of interest.**

### MRSI of Brain Neoplasms

Magnetic resonance spectroscopy imaging (MRSI) has the ability to interrogate tissue biochemistry and is a powerful tool that adds to the information obtained by conventional radiology. For brain tumors it may indicate abnormalities in normal appearing tissue outside that as depicted by conventional MRI. The ability for MRSI to investigate biochemical features of tissue has shown metabolites and their relationship to tumor activity relative to that of normal tissue.

Choline appears as a singlet that appears at 3.22 ppm. When elevated relative to normal appearing tissue, it has been defined as a general marker for cancers in the brain. The elevation of choline is thought to be due to accelerated membrane synthesis of rapidly dividing cancer cells. The choline peak contains choline, phosphocholine, and glycerophosphocholine, which are

major components of biological membranes. In extracts of tumor biopsies the choline peak has been found to predominantly phosphocholine and glycerophosphocholine. In vivo choline levels have been shown to correlate with proliferative potential as determined by immunohistochemical analysis of tumor biopsies for gliomas.

Creatine appears as a singlet that appears at 3.04 ppm comprising of creatine and phosphocreatine. When creatine is compared to normal brain, it is reduced in glioma patients, particularly astrocytomas. Creatine is related to the cellular energetics. N-acetyl aspartate (NAA) appears as a singlet that appears at 2.05 ppm, and is indicative of the presence of viable neurons within brain tissue. NAA is reduced or absent within regions of tumor in brain tissue and has been associated with infiltrative tumors such as gliomas.

Lactate appears as a doublet at 1.33 ppm and is frequently observed in tumors due to the tumor preference for aerobic glycolysis. Lactate in proton MRS is generated from both intra- and extracellular spaces; its overall level is a function of metabolic rate and clearance, with the possibility of lactate pooling within necrotic or cystic regions.

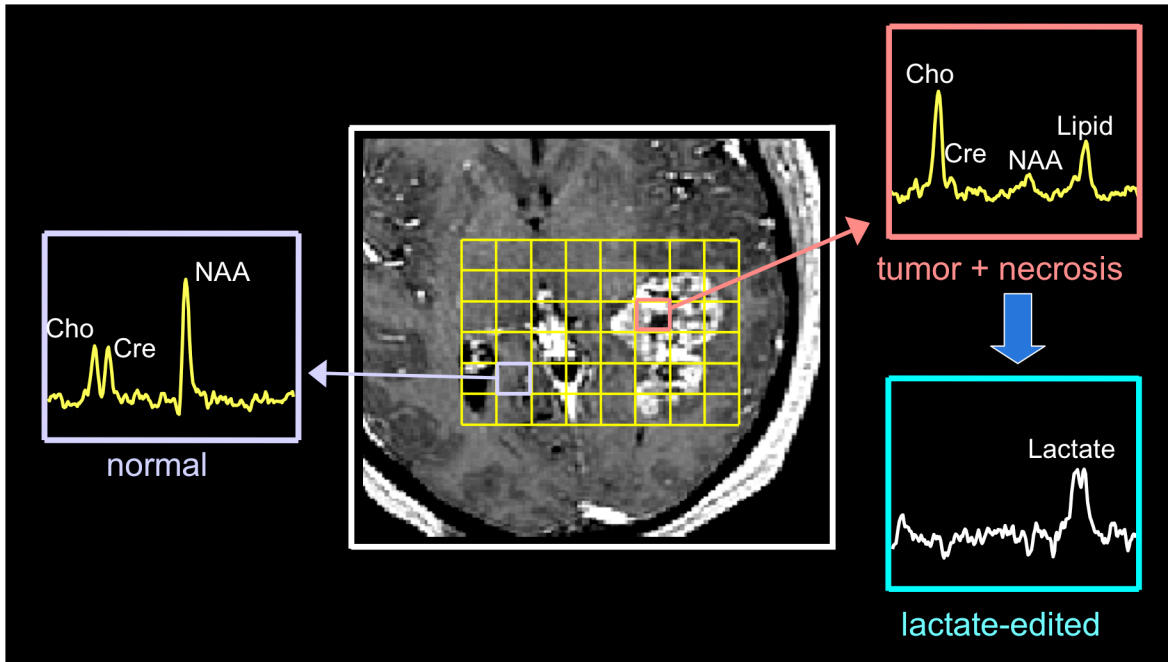


**Figure 3.11: In vivo magnetic resonance spectroscopic imaging of a brain tumor patient with a high-grade glioma in the poster occipito-temporal region. It can be noted that choline (Cho), creatine (Cre), N-acetyl aspartate (NAA), lipid, and lactate all exist within the voxel examples. Normal and tumor voxels were chosen to contrast the varying metabolic patterns that distinguish both.**

Lipids appear at 1.3 or 0.9 ppm and are very characteristic of high-grade tumors. Extract studies indicate that lipids correlate with necrosis, which is a histological characteristic of high-grade tumors. Lipids have been thought to be associated with phospholipids release during cell breakdown. Figure 3.11 illustrates these tumor characteristics using MRSI from two regions of brain tissue in a patient with high-grade glioma. Two voxels were chosen corresponding to regions of normal and abnormal tissue metabolism.

## **Chapter 4: Serial assessment of therapy response for low-grade glioma patients through MR diffusion, perfusion, spectroscopic, and anatomical imaging at 1.5 Tesla**

---

*Magnetic resonance spectroscopic imaging (MRSI) is capable of assessing the underlying metabolism in cerebral tissue. This chapter will investigate not only MRSI in tumor patients, but also other functional MR imaging techniques to better understand treatment response in low-grade glioma patients. These techniques are used to generate a more comprehensive understanding of changes serially – focusing on change within normal and abnormal regions as defined by conventional anatomical imaging, as well as metabolic imaging.*

---

### **4.1 Low Grade Glioma Background**

Prolonged survival of patients with Grade II gliomas has made it important to identify prognostic indicators that may be used to evaluate therapy response and manage patients on an individual basis [1]. Conventional imaging methods have not been able to reliably distinguish changes in low-grade gliomas [2]. Alternative techniques such as diffusion, perfusion, and MR spectroscopic imaging (MRSI) have shown improvements over conventional MR in tracking patient response to therapy. Identifying MR parameters is valuable in assessing treatment response. The advantage in tailoring therapies for individual patients would spare the potentially toxic



effects of agents. The purpose of this study was to investigate the serial changes in various MR parameters for a population of low-grade glioma patients undergoing treatment with chemotherapy.

## **4.2 Methods**

### Patient Population

Twelve patients (nine men and three women) with low grade gliomas were included in this study. Their ages ranged from 28 to 66 years, with a median of 38 years. Tissue samples obtained during surgical resection or open biopsy were graded by histologic examination using criteria defined by the World Health Organization (WHO). All 12 patients had histologically confirmed grade II gliomas (seven oligodendrogliomas, three astrocytomas, and two oligoastrocytomas). Entry into the study was within five weeks of confirmed tumor grade. Patients were provided informed consent, approved by the Committee on Human Research at our institution.

### Treatment

Subtotal resections were performed on 11 of 12 patients prior to their initial pre-therapy scan. One of 12 patients did not receive a resection, therefore only receiving a biopsy. All patients had no prior treatment with radiation or biological therapy. Patients were treated with chemotherapy alone, using temozolomide. Temozolomide was delivered with a dose of 200mg/m<sup>2</sup>/day for 5 days and repeated every 28 days for a maximum of 12

cycles; one patient was an exception receiving 18 cycles of therapy. The specific treatments cycles and descriptions are shown in Table 4.1.

**Table 4.1: Patient treatment demographics.**

<b>Diagnosis</b>	<b>Grade</b>	<b>Resection</b>	<b>Treatment</b>	<b>Cycles</b>	<b>Progression</b>
Oligoastrocytoma	II	Subtotal	None	N/A	Yes
Oligodendroglioma	II	Subtotal	Temozolomide	12/12	Yes
Oligodendroglioma	II	Subtotal	Temozolomide	12/12	----
Oligoastrocytoma	II	Subtotal	Temozolomide	18	----
Astrocytoma	II	Subtotal	Temozolomide	12/12	----
Oligodendroglioma	II	Biopsy	Temozolomide	12/12	----
Oligodendroglioma	II	Subtotal	Temozolomide	7/12	Yes
Oligodendroglioma	II	Subtotal	Temozolomide	12/12	----
Astrocytoma	II	Subtotal	Temozolomide	5/12	Yes
Astrocytoma	II	Subtotal	Temozolomide	11/12	----
Oligodendroglioma	II	Subtotal	Temozolomide	12/12	----
Oligodendroglioma	II	Subtotal	Temozolomide	12/12	----

MR Data Acquisition

A total of 36 MRI examinations were performed on 12 patients on a 1.5 Tesla GE Signa Echospeed MR scanner (GE Healthcare Technologies, Milwaukee, WI) using a quadrature head coil. Each patient received three scans over a projected four month period as shown in Figure 4.1.

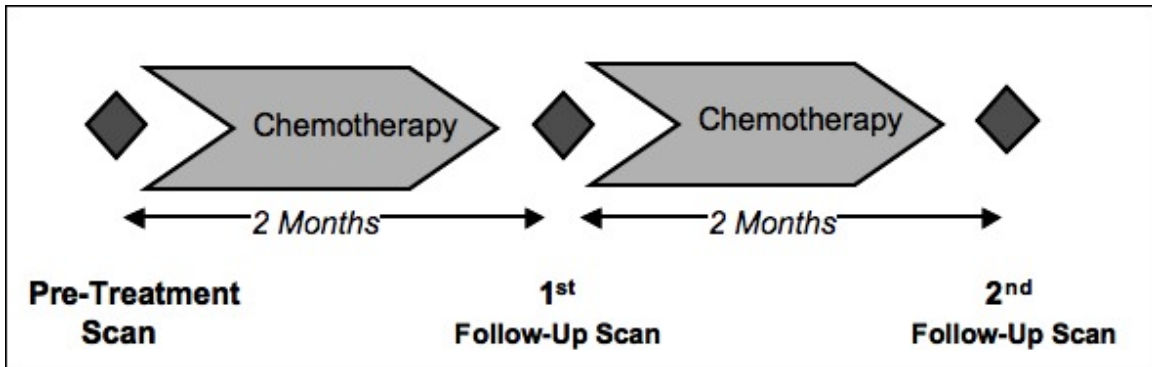


**Figure 4.1: Serial time points for scan acquisitions. The chemotherapy treatment time periods are detailed within the projected scanning dates.**

The MRI protocol included pre-contrast axial T1-weighted volume spoiled gradient echo (SPGR) images (TR = 35 ms/TE = 8 ms, flip angle = 45°, 124 slices, slice thickness = 1.5 mm), axial fluid attenuated inversion recovery (FLAIR) images (TR = 10000 ms, TE = 148 ms, TI = 2200 ms, slice thickness = 3 mm), axial diffusion weighted imaging using echo planar imaging-spin echo (TR = 5000 ms, slice thickness = 3 mm, 36x21 FOV, 256 x 128 matrix, b = 1000 s/mm<sup>2</sup>), and post-contrast T1-weighted volume SPGR images (TR = 27 ms/TE = 5 ms, flip angle = 40°, 124 slices, slice thickness = 1.5 mm).

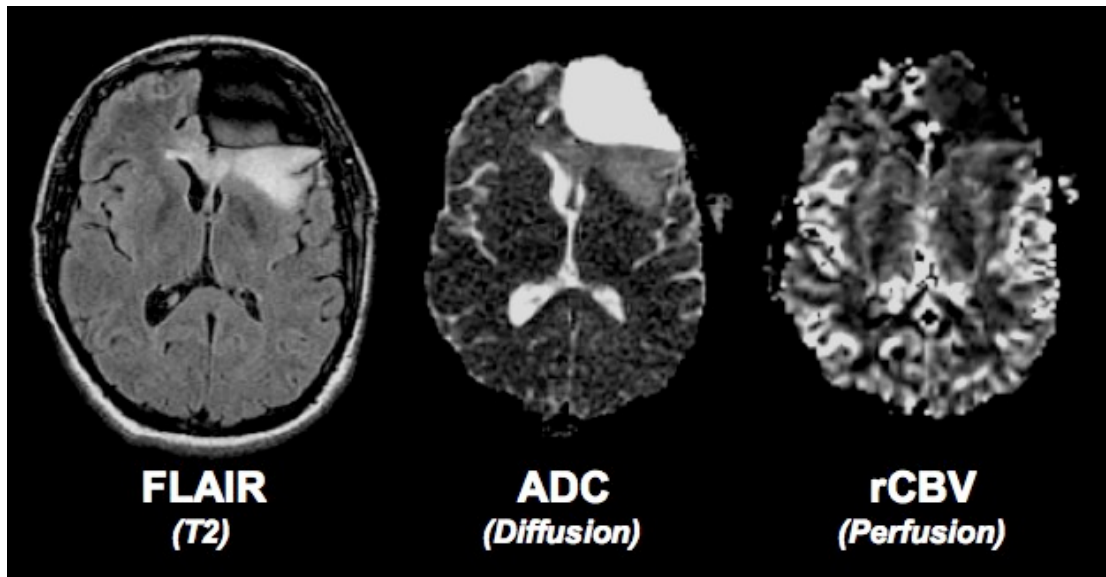


**Figure 4.2: Conventional anatomic FLAIR and functional MR maps of diffusion (ADC) and perfusion (rCBV). All images are from an Oligodendroglioma patient with a left frontal neoplasm; this was the pre-treatment scan performed after a subtotal resection. In this slice the resection cavity is noted adjacent and anterior to the T2 hyperintense abnormal signal in the FLAIR image. The ADC map demonstrates increased diffusion in the region corresponding to T2 abnormality, and the rCBV map shows slight hypointense signal in the respective region.**

Perfusion was obtained using a dynamic imaging sequence with a bolus injection of 0.1 mmol/kg body weight of Gd-DTPA contrast agent at a rate of 5 mL/s. Shown below in Figure 4.2 is an oligodendroglioma patient with FLAIR, ADC, and rCBV at an equivalent slice.

Three-dimensional Magnetic Resonance Spectroscopic Imaging (MRSI) data was obtained using point resolved spectral selection (PRESS) volume selection technique combining phase-compensating spectral- and spatial-selective  $180^\circ$  pulses for water suppression. A typical acquisition is phase-encoded with a matrix of  $12 \times 12 \times 8$  or  $16 \times 8 \times 8$  with a TR of 1000 ms and TE of 144 ms. MRSI data sets were acquired in 17 minutes at a nominal spatial resolution of 1.0 cc. The precision of the PRESS box selection depended upon the bandwidth of the radio frequency (RF) pulses, which were substantially improved by using very selective suppression (VSS) pulses (4).

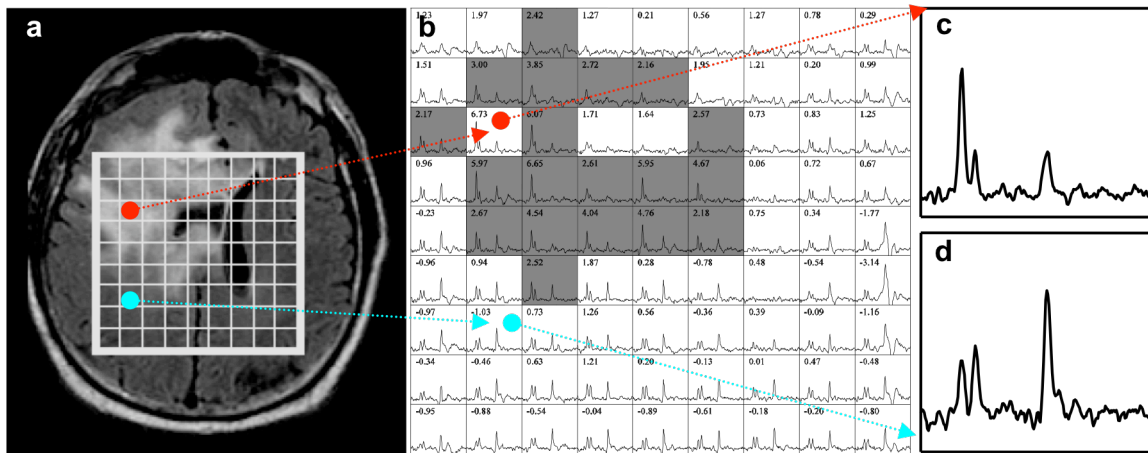


**Figure 4.3: FLAIR and MRSI of a right fronto-occipital low-grade oligodendroglioma. (a) FLAIR with PRESS-MRSI selection overlay. (b) MRSI corresponding to PRESS selection from (a). (c,d) Example voxels of (c) abnormal and (d) normal tissue metabolism. Note that MRSI selection extends into normal tissue for comparative spectra with abnormal regions.**

The MRSI data was obtained from a region that included the mass of tumor and as much of the adjacent and contralateral normal tissue as possible to provide a reference for the post-processing and analysis (Figure 4.3).

#### MR Data Post-Processing

Each MRI data set was aligned to the initial scan from the serial study as shown in Figure 4.4. Anatomical images were contoured manually and used for volumetric analysis. The regions of interest (ROI) included the regions of high signal intensity on the FLAIR image, these were defined as T2 hyperintense regions and, if present, the T1 contrast enhancement. Contours were generated, as shown in Figure 4.5, for all time points (pretreatment, two month follow-up, and four month follow-up scan) acquired within the serial evaluation.

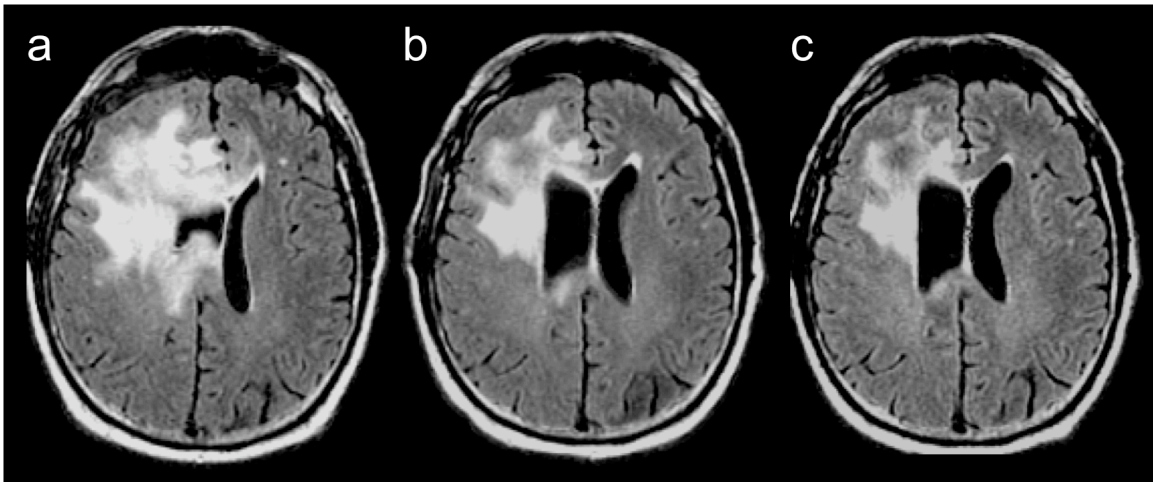


**Figure 4.4: FLAIR serial images of a right fronto-occipital low-grade oligodendroglioma. (a) Pretreatment scan. (b) First follow-up scan. (c) Second follow-up scan. Images (b) and (c) are both aligned in reference with (a).**

The apparent diffusion coefficient (ADC) and the relative blood volume (rCBV) parameters were analyzed within the regions of T2 hyperintensity

(Figure 4.5). Metabolic data was used to generate contours using the method provided below.

A previously developed automated statistical analysis technique was used to identify voxels with normal metabolic properties in patients diagnosed with brain tumors (24). The spectra that were identified as being normal were then used as controls for evaluating the probability of disease being present at each voxel location. The number of standard deviations of difference between the relative Choline (Cho) and N-Acetyl Aspartate (NAA) levels within a given voxel and that of the control voxel determined the degree of spectral abnormality. This quantitative score is referred to as the Cho/NAA index (CNI) and is defined by its residual or z-score. Through definition, control voxels fell within two standard deviations for each patient, therefore voxels with  $CNI < 2$  were considered metabolically normal.

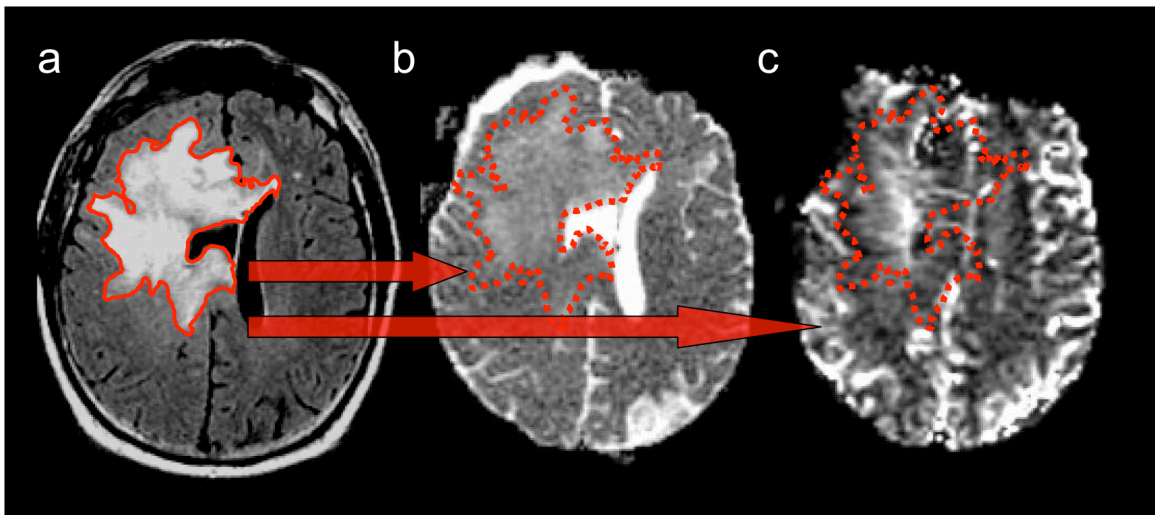


**Figure 4.5: Abnormal T2 region is manually contoured from the FLAIR anatomical image (a). This ROI is then superimposed upon the (b) ADC and (c) rCBV maps to generate values.**

A study looking at the histopathological validation of the CNI found that a CNI of 2 is an appropriate lower limit corresponding to tumor with 0.96 sensitivity, and 0.57 specificity, with a 95% confidence (25).

The CNI values obtained from the MRSI were used as intensities to create a CNI image. This image was interpolated to match the resolution of the anatomical image, and contours were generated using the CNI values that were representative of abnormal metabolic regions ( $CNI \geq 2$ ). These contours were superimposed upon the anatomical images to give a better representation and visualization of the metabolically abnormal regions (Figure 4.3). 3D volumes were generated to represent the spatial extent of the abnormal metabolic region.

### **4.3 Results**

#### Pre-Therapy

The pre-treatment T2-hyperintensity (T2h) volumes displayed a range of 4.4-240.1cc as shown in Table 4.2. Five of twelve patients showed contrast enhancement with a range of 0.1-9.3 cc. The volumes of CNI2 lesions ranged from 1.3-51.4 cc, in all but three cases these were substantially smaller than the volume of the T2h. Median ADC values within the T2h region were in the range of  $1002-1493 \times 10^{-6} \text{ mm}^2/\text{s}$ , and 25<sup>th</sup> percentile ADC values ranged from  $854-1279 \times 10^{-6} \text{ mm}^2/\text{s}$ . ADC values for normal tissue had a significantly lower median value of  $832 \times 10^{-6} \text{ mm}^2/\text{s}$  compared to ADC within regions of T2h ( $p < 0.05$ ).

**Table 4.2: Pretreatment T2 volumes of abnormality, CNI volumes, and ADC values.**

<b>Pretreatment Variable</b>	<b>Median</b>	<b>Range</b>
T2 abnormality volume (cc)	24.4	4.4 – 240.1
CNI-2 volume (cc)	17.6	1.3 – 51.4
ADC in NAWM ( $10^{-6}$ mm <sup>2</sup> /s)	832.0	159 – 920.0
ADC in T2-L ( $10^{-6}$ mm <sup>2</sup> /s)	1286.5	1002 – 1493.2
ADC in CNI-2 ( $10^{-6}$ mm <sup>2</sup> /s)	1171.5	924 – 1515.0

Follow-Up

During follow-up scans, the volumes of T2h were found to be significantly different after the two month follow-up ( $p < 0.05$ ) and also after the four month follow-up ( $p < 0.02$ ) compared to the pre-therapy exam (Wilcoxon Signed-Rank Test). Ten of twelve patients responded with a decrease in T2h, presenting a median decrease of 29.5%, with one patient remaining stable, and one patient showing progression. The ADC values within the regions of T2h as defined separately for each examination were stable as a function of time. A patient example demonstrating serial ADC data is shown in Figure 4.6.



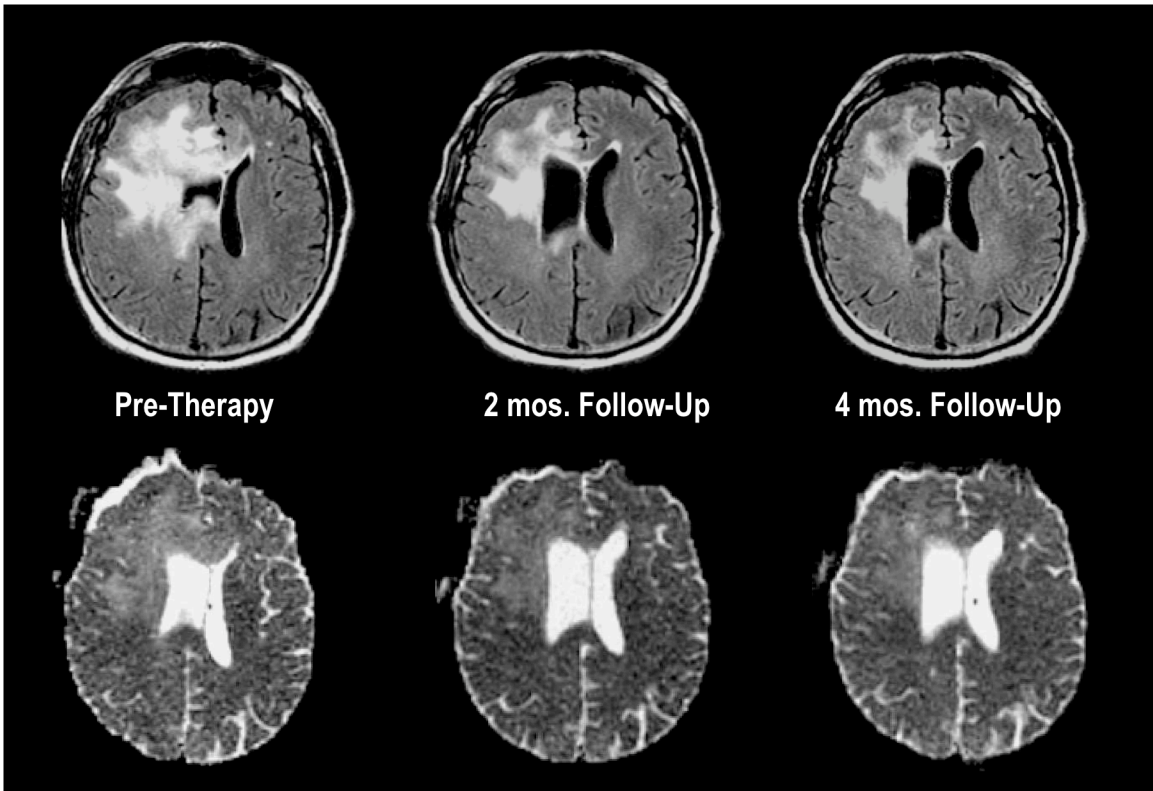


**Figure 4.6: Serial FLAIR images with slice corresponding ADC maps for a right fronto-occipital oligodendroglioma patient. Although the FLAIR images do show a decrease in T2 hyperintense signal, the ADC maps – when analyzed – did not demonstrate significant change in values.**

CNI2 volumes were found to be significantly smaller at second follow-up ( $p = 0.052$ ) compared to pre-therapy. The magnitudes of the volume changes in metabolic lesions were different from the changes in the T2h, providing contradictory results for 5/9 patients and indicating that there were six patients who responded, two who progressed and one who remained stable. Serial changes within the MRSI suggest that low-grade glioma tumors are heterogeneous in time and space. Heterogeneity within the MRSI data is shown in Figure 4.7 below in a patient with a right fronto-occipital

oligodendroglioma where there are metabolic changes indicating improvement over time.

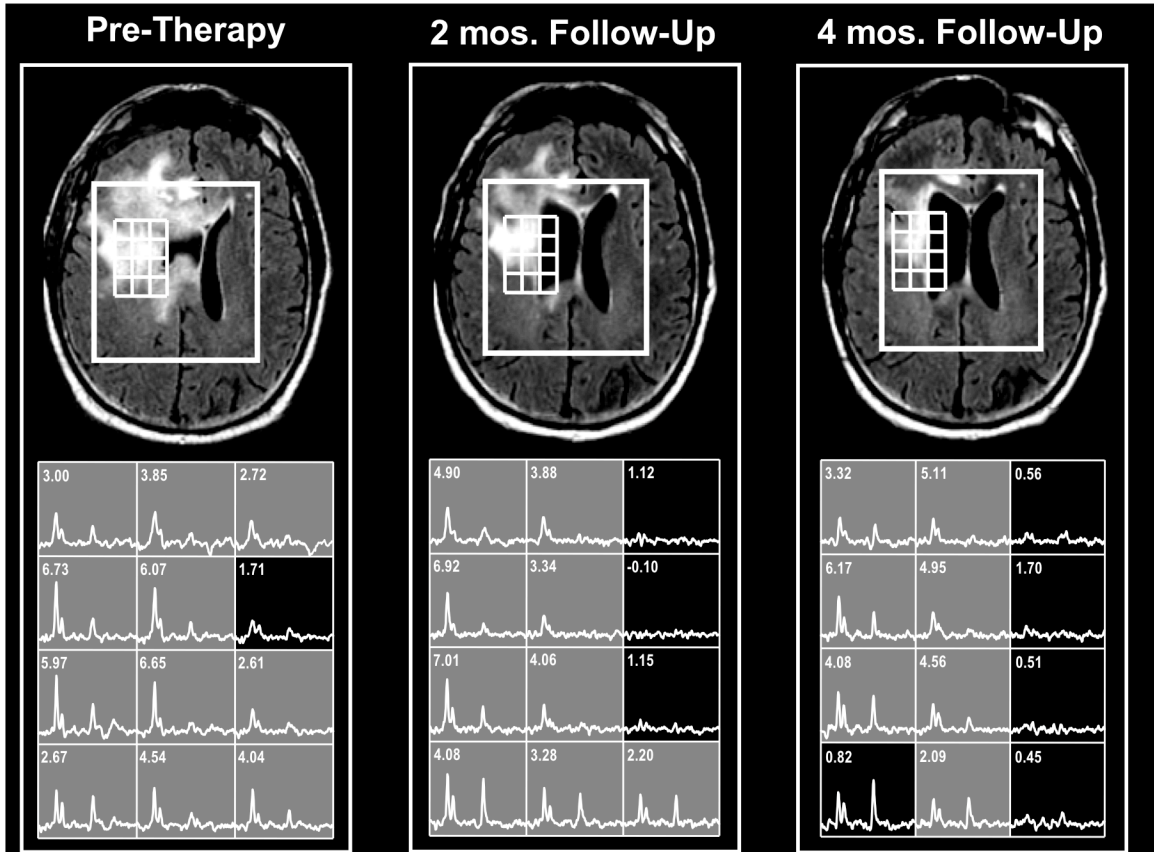


**Figure 4.7: Spectral patterns corresponding to tissue that has shown a reduction in T2-hyperintensity from pre-therapy, to the first follow-up, to the second follow-up time point. Reduction of choline from baseline is apparent at the first and second follow-up time points. Recovering NAA levels can also be observed at the second follow-up time point. The improved choline/NAA levels is evident among the changes in the CNI values.**

#### **4.4 Discussion**

In our study we found that the volume of the metabolic lesion as defined by MRSI data was much less than the volume of the T2h for 8/9 patients with low-grade gliomas. This has implications for the interpretation

of response to therapy for such lesions and is consistent with the T2h corresponding to a mixture of tumor and edema. Although we found that there was a significant change in T2-hyperintensity (T2h) within the first four months of low-grade gliomas receiving chemotherapy, it is highly unlikely that the effects of chemotherapy alone would cause an improvement in such a short time span. This implies that changes in the T2h reflect variations in the extent of edema in addition to the effects of chemotherapy and may be misleading in terms of patient response to treatment. The ADC within the T2h regions were similar to pre-treatment values at both the two and four month follow-up examinations. Hence it seems unlikely that ADC will provide additional information concerning response to therapy for this population of patients. Previous studies in our laboratory have suggested that metabolic lesions are a more reliable measure of tumor than morphological lesions (1,26). If the changes in the volume of the metabolic lesion are used to assess response to therapy rather than the volume of T2h, we would have made different conclusions for more than 50% of our patients. While further follow-up is required in order to determine whether these parameters are predictive of long-term outcome, it seems likely the MRSI data contain information that will help in determining whether the observed changes are due to residual tumor or to changes in the spatial extent of edema.

## Chapter 5: 3D $^1\text{H}$ MRSI of Brain Tumors at 3.0 Tesla using an 8-Channel Phased Array Head Coil

---

*In this chapter we present the implementation of 3D  $^1\text{H}$  MRSI at 3 T using an 8-channel phased array head coil for a population of brain tumor patients. Also, we focus on evaluating the quality and metabolite SNR of the data generated.*

---

### **5.1 Background**

Although magnetic resonance imaging (MRI) examinations are the current standard for evaluating brain tumor patients, there are circumstances when the interpretation of the images is complicated by the difficulties in identifying the true extent of the lesion and in distinguishing treatment effects from tumor progression (27,28). Since morphologic images are unable to provide information about tissue function, there has recently been an increased demand for alternative imaging techniques that reflect functional rather than morphologic properties of the tissue.

Proton magnetic resonance spectroscopic imaging ( $^1\text{H}$  MRSI) is an *in vivo* imaging technique capable of identifying regions of tissue that exhibit abnormal metabolism (1,2,29-32). It has been shown to provide vital information about the spatial extent and degree of abnormal metabolic activity of gliomas both within the contrast enhancing volume and in

surrounding areas of hyperintensity on the  $T_2$ -weighted images (1,2,29-32). This information has gained significance for brain tumor characterization because it provides insight into the physiological properties of the underlying tissue. It has been implemented as a commercial product at the standard clinical field strength of 1.5 Tesla and has generated promising results (1,2,32,33).

3 Tesla (3 T) MR systems are now offered by most commercial manufacturers and are becoming frequently used for clinical applications. Previous studies have demonstrated the initial benefits in sensitivity and specificity in spectroscopic imaging acquisitions when moving up in magnetic field strength (34-38). Single voxel MRS has shown promising results with brain tumor characterization at 3 T (39), and there has been one study that has shown the ability to obtain data from two brain tumor patients at 3 T with 3D  $^1\text{H}$  MRSI (35). Although these studies have provided proof of principle, it is important to determine whether they are applicable in a larger population of brain tumor patients that are representative of those encountered routinely in clinical practice. It is also important to examine whether the relative levels of Cho, Cr and NAA in normal brain and tumor are different at 3 T versus 1.5 T.

The use of phased array coils is desirable for conventional imaging at both 1.5 T and 3 T because it provides higher signal-to-noise ratio (SNR) than standard volume coils (40,41). The use of phased array detectors has been applied for brain MRSI previously (40-42), but has not been presented clinically in brain tumors with 3D MRSI at 3 T. The increased SNR that is

associated with higher field strength and multi-channel phased array coils is expected to be important for MRSI (36,40,41,43-45) and for increasing the spectral resolution of the data (34,46). The purpose of this study was to implement 3D  $^1\text{H}$  MRSI at 3 T using an 8-channel phased array head coil for a population of brain tumor patients, and to evaluate the quality and metabolite SNR of the data generated.

## ***5.2 Study Population***

Seven volunteers and 34 patients (22 men and 12 women) with histologically confirmed brain tumors were included in this study. Volunteer ages ranged from 25 to 28 years, and patient ages ranged from 25 to 67 years. Tissue samples obtained during surgical resection or open biopsy were graded by histologic examination using criteria defined by the World Health Organization (WHO). Thirty-two patients had histologically confirmed tumors of glial origin (eight grade II, nine grade III, and 13 grade IV, one gliomatosis cerebri, one brainstem glioma), and two had tumors of non-glial origin (malignant lymphoma, and meningioma III). Patients provided informed consent as approved by the Committee on Human Research at our institution. Gross total or subtotal resections were performed prior to their scan. Patients had received varying levels of treatment, including a combination of chemotherapy and/or radiation therapy.

### Conventional MRI

A total of 49 MRI/MRSI examinations were performed (on seven volunteers and 34 patients) on a 3 T GE Signa EXCITE scanner using the body coil for RF transmission and the 8-channel phased array head coil for signal detection. Eight of the patients received two scans each. T2-weighted axial FLuid Attenuated Inversion Recovery (FLAIR) images (TR/TE/TI = 10000/120/2200 ms, 48 slices, slice thickness = 3 mm, skip 0), pre- and post-contrast axial T1-weighted volume 3D SPOiled GRAdient echo (SPGR) images (TR/TE = 26/8 ms, 40° flip angle, 124 slices, slice thickness = 3 mm, skip 0) were acquired and used to select regions of T2-hyperintensity and normal appearing white matter (NAWM) for further analysis. The magnetic field homogeneity was optimized using higher order shimming over the volume of interest prior to the MRSI acquisition. Proton density weighted gradient echo (GRE) images were acquired using the manufacturer-provided parallel imaging calibration sequence to estimate the sensitivity profile from each coil element (TR/TE = 150/2 ms, 64 x 64 matrix, 30 x 30 mm FOV).

### <sup>1</sup>H MRSI Acquisition

The three-dimensional Proton Magnetic Resonance Spectroscopic Imaging (<sup>1</sup>H MRSI) data were acquired using point resolved spectroscopy (PRESS) volume selection, with TR/TE = 1100/144 ms. The precision of the PRESS volume selection depended upon the bandwidth of the RF pulses, 933 Hz for the 180° pulse and 2400 Hz for the 90° pulse, which were substantially improved by using very selective suppression (VSS) pulses (4).

Chemical shift misregistration were reduced by prescribing a PRESS box larger than the region of interest (overpress), and using VSS pulses to suppress signals arising from beyond the region of interest. At 3 T, an overpress factor of 1.2 has been shown to significantly reduce the chemical shift artifact (36). Chemical shift selective saturation (CHESS) pulses were used for water suppression (4).

The PRESS-selected volume was in the range of 147-324 cm<sup>3</sup>, with a mean of 241 cm<sup>3</sup>. The MRSI data obtained was from a region that included the tumor mass and as much of the adjacent and contralateral normal tissue as possible to provide a reference for the post-processing and analysis (47). These acquisitions had a phase encoding matrix that was 16 x 16 x 8 with a FOV of 160 x 160 x 80 mm. K-space sampling was restricted to the central elliptical region of the array, and the radius of the sampled region was set to cut the acquisition time to approximately one-half of that for full rectangular sampling (17 minutes). Table 5.1 presents the acquisition times, the number of excitations, and the nominal voxel size obtained using the standard GE MRS head phantom (12.5 mM NAA, 10 mM Cre, 3 mM Cho, 5 mM lactate, 12.5 mM Glu, and 7.5 mM mI, pH 7.2, 0.1% Magnavist) and one volunteer. The SNR was approximately 1.4 times when comparing reduced to full rectangular sampling of k-space. Using the equation  $SNR \propto \Delta X \sqrt{t}$ , while maintaining all other conditions similar, this result suggested that the nominal voxel size with an elliptical acquisition would be 2.0 times that of the rectangular acquisition (48).



**Table 5.1: Acquisition times, number of excitations, and nominal voxel sizes for data acquired.**

<b>Acquisition</b>	<b>Time (minutes: seconds)</b>	<b>Number of excitations</b>	<b>Nominal voxel size (cc)</b>
Phantom			
Rectangular	37:37	2048	1.0
Ellipsoidal	17:32	952	2.1
Volunteer			
Rectangular	37:37	2048	1.0
Ellipsoidal	17:32	952	2.0

*<sup>1</sup>H MRSI Reconstruction*

Upon completing each MRSI examination, the images and spectra were transferred to a workstation for off-line processing using in-house software. The <sup>1</sup>H MRSI processing algorithms have been described elsewhere (47). Spectral data reconstruction was evaluated by Nelson et al. (47), and it was determined that data apodization at 1.5 T with a 2 Hz Lorentzian exponential provided a good compromise between degrading spectral resolution and improving SNR. Therefore, a 4 Hz Lorentzian filter was chosen for the spectral data at 3 T, assuming that the linewidth variations were linear with respect to field strength. The spectral data were zero-filled to 1024 points, apodized in the time domain using a 4 Hz Lorentzian exponential and Fourier transformed, resulting in an array of spectra. The spectral baseline was removed; phase shifts and frequency shifts were corrected for each spectrum using prior information about the relative location and linewidth of each metabolite peak (47). Spectral arrays from the eight-channel coil were processed individually, and the signals were combined using the in-house

developed software that weights the data by their coil sensitivities, as demonstrated for a phantom in Figure 5.1.

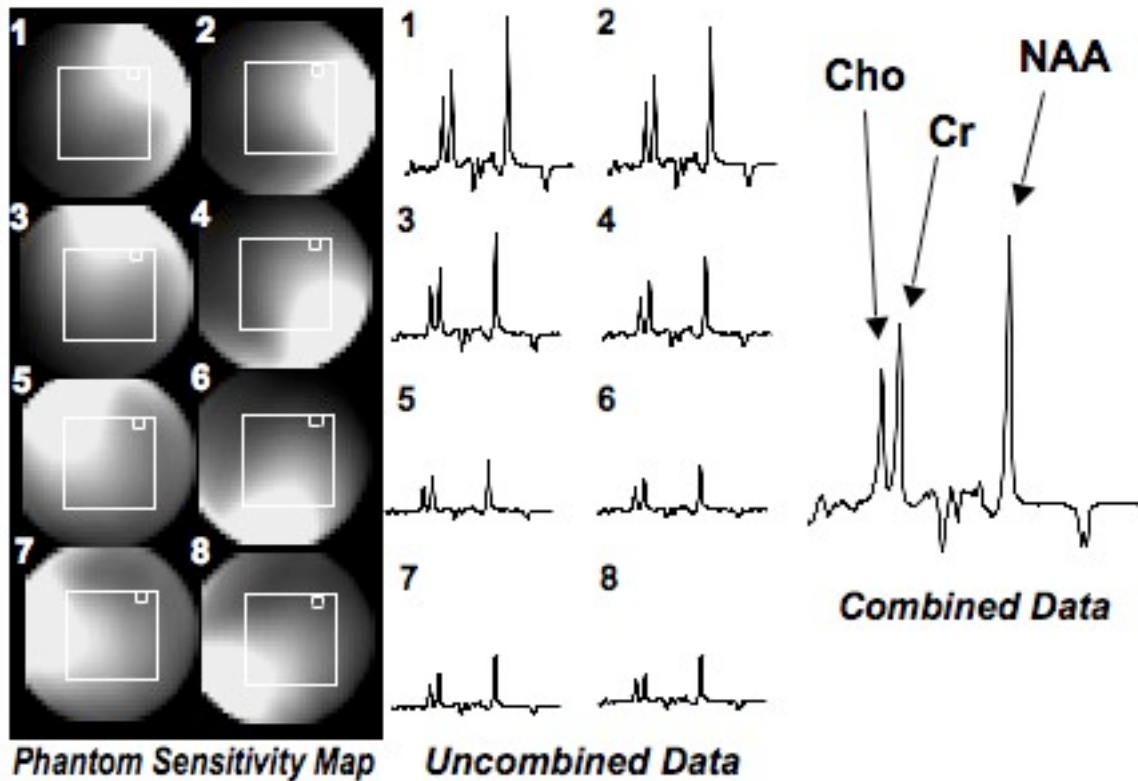


**Figure 5.1: Phantom data for a single voxel from all eight individual coil receptions are shown uncombined. The resulting combined data for the example voxel are shown on the right.**

The theory of the combination for eight-channel data was based on SENSE (SENSitivity Encoding) reconstruction with a reduction factor (R) of 1.0 as described in a previously cited article (49). The signal intensity variation shown is primarily dominated by receiver coil sensitivity. Metabolite images for N-Acetyl Aspartate (NAA) were generated for a normal volunteer, as shown in Figure 5.2, demonstrating the spatial sensitivity of the individual coils, as well as the uniformity from the resulting combined data.

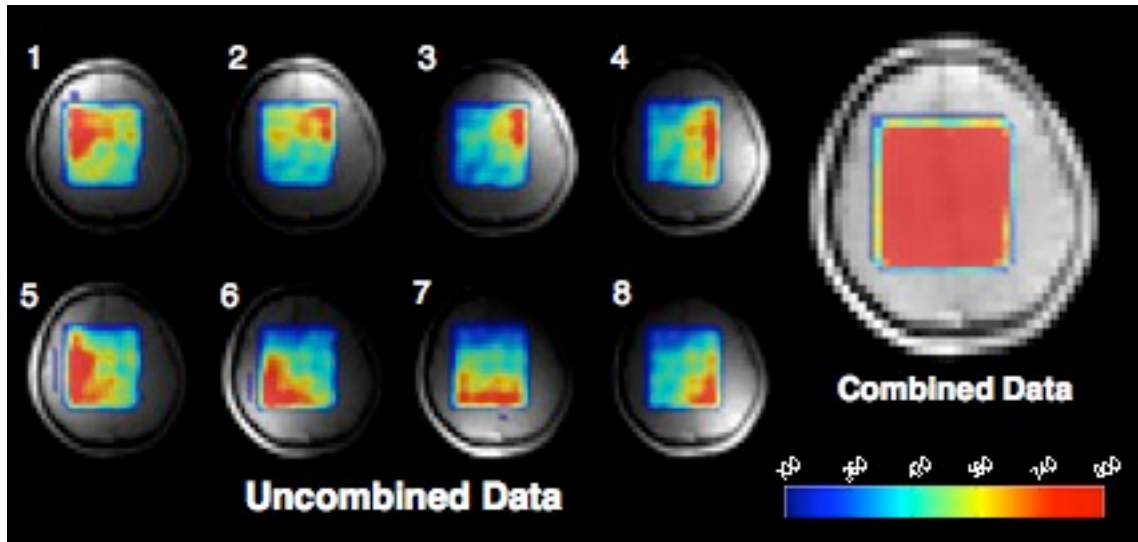


**Figure 5.2: Metabolite maps of NAA peak amplitude, within the PRESS-selected region, are displayed in color overlaid on the coil sensitivity acquisition for a normal volunteer. Corresponding maps for each of the 8 individual coils are shown uncombined along with the combined data.**

### 1H MRSI Volume Segmentation

Image analysis of each examination consisted of 3D regions of interest (ROIs) of the morphologic abnormalities using the T2-weighted hyperintensity lesion (T2L), which were contoured manually by a neuro-radiologist experienced in the assessment of brain tumors. The volumes of each of the morphologic abnormalities were determined using IDL-based software developed in our laboratory. Pre-contrast T1-weighted 3D SPGR images were used for segmentation of white matter (WM) using a Markov random field model. The regions of T2-hyperintensity were then subtracted from the WM segmentations to produce a NAWM map. The resulting maps were regridded to yield the fraction of each spectroscopic voxel that was deemed NAWM,  $f_{NAWM}$ , or T2-hyperintense,  $f_{T2}$ . All voxels in which  $f_{NAWM} < 0.9$

or where  $f_{T2} < 0.7$  were excluded from further analysis. The remaining mean metabolite peak height values within voxels of NAWM and T2-hyperintensity regions were then used to calculate regional metabolic ratios.

### *In Vivo Metabolite Measurements*

Signal-to-noise ratio (SNR) measurements were calculated to test receiver coil sensitivity (homogeneity) from both the 8-channel phased array coil and the standard volume head coil. A gradient echo (GRE) sequence was used to produce minimal tissue contrast *in vivo*, resulting in a proton density weighted image. Imaging parameters were maintained the same for both acquisitions. SNRs were calculated to analyze the coil sensitivity from superior to inferior regions, and from lateral to medial regions. Adjacent circular 1 cm<sup>2</sup> areas were evaluated, beginning at the edge of the volunteer brain tissue, and mean SNR values were used for comparison.

Signal-to-noise ratios (SNRs) were calculated for three metabolites: Choline (Cho), Creatine (Cre), and NAA for volunteers and patients. After exponential multiplication of the spectral data, the peak heights for Cho, Cre, and NAA were obtained in each voxel and the mean values from all the voxels in the representative ROI determined the signal for that region. The noise was calculated using the mean standard deviation of the noise from the right end of the spectral region within the PRESS-selected volume that was devoid of metabolite peaks. Spectral linewidths for Cho, Cre, and NAA were calculated after exponential multiplication of the data using the full-width at half-maximum (FWHM) of the spectral line of interest for each voxel.

MR spectroscopy data were further processed using a previously developed automated statistical analysis technique that is used to identify voxels with normal and abnormal metabolic properties in patients diagnosed with brain tumors (24). This technique characterizes spectra based on the relative levels of Cho to NAA. The assumption used for this analysis was that normal tissue has small variations in Cho/NAA when compared with histologically confirmed tumor regions that exhibit increased Cho and reduced NAA. Voxels were classified into normal and abnormal based upon an iterative procedure that selectively removed outliers from a linear regression of Cho to NAA. A quantitative index was determined for each voxel by calculating the distance of its Cho and NAA values from the regression line. Division of this index by the standard deviation of the distances for all of the normal voxels provided a parameter that is referred to as the Cho-to-NAA index (CNI) (1,24). A cut-off of 2 standard deviations was used to separate control voxels and metabolically abnormal voxels for each patient. Voxels with a CNI higher than 2.0 ( $CNI \geq 2$ ) were considered metabolically abnormal (24). A Cho-to-Cre index (CCrI) was calculated equivalently to the CNI using Cho and Cre levels.

### **5.3 Results**

Both the patient and the volunteer data demonstrated that good quality 3D  $^1H$  MRSI data could be obtained consistently using the 8-channel phased array coil at 3 T. After the spectra were combined, a 4 Hz filter was applied and linewidths for data from normal volunteers were  $11.9 \pm 2.2$  Hz,

11.3±1.9 Hz, and 12.8±2.9 Hz (mean ± standard deviation) for choline, creatine, and NAA, respectively. Corresponding linewidths for tumor patients were 12.0±2.3 Hz, 11.4±2.0 Hz, and 12.5±3.0 Hz (Cho, Cre, NAA). A comparison of data quality was evaluated for filtered data, 4 Hz Lorentzian, versus unfiltered data. The 4 Hz Lorentzian filter showed an average improvement in SNR for Cho, Cre, and NAA of 2.3 over unfiltered data (0 Hz). Figure 5.3 shows examples of the different spectral patterns seen in a patient with a grade IV glioma. The normal voxel has choline and creatine that are approximately 50% lower than NAA, with relatively sharp peaks and high SNR. The region of abnormality shows highly elevated choline, reduced creatine and NAA. These metabolites are virtually absent in the other two spectra, which show the inverted doublet of lactate and a larger, single peak that was interpreted as being lipid. The color overlay shows the CNI map, with the highest values being in the posterior edge of the lesion.

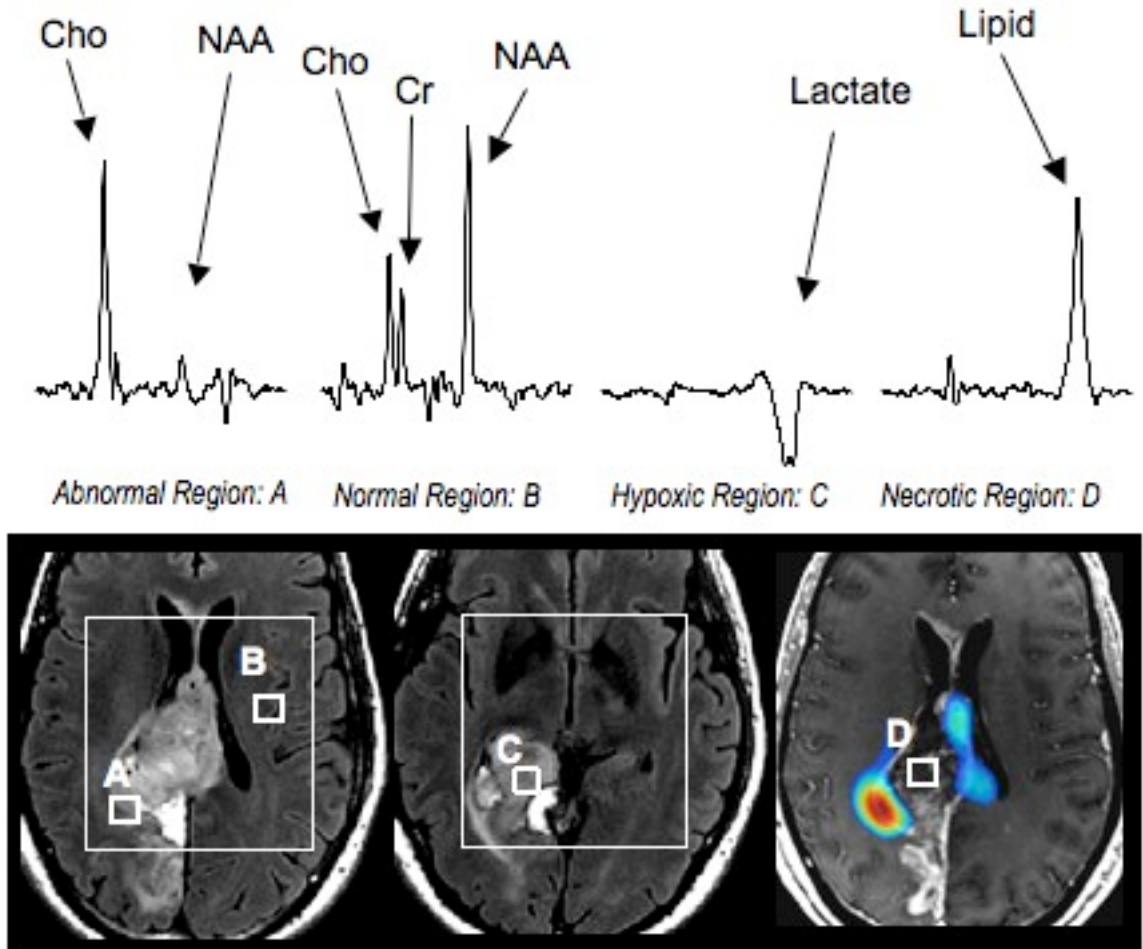


**Figure 5.3:  $^1\text{H}$  MRSI data from a grade IV glioma patient demonstrating the extreme spatial heterogeneity of the tumor shown within the representative voxels. T2-FLAIR images with the PRESS-selected volume superimposed are shown for two different axial slices. The T1-weighted SPGR post-Gadolinium image is shown with a superimposed CNI color overlay map.**

Figure 5.4 shows multiple axial slices from a patient with a resected grade IV glioma. The shaded voxels correspond to regions with CNI greater than 2. Note the variability in spectral patterns between the normal and abnormal region that includes part of the resection cavity.

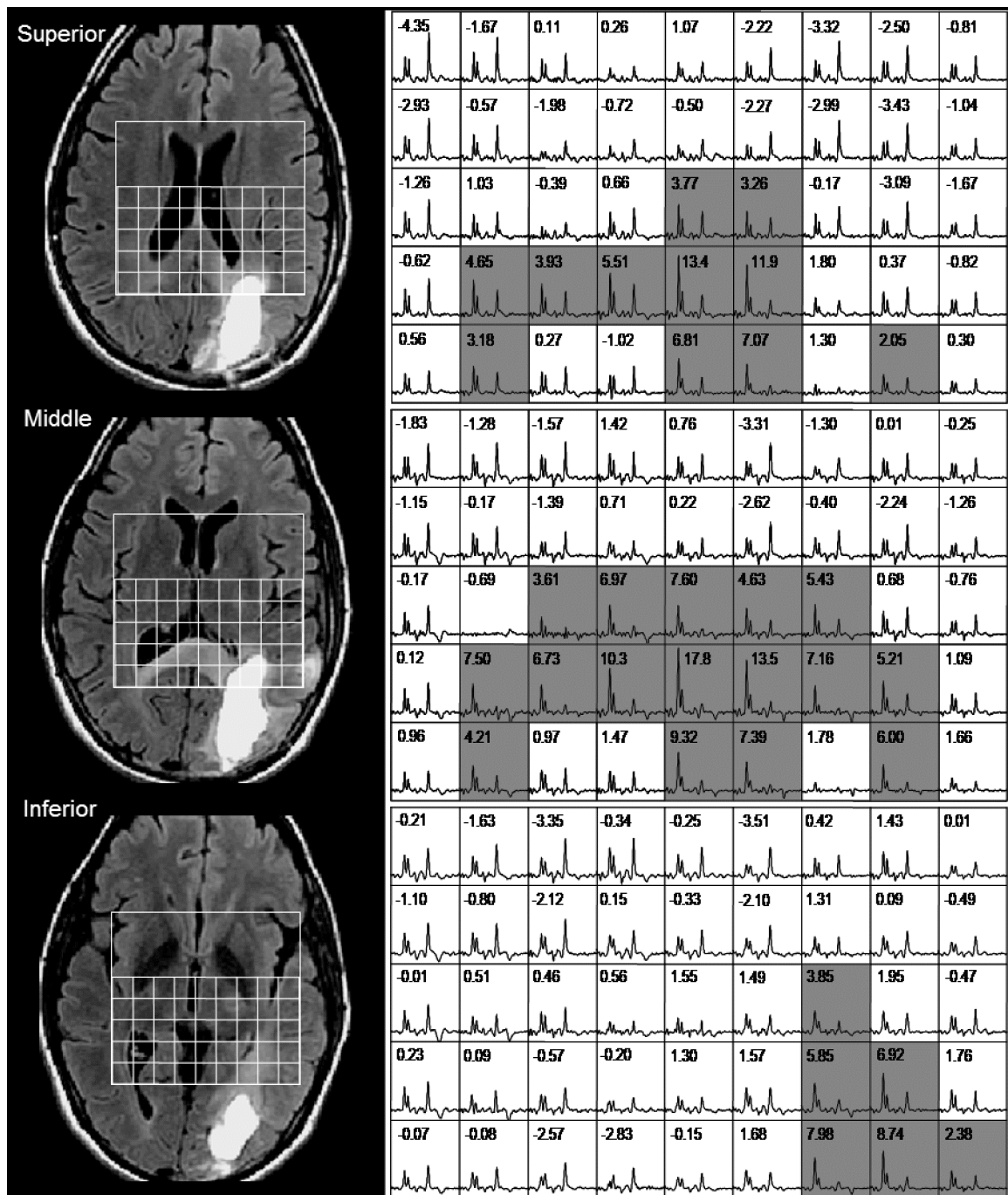


**Figure 5.4: Multiple 1H MRSI arrays from a patient with a grade IV glioma who received a subtotal resection along with external beam radiation treatment. Axial slices of MRSI data demonstrate the extreme spatial heterogeneity of the lesion shown from the representative voxels. Voxels shaded in gray were deemed metabolically abnormal, with a CNI  $\geq 2$ .**



Figure 5.5 illustrates the 3-D nature of the spectral data, in that it can be displayed in coronal orientation. The increases in Cho within this grade IV glioma are especially dramatic in the central slice. Figure 5.6 demonstrates that there are voxels with abnormal metabolite levels in regions of this oligodendroglioma where the FLAIR images have no obvious anatomic lesion.

### Lipid Contamination

All patient data was evaluated for lipid contamination by counting the voxels exhibiting readily visible lipid. Of the 15 patient scans exhibiting lipid contamination (42 total exams), seven had lipid in 5-10% of the total number of voxels, while the remaining eight patients had more than 10% of the voxels contaminated by lipid.

### Metabolite Ratios

The mean Cho/NAA was similar within regions of NAWM in volunteers ( $0.52 \pm 0.04$ ) and patients ( $0.59 \pm 0.12$ ,  $P = 0.15$ ), but was significantly higher in regions of T2-hyperintensity relative to NAWM for patients ( $1.44 \pm 0.70$ ,  $P = 0.001$ ), as shown in Figure 5.7. This difference demonstrates the ability of 3D MRSI to distinguish tumor from normal tissue at 3 T. The mean Cr/NAA was significantly higher within regions of NAWM in volunteers ( $0.43 \pm 0.03$ ) relative to the NAWM in patients ( $0.48 \pm 0.05$ ,  $P < 0.05$ ), and was also significantly higher in regions of T2-hyperintensity relative to NAWM for patients ( $0.85 \pm 0.26$ ,  $P < 0.001$ ).

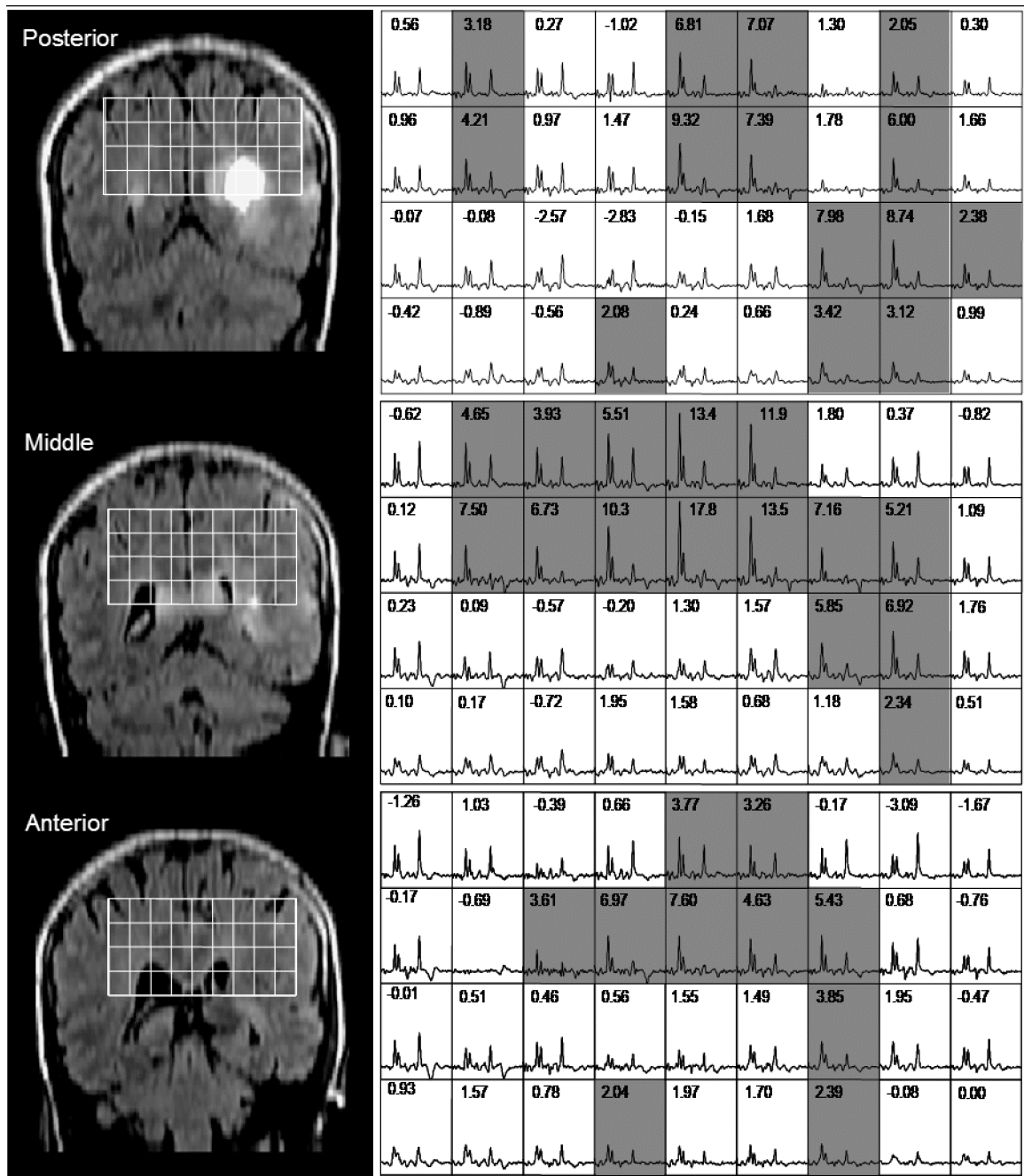


**Figure 5.5: Multiple 1H MRSI arrays from a patient with a grade IV glioma who received a subtotal resection along with external beam radiation treatment. The coronal representations of the spectral arrays are demonstrating the spatial heterogeneity in the superior- and inferior-most regions of the tumor. Voxels shaded in gray were deemed metabolically abnormal, with a CNI  $\geq 2$ .**

The mean Cho/Cr was similar within regions of NAWM in volunteers ( $1.20 \pm 0.06$ ) and patients ( $1.22 \pm 0.18$ ,  $P > 0.05$ ), but was significantly higher in regions of T2-hyperintensity relative to NAWM for patients ( $1.69 \pm 0.59$ ,  $P < 0.001$ ).

#### Abnormality Index (CNI)

Data were also analyzed using the Cho to NAA index (CNI), for the 42 examinations performed on patients. The voxels acquired within the press volume selection were divided into two groups, metabolically normal ( $CNI < 2$ ) and metabolically abnormal ( $CNI \geq 2$ ). The mean number of voxels acquired within the press volume for the patient data was ( $241 \pm 45$ ), with approximately 10% ( $25 \pm 1$ ) being metabolically abnormal and the rest being metabolically normal ( $199 \pm 38$ ).

Regions that were defined as metabolically abnormal,  $CNI \geq 2$ , were further evaluated using indices for CNI and the choline to creatine index (CCrI). The mean CNI in metabolically abnormal tissue ranged from 2.5-6.4, with a mean of  $3.3 \pm 0.76$ . Maximum CNI values for the PRESS-selected volume ranged from 2.6-18.0, with a mean of  $6.2 \pm 3.32$ . The mean CCrI in metabolically abnormal tissue ranged from 0.8-4.3, with a mean of  $1.9 \pm 0.87$ . Maximum CCrI values for the PRESS volume ranged from 2.4-16.4, with a mean of  $4.6 \pm 2.63$ .

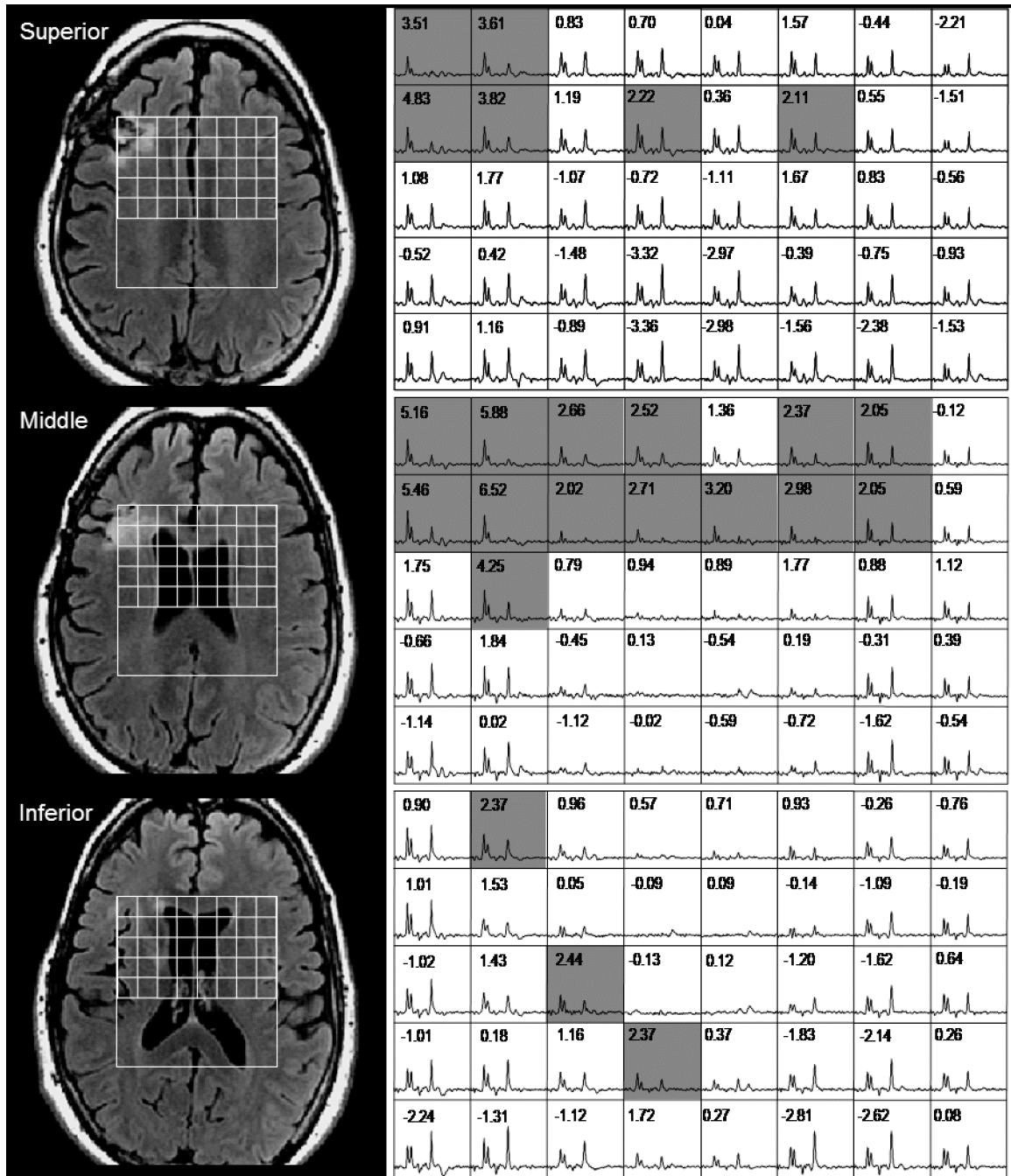


**Figure 5.6: Multiple 1H MRSI arrays from a grade II oligodendroglioma patient who received a subtotal resection along with chemotherapy treatment. MRSI demonstrates the metabolic activity of the tumor moving across the midline of the hemispheres. Voxels shaded in gray were deemed metabolically abnormal, with a CNI  $\geq 2$ .**

Signal-to-Noise Ratio (SNR)

Signal-to-noise ratio (SNR) measurements were calculated to test receiver coil sensitivity (homogeneity) from both the 8-channel phased array coil and the standard volume head coil. The 8-channel phased array coil had an SNR range of 199.0-204.4 in the superior to inferior (SI) direction, and 203.3-238.5 in the medial to lateral (ML) direction. The volume head coil had reduced SNR values with a range of 79.8-110.3 in the SI direction, and 86.2-106.6 in the ML direction.

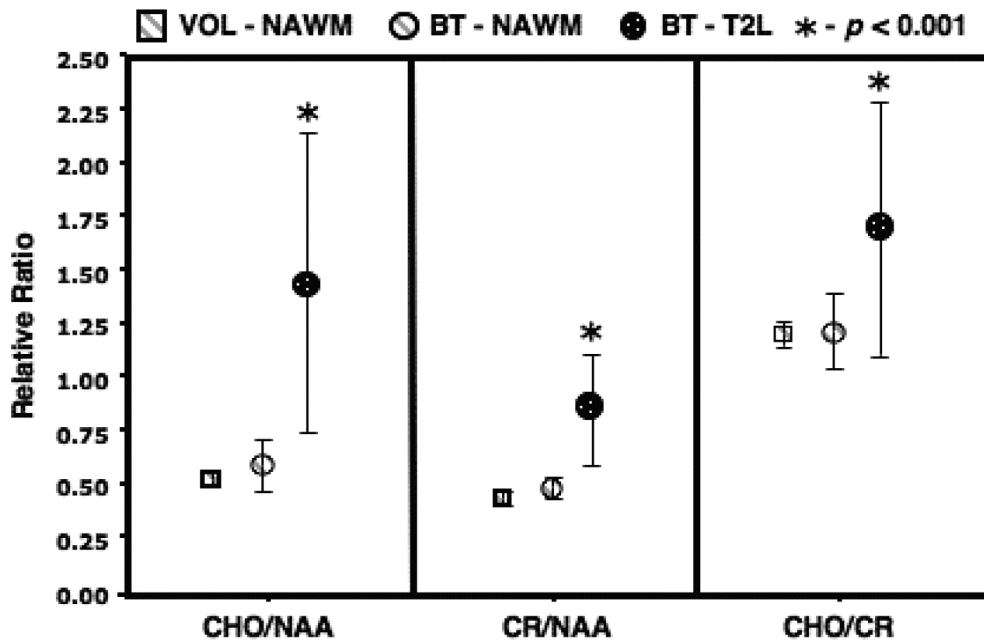


**Figure 5.7: Regional analysis of metabolic ratios, as defined through morphologic segmentation, is shown for volunteers and patients. The mean voxels used for each patient were 54, 20, and 15 for volunteer NAWM (VOL-NAWM), brain tumor NAWM (BT-NAWM), and brain tumor T2L (BT-T2L), respectively. T2L regions were significantly higher for all metabolite ratios.**

The mean SNR values for choline (Cho), creatine (Cr), and N-acetyl aspartate (NAA) within NAWM regions were  $42.0 \pm 7.8$ ,  $34.8 \pm 5.6$  and

80.0±11.1 (mean ± s.d.) for normal volunteers, respectively. These values were comparable to regions of NAWM for patients where Cho, Cr, and NAA had SNR values of 42.2±11.6, 34.8±8.0, and 71.9±14.2, respectively. The SNR values for these metabolites were not found to be significantly different between volunteers and patients for regions of NAWM. The averages and standard deviations (SD) of each metabolite are shown in Table 5.2. The SNR values that were obtained demonstrate the reliability of <sup>1</sup>H MRSI data from brain tumor patient acquisitions. These values were 1.95 times higher than the values that we had observed in our previous brain tumor studies that were performed at 1.5 T with a volume head coil, which used comparable pulse sequences and acquisition parameters (36).

Regions of T2L within patients had SNR values for Cho, Cr, and NAA of 38.4±13.4, 23.9±7.7, and 29.9±11.9, respectively. Creatine and NAA had significantly lower SNR values when compared with NAWM regions (P < 0.001). The SNR of Cho and NAA in metabolically normal tissue, CNI < 2, was 31.6±7.4 and 46.2±13.4, respectively. These values were significantly different, (P < 0.05), from the SNR values for Cho and NAA within metabolically active tissue, CNI ≥ 2, 47.8±15.2 and 33.5±13.8, respectively. These SNR comparisons are shown in Table 5.2.

**Table 5.2: Signal-to-Noise ratio of metabolite levels for normal volunteers and brain tumor patients.**

	<b>Signal-to-noise ratio (SNR) (mean <math>\pm</math> SD)</b>			
	<b>Voxels</b>	<b>Choline</b>	<b>Creatine</b>	<b>NAA</b>
Data - normal volunteers				
All voxels	256 $\pm$ 0	34.6 $\pm$ 5.6	31.2 $\pm$ 5.3	62.9 $\pm$ 8.1
NAWM	54 $\pm$ 10	42.0 $\pm$ 7.8	34.8 $\pm$ 5.6	80.0 $\pm$ 11.1
Data - patients with brain tumors				
All voxels	241 $\pm$ 45	37.7 $\pm$ 7.8	27.9 $\pm$ 6.3	47.3 $\pm$ 13.1
NAWM	20 $\pm$ 12	42.2 $\pm$ 11.6	34.8 $\pm$ 8.0	71.9 $\pm$ 14.2
T2L	15 $\pm$ 19	38.4 $\pm$ 13.4	23.9 $\pm$ 7.7	29.6 $\pm$ 11.9
CNI $\geq$ 2	199 $\pm$ 38	31.6 $\pm$ 7.4	26.9 $\pm$ 6.3	46.2 $\pm$ 13.4
CNI $\geq$ 2	25 $\pm$ 16	47.8 $\pm$ 15.2	29.2 $\pm$ 9.0	33.5 $\pm$ 13.8

#### **5.4 Discussion**

MRSI has been shown to be a valuable adjunct to conventional MRI when used for characterizing brain tumors (33). The majority of the  $^1\text{H}$  MRSI studies presented in the literature have been performed at the standard clinical field strength of 1.5 T using single channel volume head coils (1,2,29-31). With the availability of clinical 3 T scanners and multi-channel phased array coils for neurological application, there is a desire to take advantage of the theoretical improvements in sensitivity that they would provide for both the anatomic and metabolic images. Preliminary studies obtained using 3 T scanners produced conflicting results concerning whether the anticipated increase in SNR could be realized for MRS data (50). Other concerns that were expressed related to whether the increased susceptibility effects at 3 T would compromise the data quality.

The results presented in this study have made it clear that high SNR MRSI data can be acquired at 3 T using a commercial 8-channel phased array coil in a group of patients with brain tumors that are representative of the population encountered routinely in clinical practice. The pulse sequences and acquisition parameters used for this study were comparable with those used in our previous analyses of brain tumor patients that were performed at 1.5 T and show similar metabolite patterns between tumor and normal tissue. This means that the observations used for tissue characterization and for evaluating differences in the spatial extent of tumor in those studies can be directly applied at the higher field strength (1,2,29-32). With 3 T and multi-channel RF coils becoming the preferred tools for anatomic imaging of patients with brain tumors, this is an important finding and one that suggests MRSI may be applied in a clinical setting as a useful tool for complementing conventional MRI data.

Our previous studies at 1.5 T have shown that clinically relevant findings could be obtained with MRSI at a nominal spatial resolution of 1 cc and acquisition time of 17 minutes (1,24,32,47). The clear improvements in SNR that were observed at 3 T with the 8-channel coil were approximately 2-fold higher than the values presented at 1.5 T with a single channel volume head coil. This means that the acquisition time for the MRSI data acquired for routine follow-up of patients at 3 T could be cut down by as much as a factor of 4 while still retaining good discrimination between normal and tumor tissue. For situations such as planning focal radiation therapy, where the spatial resolution of the data is more important, the nominal voxel size



could be cut down by a factor of 2 while retaining the 17 minute scan time. Future studies will investigate the relative benefits of employing such strategies in order to enhance the use of MRSI as a practical clinical tool for detecting tumor malignancy.

In conclusion, the results of this study demonstrate the acquisition of clinically acceptable spectra using 3D  $^1\text{H}$  MRSI at 3 Tesla from brain tumor patients that were representative of the population encountered routinely in clinical practice. The clear improvements in sensitivity that were observed at 3 T with the 8-channel coil could be utilized to either reduce the spatial resolution and acquisition time or to detect more subtle differences in metabolite levels at the same spatial resolution and acquisition time.

## Chapter 6: Design of cosine-modulated very selective suppression pulses for 3D $^1\text{H}$ MRSI at 3.0 Tesla

---

*In this chapter we present the design of a cosine-modulated VSS (CM-VSS) pulse that was optimized for  $^1\text{H}$  MR Spectroscopic Imaging ( $^1\text{H}$  MRSI) at 3 Tesla in order to obtain improved outer volume suppression (OVS). The goal of the suppression pulses was to improve scalp lipid suppression with a smaller number of OVS pulses using power requirements that fit within the level acceptable for human use. PRESS localization was combined with an improved OVS scheme in order to obtain larger coverage for  $^1\text{H}$  MRSI of human brain tissue. These pulses were compared to conventional methods.*

---

### **6.1 Background**

At lower field strengths, successful clinical application of OVS was shown through the very selective suppression (VSS) pulse design (4). The large bandwidth of the VSS pulses which greatly reduces chemical shift errors, the sharp transition band, and relatively low peak RF peak power demonstrated significant advantages over previous spatial saturation pulses (51-54). These VSS pulse characteristics allowed them to be used with body coil excitation (4). The increased SNR that is associated with higher field strength and multi-channel phased array coils is becoming more frequently used for clinical applications (55), making the characteristics of the VSS

pulse not only beneficial, but also key for optimal performance and reduced chemical misregistration effects at the edges of the selected region.

In this chapter we present a cosine-modulated VSS (CM-VSS) pulse that was optimized for MRSI at 3 Tesla in order to obtain improved suppression with a smaller number of pulses. We combined PRESS localization with an improved OVS scheme in order to obtain larger coverage for  $^1\text{H}$  MR Spectroscopic Imaging ( $^1\text{H}$  MRSI) of the human brain. This has been achieved by integrating fixed cosine-modulated, and graphically placed non-cosine-modulated, VSS pulses that are optimized for high field strengths (56). The clinical applicability of the CM-VSS pulse scheme was then evaluated in MRSI studies of supratentorial brain tissue from various head sizes and shapes.

## **6.2 Methods**

### *Pulse Design*

A non-linear phase SLR (57) RF pulse with a time-bandwidth of 18 was designed with the phase optimized to minimize the peak RF power using methods described previously (58,59). This RF pulse was used as the basis for creating a cosine-modulated very selective suppression (VSS) pulse (see Figure 6.1a). The low stopband ripple (0.01) and non-linear phase of the basis RF pulse were designed so that there would be minimal interaction between the dual suppression bands of the cosine-modulated pulse (see Figure 6.2c). The VSS pulse had a nominal B1 of 0.116 G, a pulse width of

3.0 ms, and a bandwidth that of 5868 Hz. The flip angles of the VSS pulse that were used varied from 91–105°.

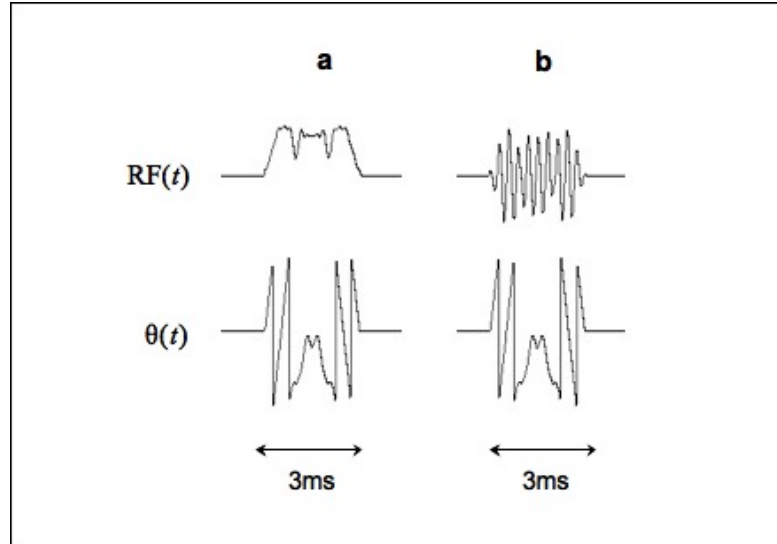


**Figure 6.1: (a) RF pulse prior to cosine-modulation, (b) cosine modulated VSS pulse.**

Two parallel symmetric suppression bands were produced using a single RF pulse by modulating the VSS pulse by a cosine function ( $\cos 2\pi f_o t$ ). The cosine-modulated VSS (CM-VSS) pulse was generated in real time and produced two suppression bands of equal thickness that were spatially placed based on the volume edge prescription using

$$FT(\cos 2\pi f_o t) = \frac{\delta(f - f_o) + \delta(f + f_o)}{2} \quad (6.1)$$

Here  $f$  is the frequency relative to the center of the acquisition volume, and  $\pm f_o$  is chosen based on the suppression band separation. This separation was computed as the difference from the center of the acquisition volume to the center of the suppression band. The RF pulse waveforms before (a) and after

cosine-modulation (b) are shown in Figure 6.1.

The excitation of the cosine-modulated pulse was optimized to generate similar suppression as a single VSS pulse while maintaining an adequate power level. In theory, this would be accomplished by doubling the VSS pulse flip angle to achieve the desired suppression. VSS pulse flip angles that were cosine-modulated varied between  $182-193^\circ$ .

Crusher gradients were used to eliminate any residual transverse components of magnetization following each VSS pulse, all with a duration of 1 ms. Conventional suppression pulse schemes that generated one suppression band for each VSS pulse utilized an equal number of crusher gradients as VSS pulses (4). The CM-VSS pulse scheme utilized only one crusher gradient for every two suppression bands that were generated from a cosine-modulated pulse.

The phased modulated low peak power characteristic of the CM-VSS pulse allowed for six pairs of fixed-suppression bands in addition to the 6 graphically prescribed bands – a total of 18 suppression bands. The pulse sequence for this suppression pulse scheme is shown in Figure 6.2. Four pairs of the 12 fixed cosine-modulated suppression bands were used to generate an octagonal selection region in axial slices.

The six additional graphically prescribed bands were also used axially to generate an elliptical volume selectivity that uniquely conformed the selected region to the shape of the individual. The remaining four cosine-modulated suppression bands were implemented in the superior and inferior sides of the volume selection.

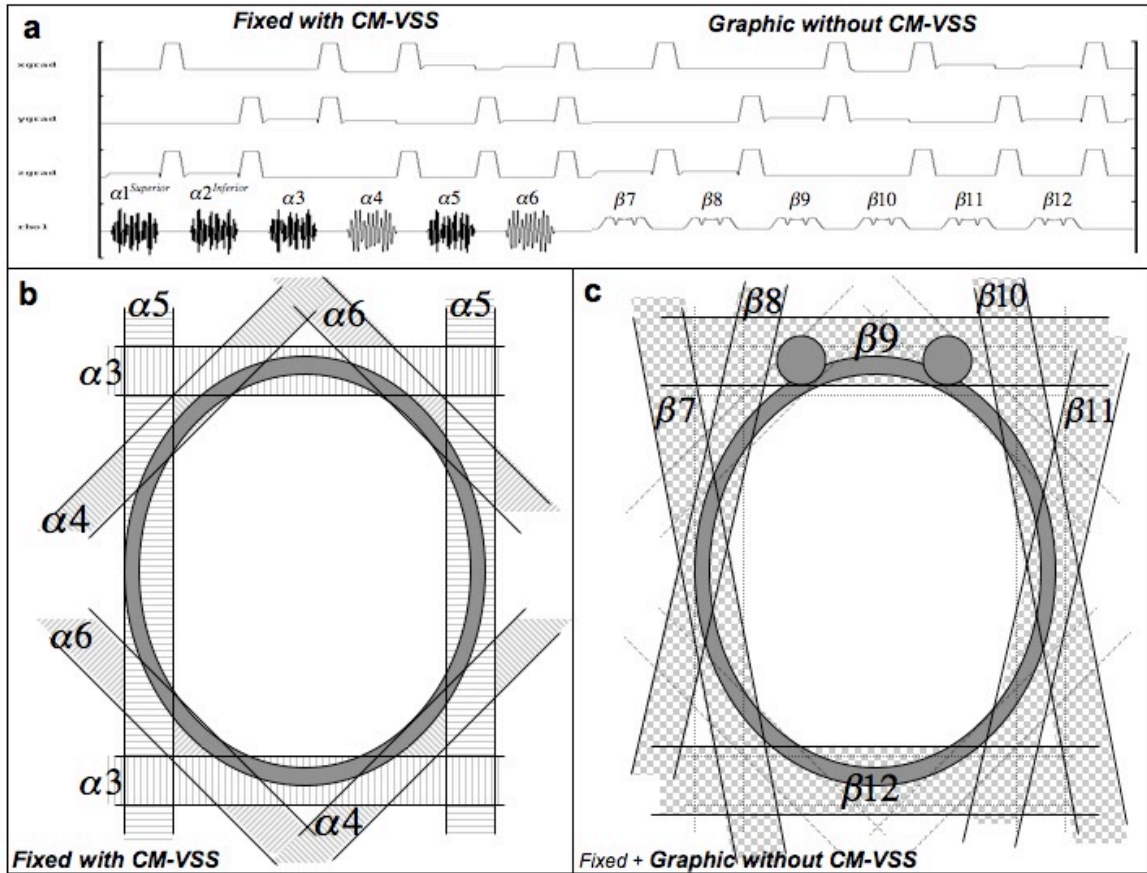


**Figure 6.2: The section of the MRSI pulse sequence corresponding to the outer volume suppression scheme – shown in (a). The phased modulated low peak power characteristic of the CM-VSS pulse allowed for 12 fixed-suppression bands in addition to the 6 graphically prescribed bands – a total of 18 suppression bands. Eight of the 12 fixed cosine modulated suppression bands were used to generate an octagonal selection region in axial slices – shown in (b). The six additional graphically prescribed bands were also used axially to generate an elliptical volume selectivity that uniquely conformed the selected region to the shape of the individual – shown in (c). The remaining four cosine modulated suppression bands were implemented in the superior and inferior sides of the volume selection.**

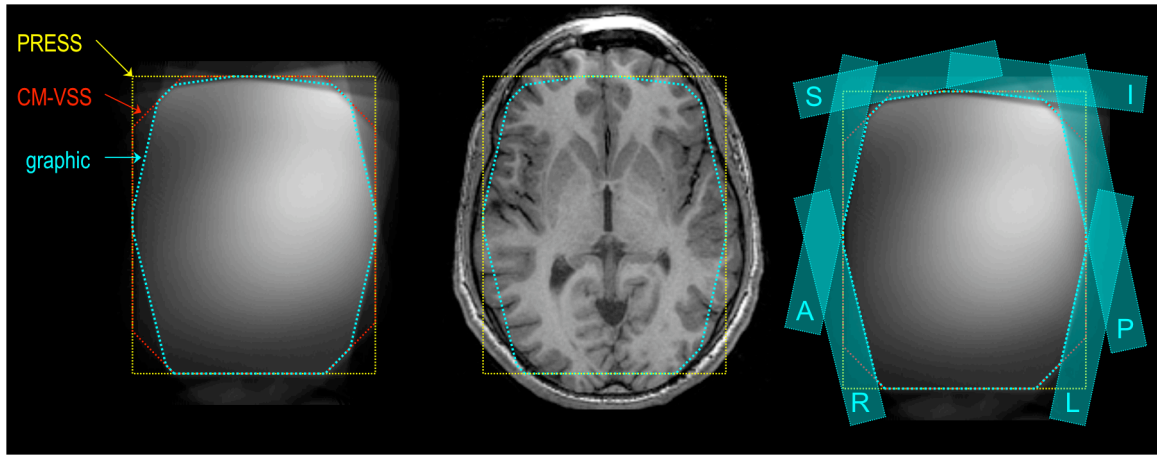


**Figure 6.3: Phantom image acquisition utilizing CM-VSS pulses demonstrating spatial placement of fixed (red – CM-VSS) pulses, and graphic (blue). PRESS excitation volume is shown in yellow. Volunteer T1-weighted image is shown with overlay of predicted coverage. Shown on the right is a phantom image explicitly showing the placement of the graphic suppression bands.**

#### Data Acquisition

The VSS pulse scheme was tested in phantom experiments, and on normal volunteers using a PRESS pulse sequence on a GE 3 T MR scanner. Signal was received using an eight-channel phased array head coil, and a whole-body birdcage coil was used for RF transmission. CHES pulses were used for water suppression, and acquisition time was 4.5 minutes with TR = 1100 ms, and TE = 144 ms for a single slice. These acquisitions employed spectral arrays of 16 x 16 x 1 acquired with full k-space sampling with fields of view adjusted to correspond to a 10 mm isotropic resolution. Chemical shift misregistration effects were reduced by prescribing a PRESS box larger than the region of interest (overpress of 20%), and using CM-VSS pulses to suppress signals arising from beyond the region of interest. At 3 T, an overpress factor of 1.2 has been shown to significantly reduce the chemical

shift artifact (56). Data were reconstructed using processing software that was customized for MRSI exams (47).

### **6.3 Results and Discussion**

#### CM-VSS Pulse Scheme

Spin-echo images of a phantom are shown in Figure 6.4 before (a) and after (b) cosine-modulation of one VSS pulse. The phantom studies demonstrated the high spatial selectivity of the suppression bands without notable interaction between the bands at distances that were practically implemented (Figure 6.4). This is shown from the linear profile in Figure 6.4c corresponding to a projection from the center of the image in Figure 6.4b. Suppression bands were tailored to obtain an ROI representative of an octagon shown in Figure 6.4d. Two symmetric saturation bands were generated at distances down to 2 mm apart with no interaction between the bands. The efficiency of saturation of water from the VSS pulse was 98% in phantom analysis.

The time taken to play out the total number of suppression bands using the modified CM-VSS scheme was less than if the same number of suppression bands were generated using a conventional pulse scheme, which in turn improved water suppression by 17%. In addition, time was conserved further from the additional crusher gradients and the ramp time from the spatial selective gradient. The time saved from crusher gradients and gradient ramp time was 1.7 ms per pulse. Cosine-modulation of the VSS



pulse along with the phased modulated low peak power characteristic allowed for 18 saturation bands to be implemented in human subjects while still keeping the power deposition under the FDA approved specific absorption rate (SAR) limit. The current CM-VSS pulse scheme duration was 56.4 ms producing 18 suppression bands, where conventional non-CM-VSS scheme would have duration of 84.6 ms to produce the same number of suppression bands. Practical implementation of the conventional VSS pulse scheme allowed a maximum of 12 VSS pulses at 3 T, limiting the number of suppression bands to 12 with a total duration of 56.4 ms. The current outer volume suppression pulse scheme was not only retaining the total duration of pulses to 56.4 ms to maintain adequate water suppression, but it was additionally providing six extra suppression bands. Table 6.1 lists the pulse parameters for the different outer volume suppression pulse schemes. Note the use of the CM-VSS scheme allows for a greater number of suppression bands in a shorter duration.

**Table 6.1: Timing comparison for CM-VSS pulse scheme.**

<b>OVS Pulse</b>	<b>#Pulses/Bands</b>	<b>Selection</b>	<b>Duration (ms)</b>
<i>CM-VSS</i>	12/18	Octagon	56.4
<i>VSS (only)</i>	18/18	Rectangular	84.6
<i>VSS (convention)</i>	12/12	Rectangular	56.4

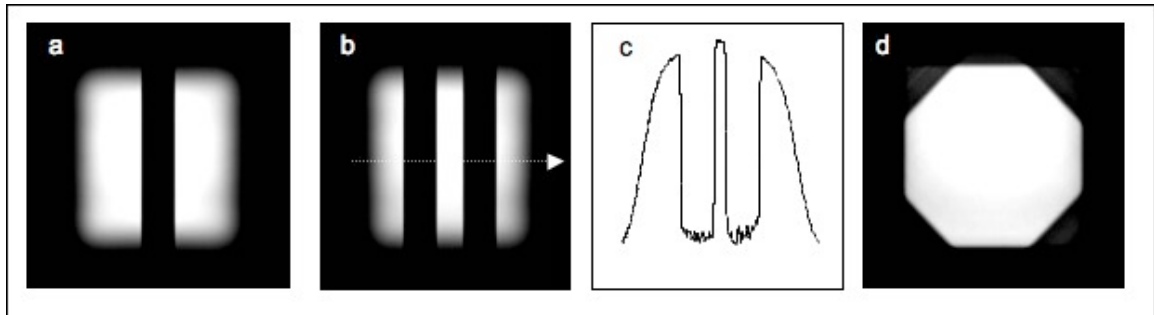


**Figure 6.4: Demonstration of the functionality of the pulse. (a) One single band VSS pulse. (b) One dual-band cosine-modulated VSS pulse shown as two symmetric bands. (c) A linear intensity profile generated from figure (1b). (d) Four dual-band cosine modulated VSS pulses making an octagon shaped volume selection.**

Volunteer Data

The data in Figure 6.5 show the feasibility of performing an MRSI scan on a volunteer with the PRESS volume conformed to an octagonal-shaped axial selection region. The high spatial selectivity of the suppression bands is demonstrated in the edge transitions of the box image in Figure 6.5b. The spectral array in Figure 6.5c show homogenous metabolite excitation within the volume selection, and complete suppression of signal outside of the volume selection. The efficiency of saturation of water from the CM-VSS pulse was 93% in volunteers.

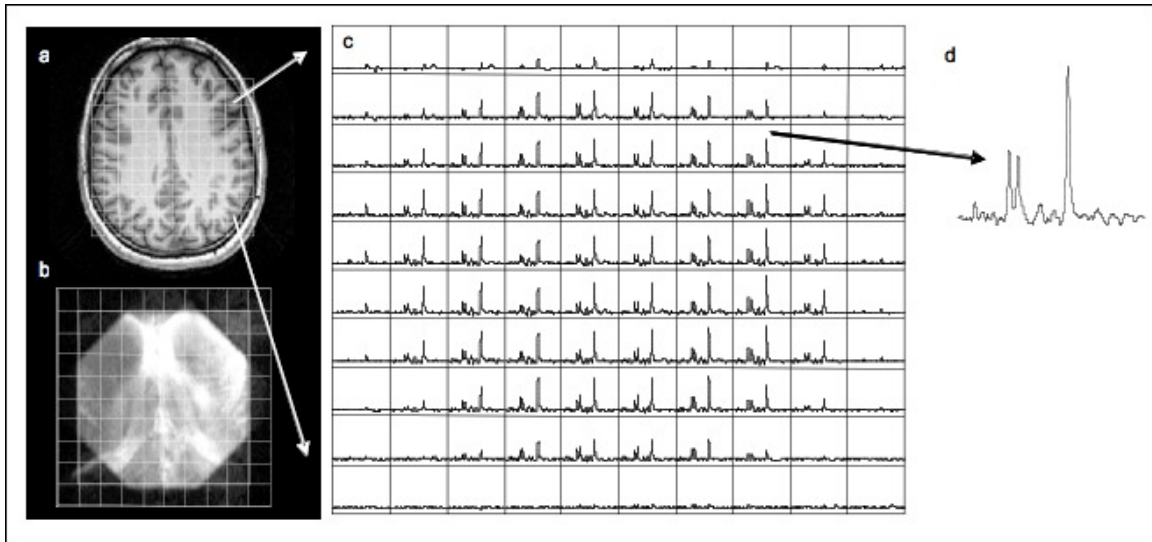


**Figure 6.5: In vivo volunteer data with four VSS pulses performing eight saturation bands into an octagon shaped volume selection. (a) T1 SPGR with overlay of MRSI. (b) MRS selection volume demonstrating the irregular contour. (c) Full MRSI array demonstrating an array high quality spectra with desired contour selection. (d) Spectra coming from a voxel adjacent to saturation band demonstrating high selectivity of cosine modulated VSS.**

Maximum coverage was achieved in volunteers from MRSI data using the CM-VSS pulse scheme. The metabolite maps in Figure 6.6 demonstrate MRSI with high spatial selectivity of the suppression bands from multiple acquired slices. Conventional volume selection at 3 T for the volunteer scans has been limited to 67.5 cc for a slice of MRSI data using 3D acquisitions with 12 VSS pulses. The mean volume selection in volunteers for a slice acquired with the CM-VSS pulse scheme was 102.8 cc, allowing a 1.5 increase in coverage. The irregular selection was conformed to an octagon region as shown by a NAA map overlay in a volunteer in Figure 6.6.

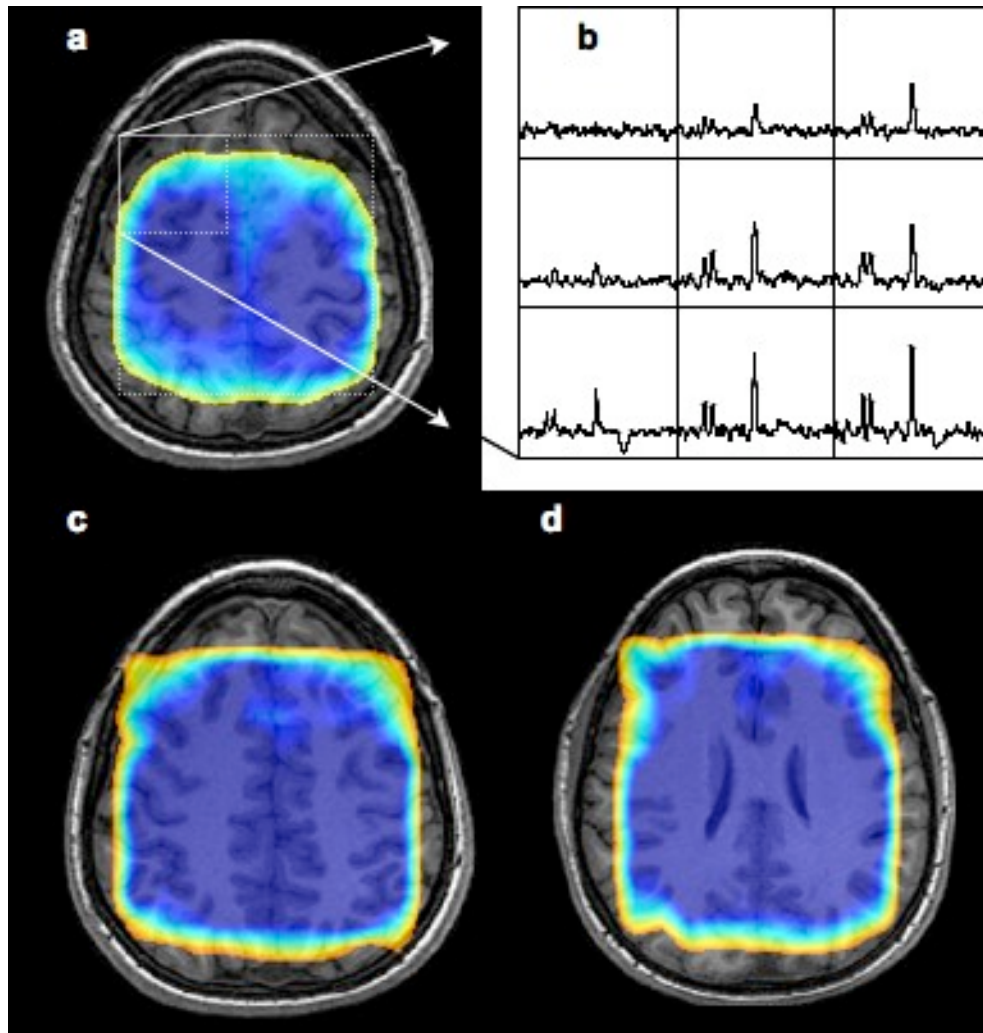


**Figure 6.6: (a,c,d) Normal volunteer with cosine modulated PRESS MRSI, overlay of NAA peaks, (b) spectral array from superior slice selection in (a). Note lipid is within PRESS selection but adequately suppressed.**

The data shown in Figure 6.7 show the feasibility of performing an MRSI scan using the CM-VSS scheme with voxels covering a very large volume of interest. The proposed CM-VSS pulse scheme was most efficient for lipid suppression when compared to conventional outer volume suppression pulse schemes. The lipid metabolite map overlays show this improved lipid suppression when using fixed CM-VSS and graphically

prescribed VSS pulses – total of 12 RF pulses for OVS. The quality of the MRSI data was analyzed and compared to the conventional MRSI sequence. Signal-to-noise calculations are shown in Table 6.2 demonstrating comparable data quality to conventional MRSI.

**Table 6.2: SNR comparison between CM-VSS and conventional pulse scheme for Choline and NAA peak heights in volunteer NAWM.**

	Signal-to-Noise		SAR [W/kg]
	Choline	NAA	
CM-VSS	15.1	26.0	1.4
VSS ( <i>convention</i> )	13.5	25.9	1.2

Graphically prescribed bands were an important facet of the current implementation of the CM-VSS pulse scheme. The purpose of the graphic suppression bands was two-fold, they were used to tailor the outer volume suppression to different head shapes and sizes, and they were critical in situations where additional suppression bands were needed for residual magnetization from excited lipid signal. It was often the case that peri-cranial lipid was excited when the volume prescriptions were increased to reach the extent of the brain tissue. In situations where lipid regions were excited, more than one suppression band was desirable in order to reduce the consequence of lipid contamination. Excited lipid regions would receive two suppression bands, one from the graphic prescription, and the other from the oblique CM-VSS pulse.

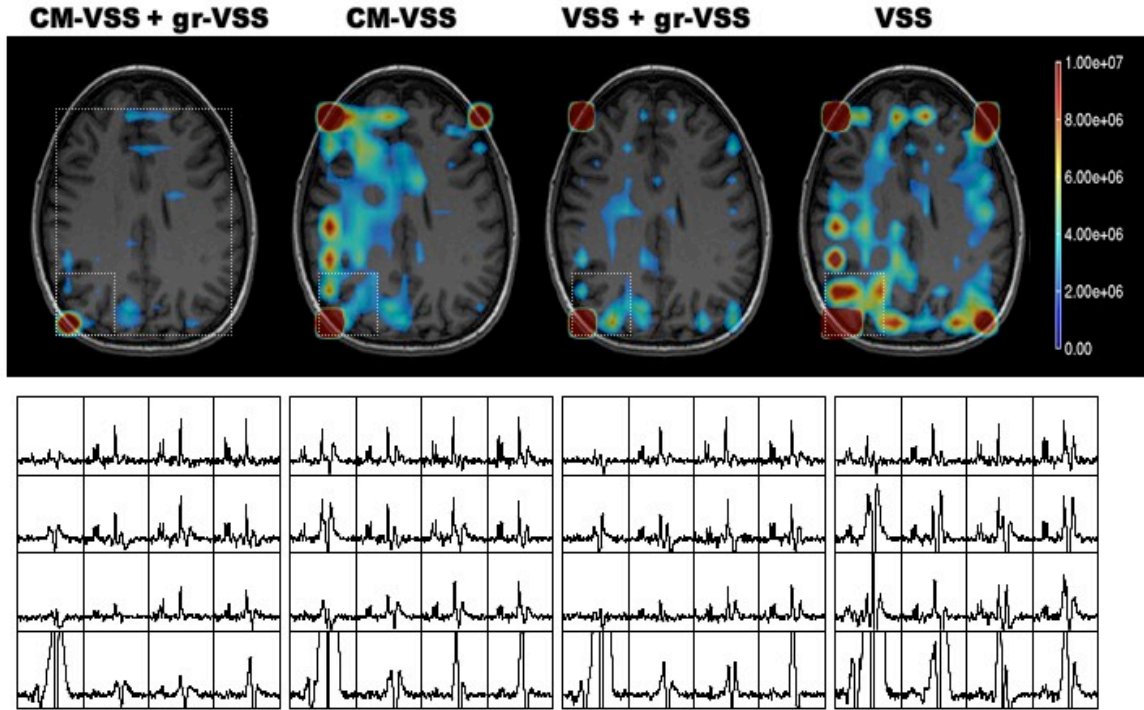


**Figure 6.7: MRSI data acquired with both the CM-VSS scheme and conventional outer volume suppression scheme. The large box selection on the  $T_1$  weighted images denotes the region excited by RF pulses in the PRESS sequence. The smaller box shows the voxel locations corresponding to the spectra below. Overlay of lipid metabolite map is shown for corresponding  $T_1$  images. (a) Spectra acquired using fixed CM-VSS pulses and graphic non-CM-VSS pulses – total of 12 RF pulses. (b) Spectra acquired with only fixed CM-VSS pulses – total of 6 RF pulses. (c) Spectra acquired using conventional VSS pulses for fixed and graphic prescription – total of 12 RF pulses. (d) Spectra acquired using VSS pulses for fixed prescription – total of 6 RF pulses.**

## **6.4 Conclusions**

Improved outer volume suppression pulses for PRESS MRSI were designed and implemented. Normal volunteers at 3 T showed the feasibility of generating improved coverage for maximum lipid suppression and improved water suppression by employing cosine-modulated VSS pulses.

SAR limits were maintained while increasing coverage for high-field MRSI. The cosine modulated VSS pulse scheme thus provides a simple and reliable approach for increasing coverage and improving coverage for clinical MRSI examinations.

## Chapter 7: Improved coverage of brain tumors with $^1\text{H}$ MRSI using Cosine Modulated Very Selective Suppression Pulses at 3T.

---

*In this chapter we present the application of the cosine-modulated VSS (CM-VSS) pulse, from the previous chapter, in brain tumor patients. CM-VSS provides a simple and reliable approach for increasing coverage and improving coverage for clinical examinations. Point resolved spectroscopy (PRESS) localization was combined with the improved OVS scheme, and larger coverage using  $^1\text{H}$  MR spectroscopic imaging ( $^1\text{H}$  MRSI) was obtained in treated brain tumor patients.*

---

### **7.1 Background**

Although 3D point resolved spectroscopy (PRESS) magnetic resonance spectroscopic imaging (MRSI) is able to provide excellent quality metabolic data for patients with brain tumors and has been shown to be important for defining tumor burden (1,29-32), the method is currently limited by how much of the anatomic lesion can be covered within a single examination. Figure 7.1 illustrates a common example of a tumor location (red), conventional MRS prescription (white), and the potential coverage when using improved outer volume suppression - CM-VSS (blue). One of the major reasons for this is that the PRESS selection is rectangular, whereas the head



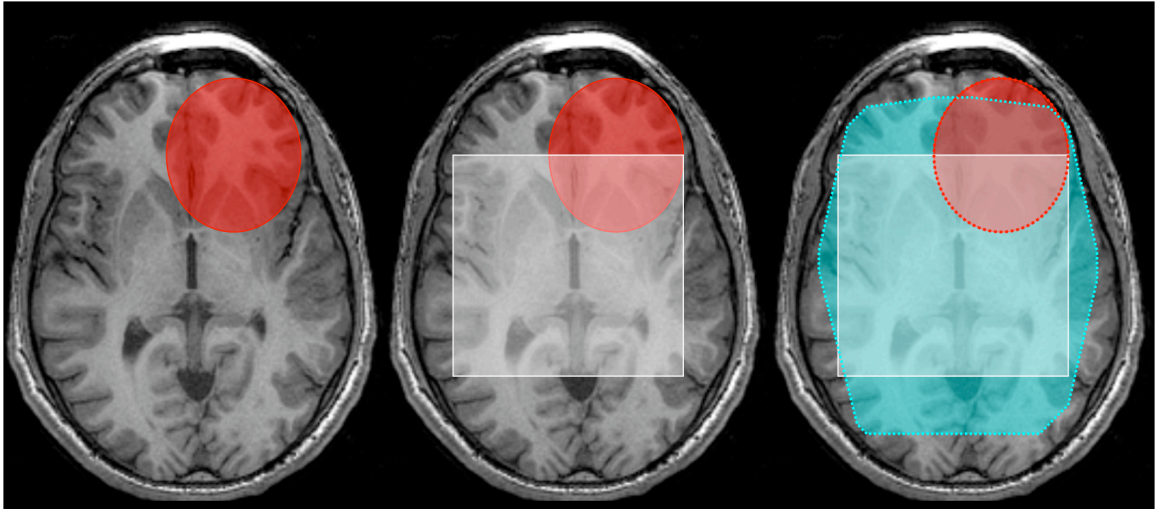


**Figure 7.1: An illustration demonstrating a common tumor location (red), conventional MRSI prescription (white), and the potential coverage when using MRSI with improved outer volume suppression pulses – CM-VSS (blue).**

is more elliptical in shape. Another complication is the effect of chemical misregistration between the selected volumes for different metabolites. While these issues may be partially addressed by using graphically prescribed outer volume suppression (OVS) pulses to conform the PRESS selected volume to the borders of the brain and avoid peri-cranial lipid contamination, the limitations on power deposition at 3 T mean that the number of such pulses that can be applied is limited (4,60).

In this chapter we further investigate the outer volume suppression pulses and scheme (CM-VSS) developed in the previous chapter. PRESS will be combined with CM-VSS and utilized in treated patients diagnosed with glioma brain tumors in order to understand if improved and larger coverage of the metabolic data from the tumor region and the adjacent normal tissue is feasible, reproducible, and reliable.

## **7.2 Methods**

### Cosine Modulated VSS Pulse

A non-linear phase-modulated SLR (57) RF pulse was utilized with the phase optimized to minimize the peak RF power using methods described previously (58,59). This RF pulse was used as the basis for creating a cosine-modulated very selective suppression (VSS) pulse (see Figure 6.1a). The low stopband ripple (0.01) and non-linear phase of the basis RF pulse were designed so that there would be minimal interaction between the dual suppression bands of the cosine-modulated pulse (see Figure 6.2c). The VSS pulse had a nominal B1 of 0.116 G, a pulse width of 3.0 ms, and a bandwidth that was 5868 Hz. The flip angles of the VSS pulse varied in application from 91–105°.

Two parallel symmetric suppression bands were produced using a single RF pulse by modulating the VSS pulse by a cosine function ( $\cos 2\pi f_o t$ ). The cosine-modulated VSS (CM-VSS) pulse was generated in real time and produced two suppression bands of equal thickness that were spatially placed based on the volume edge prescription. The same pulse scheme that was developed in chapter 6 (Figure 6.2) was used for the data acquired for the patient data presented.

### Data Acquisition

The VSS pulse scheme was used on patients with brain tumors using a PRESS pulse sequence on a GE 3 T MR scanner. Signal was received using an

eight-channel phased array head coil, and a whole-body birdcage coil was used for RF transmission. CHESS pulses were used for water suppression, and acquisition time was 4.5 minutes with TR = 1100 ms, and TE = 144 ms for a single slice. These acquisitions employed spectral arrays of 16 x 16 x 1 acquired with full k-space sampling with fields of view corresponding to a 10 mm isotropic resolution when the acquisitions were limited to a single slice of data (two-dimensional). When data was collected as three-dimensional (3D) MRSI data, spectral arrays of 16 x 16 x 8 were employed with a restricted sampling of k-space to an elliptical region. Chemical shift misregistration effects were reduced by prescribing a PRESS box larger than the region of interest (overpress), and using CM-VSS pulses to suppress signals arising from beyond the region of interest. At 3 T, an overpress factor of 1.2 has been shown to significantly reduce the chemical shift artifact (56). Data were reconstructed using processing software that was customized for MRSI exams (47).

#### *Octagon Excitation using CM-VSS: Manipulation of Octagon Configuration*

The characteristic inherent in the design of the CM-VSS pulse is the distance that separates the symmetric pair of suppression bands. This distance is determined in real time using the dimensions of the prescribed acquisition volume. Therefore, when producing an octagon configuration, there is an initial choice as to how much of the edges one would desire to exclude. The amount of edge that may be desired at any given slice through brain tissue coverage will vary based on the position within the brain. If an

MRSI slice is desired far superiorly, where the shape of the brain axially resembles more of a circular shape, one may desire a shorter distance between the symmetric suppression bands in order to better conform the excitation volume to the shape of the head. Axially in brain tissue if an acquisition slice were desired medially through the brain, then in most instances an MRSI acquisition that would be tailored to the shape of the head would resemble an elliptical shape rather than a circular shape. These theoretical examples presented support the need for a flexible and interchangeable excitation volume in real time. Figure 7.2 illustrates the distance that can be adjusted with the CM-VSS pulse presented and how it would effect the excitation volume shape.

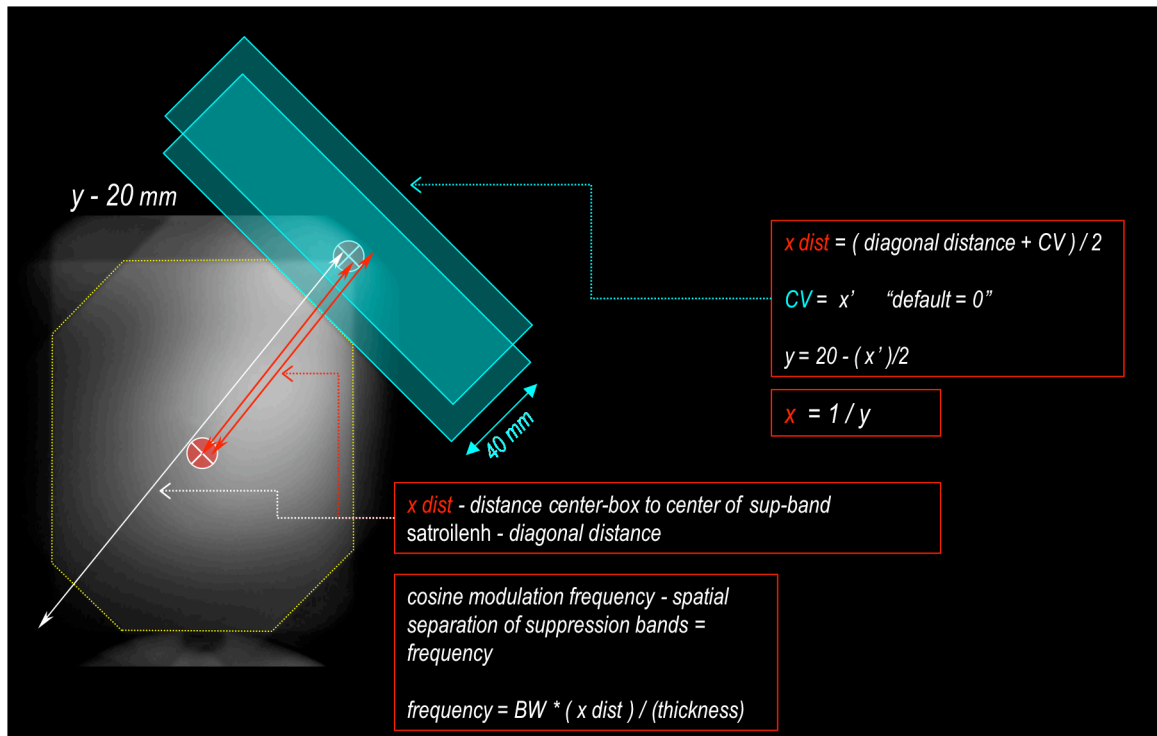


**Figure 7.2: Octagon configuration control variable. This figure illustrates internal mechanism of the design for generating the distance that is adjusted with the CM-VSS pulse presented. The schematic also illustrates the placement of the suppression band, how it would change and relate to the excitation volume in space.**

Distances could be changed in real time; default settings are set to 20 mm from the corners of the excitation volume as shown in Figure 7.3. Volunteer images were used to make simulated examples of spatial positioning of the outer volume suppression pulses, shown in Figure 7.4.

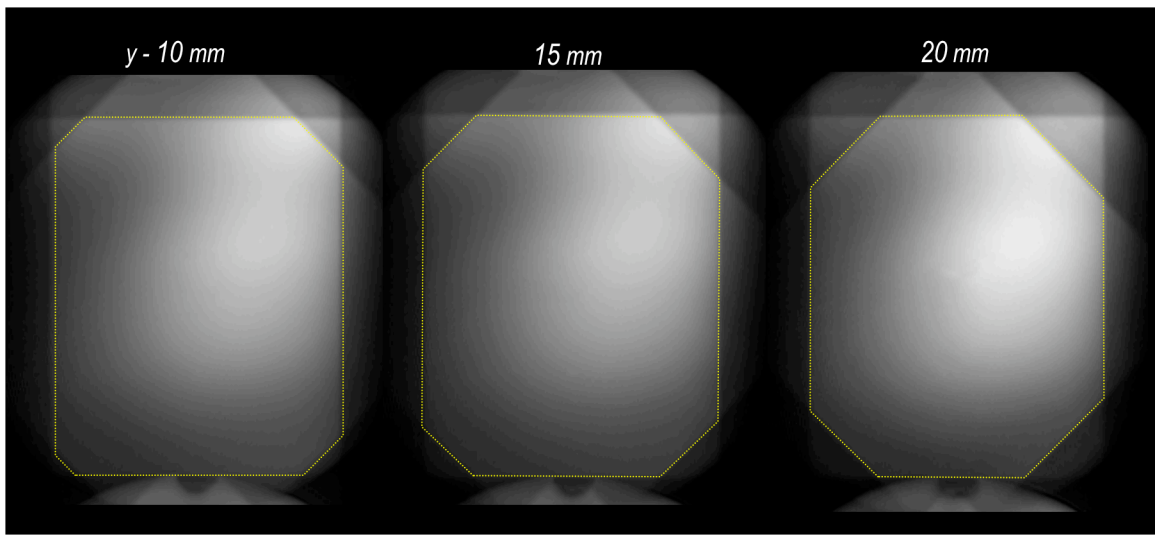


**Figure 7.3: Phantom images acquired using the control variable designed to adjust extent of octagon-corner suppression. Shown are three arbitrary distances chosen: 10 mm, 15 mm, 20 mm. Default settings are set to 20 mm.**

#### *Brain Tumor Coverage with Conventional VSS*

Brain tumor studies were analyzed retrospectively to determine the average spatial coverage resulting from MRSI examinations using conventional acquisition and post-processing methodologies (47). Twenty-eight patients were included; all patients had histologically confirmed tumors

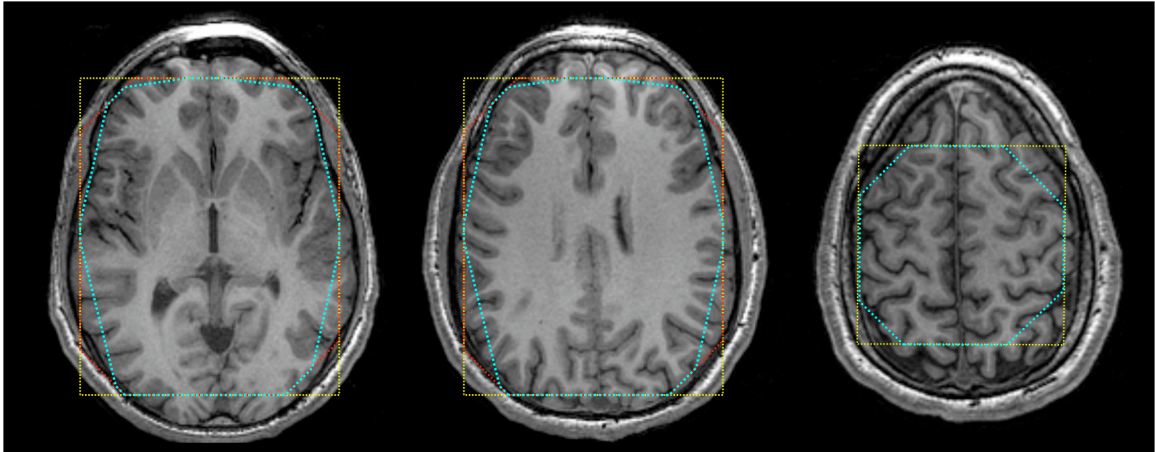


**Figure 7.4: Illustrating the various approaches for utilizing the CM-VSS pulses at different positions in the brain. Volunteer T1-weighted image was used as an example and three slices were arbitrarily chosen from midbrain to a superior extent position.**

of glial origin (14 grade II and 14 grade IV). Scans had been performed on a GE 3 T MR scanner with a conventional VSS pulse scheme. Twelve VSS pulses were used in a 3D MRSI acquisition using PRESS volume selection, with a TR/TE = 1100/144 ms. CHESS pulses were used for water suppression, and the overpress factor was 1.2.

Patients had received varying levels of treatment, including surgical resections, chemotherapy, and/or radiation therapy. The tumor region was defined as the area corresponding to the FLAIR abnormality. MRSI coverage was defined as the extent of the PRESS volume selection.

#### Brain Tumor Patients with CM-VSS

For brain tumor studies, MRSI was acquired with 10 mm slices. The number of slices acquired varied depending on the desired coverage. On average, there were five or six slices acquired. Each slice was individually prescribed in order to maximize coverage to include maximal tumor

coverage, and maximal coverage of normal surrounding tissue. For full coverage, the PRESS box selection included portions of subcutaneous lipid layers, mostly arising in the corners of the box selection. Prior to PRESS box selection, a train of six CM-VSS pulses and six graphically-prescribed conventional VSS pulses all separated by crusher gradients were used to provide outer volume suppression of unwanted signal. The magnetic field homogeneity was optimized using higher order shimming over the volume of interest prior to each MRSI slice acquisition. The rest of the protocol was the same as described for volunteers above.

### ***7.3 Results and Discussion***

#### ***Retrospective MRSI on Patient Data***

Twenty-eight patient scans were retrospectively investigated for tumor coverage with PRESS  $^1\text{H}$  MRSI using conventional VSS pulses showed a mean volume selection per slice of brain tissue of 55 cc. There was a mean coverage of 63% of the abnormal region defined as the FLAIR hyperintensity. Table 7.1 presents this data individualized by tumor grade and by tumor size (FLAIR abnormality). The mean tumor size was 80 cc. This value was used as the cutoff for dividing the populations based on tumor volume. Larger tumors trended towards MRSI examinations lacking coverage of tumor tissue.

**Table 7.1: Retrospective analysis in conventional-MRSI coverage of tumor in patients with grade II and IV gliomas.**

<b>N</b>	<b>Population</b>	<b>Coverage</b>
14	Grade II	61%
14	Grade IV	66%
19	0 – 80 cc	68%
9	80 – 167 cc	53%

*CM-VSS Pulses in Brain Tumors*

Table 7.2 shows that coverage was improved by a factor of 2.5 in patients using the new OVS scheme, with the mean volume of brain tissue covered in patients being 120 cc per MRSI slice.

**Table 7.2: MRSI coverage in three tumor patients [cc].**

<b>Slice</b>	<b>CM-VSS 1</b>	<b>CM-VSS 2</b>	<b>CM-VSS 3</b>	<b>Conventional 3</b>
1	90	80	-	64
2	110	120	-	64
3	132	130	132	64
4	132	132	132	64
5	132	132	-	-
6	132	-	-	-
Average	121	119	132	64
<b>Total</b>	<b>728</b>	<b>594</b>	<b>264</b>	<b>256</b>

Figure 7.5 demonstrates a comparison of the PRESS MRSI selected volume using both OVS methods. Figure 7.5c is the FLAIR image of a patient with a brain tumor, with superimposed selection regions (cosine-modulated VSS and conventional). Figure 7.5e is a spectrum that is characteristic of tumor that was not included within the conventional OVS scheme.



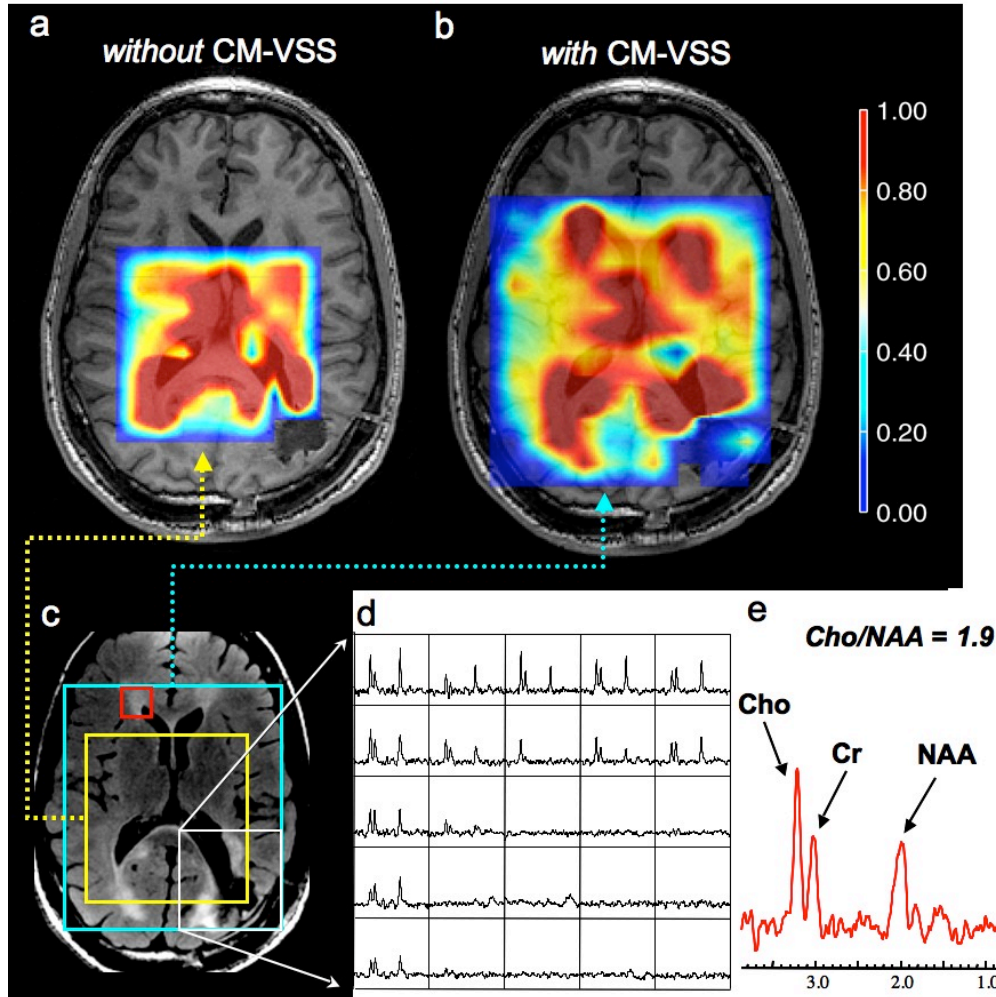


**Figure 7.5: Brain tumor patient with 1H MRSI using both cosine modulate VSS pulse scheme and conventional. (a) T1 with Cho-to-NAA overlay from conventional MRSI selection, (b) and from MRSI using cosine modulated VSS scheme. (c) FLAIR image with selected regions from (a) and (b). (d) Example array of spectra shown from selection within (b) cosine modulated VSS scheme. (e) Spectrum characteristic of abnormal metabolism from voxel outside of conventional coverage.**

### Brain Tumor – Maximum Coverage

Ten patients with diagnosed and treated brain tumors were scanned using the CM-VSS pulses with MRSI. Volume coverage obtained for brain tumor patients were similar to volunteer examinations (Figure 6.6 -

volunteer, 7.6 - patient); coverage was maximized to reach the extent of brain tissue. Figure 7.6 is an example of a grade IV glioma patient that demonstrated extensive disease on T2-weighted images. The neoplasm was restricted – on imaging – to the right hemisphere, and encompassed about 80% of that lobe of brain tissue. Five slices of MRSI data are shown in Figure 7.6 that were acquired to evaluate metabolism in abnormal and normal tissue. Signal-to-noise of the metabolic data was excellent and comparable to volunteer examinations – as shown when comparing Figure 6.6 and 7.6.

The patient in Figure 7.6 was also followed serially through time for a total of four examinations using MRSI with CM-VSS pulses. The extended coverage that was achieved with the CM-VSS pulses sufficiently included enough tissue around the tumor to monitor the progression of the disease. Conventional methods would have not only insufficiently covered the tumor, but also would not have adequately covered enough surrounding tissue to allow the ability to monitor the disease progression. This is a major pitfall of MRSI, and one of the major reasons why it may not be used as frequently to monitor treatment over time in brain tumor patients.

#### *Two- versus Three Dimensional Acquisition*

Although this study has shown favorable results when implementing CM-VSS pulses in a 2D-MRSI acquisition sequence, the OVS designed scheme is not limited to 2D and could be utilized with 3D-MRSI to generate comparable outer volume suppression and data quality. The octagon selection was designed to maximize coverage in the axial dimension, therefore during 2D-slice acquisitions, each slice could be adjusted for

maximal coverage, therefore possibly producing different coverage from one slice to the next. Although there is an advantage in choosing the number of slices desired during the scan, a disadvantage that does exist is the need for continual slice prescription by the operator. Along with the MRSI acquisition time, additional time for higher-order shimming (HOS) may be desired for smaller regions (single slice), therefore lengthening the total scan time because of the additional HOS for each slice.

When data quality was compared between 2D and 3D-MRSI acquisitions, it was noted that 3D in fact did generate higher SNR data. But 2D data was shown to be comparable because of the full sampling of k-space, therefore making the 2D-data quality sufficient for clinical applications. Among the main disadvantages that exist in choosing to utilize CM-VSS pulses in 3D versus 2D, is the limitation that may exist in the axial dimension throughout the 3D volume. Maximal axial coverage during a 3D-acquisition, is ultimately coverage-limited throughout the 3D volume by the slice within the volume that has the least amount of tissue in the axial direction; an example of this may be a slice stretching superiorly in the brain. However, if conventional 3D-methodology is desired for acquisition, the CM-VSS pulse scheme will be superior in data quality when compared to standard conventional OVS techniques.

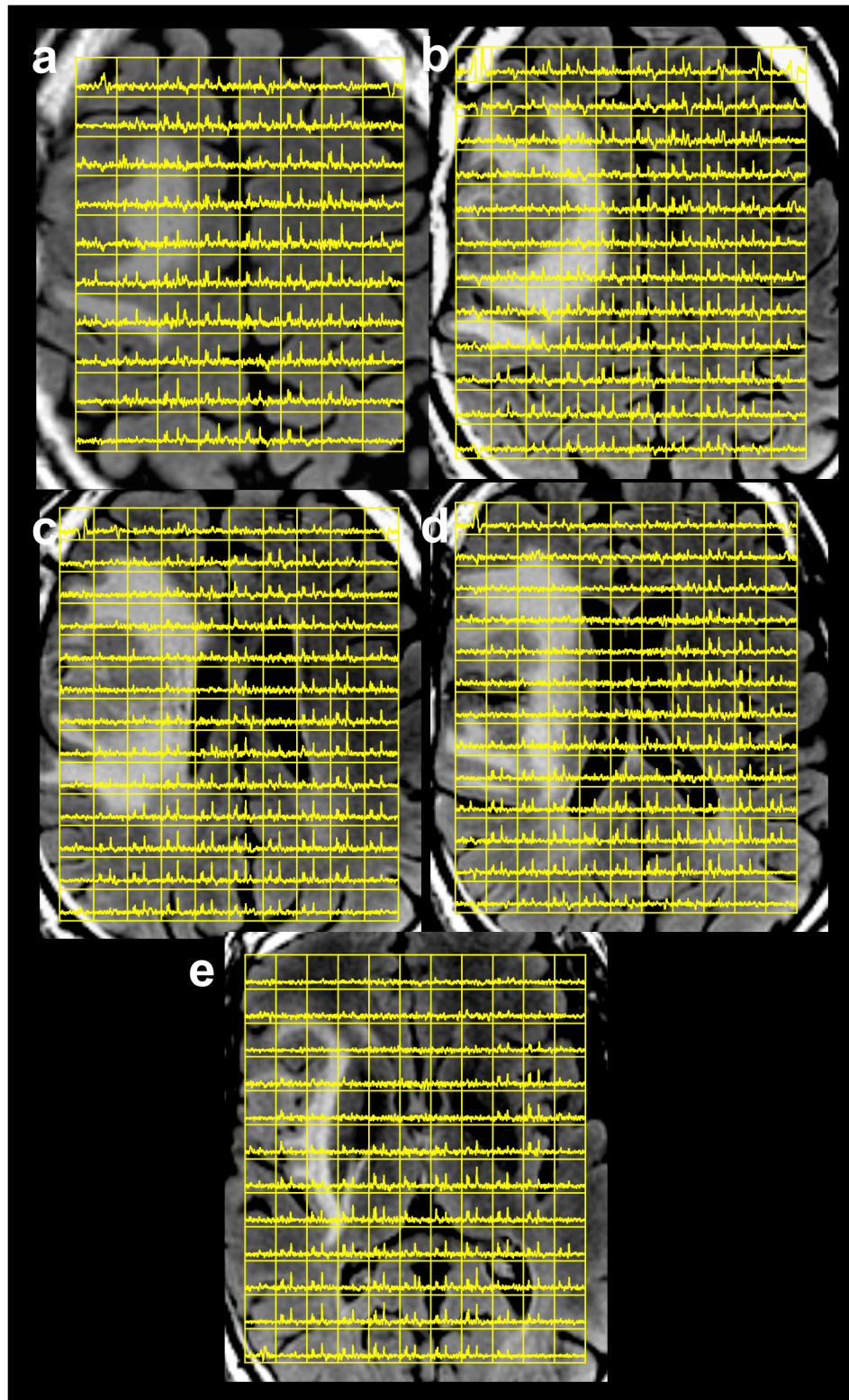


**Figure 7.6 Patient with grade IV glioma. Five slices of MRSI data acquired with CM-VSS pulses shown in yellow overlaid upon FLAIR images. Extensive tumor was adequately covered using CM-VSS.**

## Chapter 8: Summary

---

Magnetic resonance spectroscopic imaging (MRSI) is one of the most technically demanding areas of magnetic resonance imaging. To achieve the necessary performance, current methods employ many of the recent advances in RF pulse design. Extending MRSI methods to higher field strength poses a number of additional challenges, along with a wealth of opportunity, related to the design and use of RF pulses. With the availability of 3 T whole body clinical scanners, the potential exist for improving signal-to-noise ratio (SNR), spatial resolution and/or reduction of scan-time. Brain MRSI exams are a useful clinical tool for treatment planning and monitoring glial disease, but an overriding challenge has been the amount of coverage that could be achieved using this technique. This work attempted to take advantage of the improvement possible at 3 T using MRSI in order to provide metabolic characterization of tissue so that a proper assessment of brain cancer would be feasible *in vivo*.

The low-grade glioma study investigated the biochemical changes over time and evaluated how these changes related to conventional imaging methods. Although we were able to note unique metabolic changes in brain cancer tissue, the study ultimately was limited by SNR and coverage. The subtle changes could have been enhanced with an increase in SNR, making quantification and detection more robust; also, the limited coverage did not allow sufficient data to be acquired in order to truly monitor the metabolic progression of disease.

At 3 T we demonstrated the increase in SNR that would allow the flexibility to obtain high quality MRSI data in a clinically applicable time period, which would provide the necessary metabolic information in order to detect subtle change. Although we were able to address the previous SNR concerns, we still had not been able to address coverage. Higher field systems improved data quality, but it came at the cost of RF power limitations as well as chemical shift misregistration effects. This progressed into the need to reconsider the design of the RF pulses that were being used to see if optimized they could be used to improve the coverage limitation.

The cosine-modulated very selective suppression (CM-VSS) pulse designed was not only optimized for 3 T, to allow more saturation bands in a shorter time period, but it was designed to improve coverage. When tested against the most recent VSS pulses, an improvement in performance was realized in volunteers and patients. With CM-VSS pulses, MRSI could now be feasibly acquired from almost all brain tissue. This improvement will allow improved evaluation of brain tumors using MRSI. The octagon design better mimics the shape of the brain when compared to the conventional rectangular volume making data acquisition more robust.

Future studies should further focus on limiting the amount of interaction that exists during current acquisitions. Even though the fixed CM-VSS pulses in the OVS scheme better mimicked the brain shape, the current method requires the user to graphically place the six saturation bands. Fully automating this process would further minimize acquisition errors.

## References

---

1. Nelson SJ, Graves E, Pirzkall A, Li X, Antiniw Chan A, Vigneron DB, McKnight TR. In vivo molecular imaging for planning radiation therapy of gliomas: an application of 1H MRSI. *J Magn Reson Imaging* 2002;16(4):464-476.
2. Nelson SJ, Vigneron DB, Dillon WP. Serial evaluation of patients with brain tumors using volume MRI and 3D 1H MRSI. *NMR Biomed* 1999;12(3):123-138.
3. Nelson SJ. Imaging of brain tumors after therapy. *Neuroimaging Clin N Am* 1999;9(4):801-819.
4. Tran TK, Vigneron DB, Sailasuta N, Tropp J, Le Roux P, Kurhanewicz J, Nelson S, Hurd R. Very selective suppression pulses for clinical MRSI studies of brain and prostate cancer. *Magn Reson Med* 2000;43(1):23-33.
5. Kleihues P, Louis DN, Scheithauer BW, Rorke LB, Reifenberger G, Burger PC, Cavenee WK. The WHO classification of tumors of the nervous system. *J Neuropathol Exp Neurol* 2002;61(3):215-225; discussion 226-219.
6. Louis DN, Ohgaki H, Wiestler OD, Cavenee WK, Burger PC, Jouvet A, Scheithauer BW, Kleihues P. The 2007 WHO Classification of Tumours of the Central Nervous System. *Acta Neuropathol (Berl)* 2007;114(2):97-109.
7. Pignatti F, van den Bent M, Curran D, Debruyne C, Sylvester R, Therasse P, Afra D, Cornu P, Bolla M, Vecht C, Karim AB. Prognostic factors for survival in adult patients with cerebral low-grade glioma. *J Clin Oncol* 2002;20(8):2076-2084.
8. Prados MD, Scott C, Curran WJ, Jr., Nelson DF, Leibel S, Kramer S. Procarbazine, lomustine, and vincristine (PCV) chemotherapy for anaplastic astrocytoma: A retrospective review of radiation therapy oncology group protocols comparing survival with carmustine or PCV adjuvant chemotherapy. *J Clin Oncol* 1999;17(11):3389-3395.
9. Stupp R, Mason WP, van den Bent MJ, Weller M, Fisher B, Taphoorn MJ, Belanger K, Brandes AA, Marosi C, Bogdahn U, Curschmann J, Janzer RC, Ludwin SK, Gorlia T, Allgeier A, Lacombe D, Cairncross JG, Eisenhauer E, Mirimanoff RO. Radiotherapy plus concomitant and adjuvant temozolomide for glioblastoma. *N Engl J Med* 2005;352(10):987-996.
10. Reifenberger J, Reifenberger G, Liu L, James CD, Wechsler W, Collins VP. Molecular genetic analysis of oligodendroglial tumors shows preferential allelic deletions on 19q and 1p. *Am J Pathol* 1994;145(5):1175-1190.
11. Cairncross JG, Ueki K, Zlatescu MC, Lisle DK, Finkelstein DM, Hammond RR, Silver JS, Stark PC, Macdonald DR, Ino Y,

- Ramsay DA, Louis DN. Specific genetic predictors of chemotherapeutic response and survival in patients with anaplastic oligodendrogliomas. *J Natl Cancer Inst* 1998;90(19):1473-1479.
12. Shaw EG, Scheithauer BW, O'Fallon JR, Tazelaar HD, Davis DH. Oligodendrogliomas: the Mayo Clinic experience. *J Neurosurg* 1992;76(3):428-434.
  13. McPherson CM, Sawaya R. Technologic advances in surgery for brain tumors: tools of the trade in the modern neurosurgical operating room. *J Natl Compr Canc Netw* 2005;3(5):705-710.
  14. Vives KP, Piepmeier JM. Complications and expected outcome of glioma surgery. *J Neurooncol* 1999;42(3):289-302.
  15. Kesari S, Ramakrishna N, Sauvageot C, Stiles CD, Wen PY. Targeted molecular therapy of malignant gliomas. *Curr Neurol Neurosci Rep* 2005;5(3):186-197.
  16. Sawaya R. Chairman's reflection on the past, present and future of neurosurgical oncology. *J Neurooncol* 2004;69(1-3):19-23.
  17. Gilman A. The initial clinical trial of nitrogen mustard. *Am J Surg* 1963;105:574-578.
  18. Walker MD, Hurwitz BS. BCNU (1,3-bis(2-chloroethyl)-1-nitrosourea; NSC-409962) in the treatment of malignant brain tumor--a preliminary report. *Cancer Chemother Rep* 1970;54(4):263-271.
  19. Wilson CB, Boldrey EB, Enot KJ. 1,3-bis (2-chloroethyl)-1-nitrosourea (NSC-409962) in the treatment of brain tumors. *Cancer Chemother Rep* 1970;54(4):273-281.
  20. Levin VA. A pharmacologic basis for brain tumor chemotherapy. *Semin Oncol* 1975;2(1):57-61.
  21. Neuwelt EA. Mechanisms of disease: the blood-brain barrier. *Neurosurgery* 2004;54(1):131-140; discussion 141-132.
  22. Bottomley PA. Spatial localization in NMR spectroscopy in vivo. *Ann N Y Acad Sci* 1987;508:333-348.
  23. Haase A, Frahm J, Hanicke W, Matthaei D. 1H NMR chemical shift selective (CHESS) imaging. *Phys Med Biol* 1985;30(4):341-344.
  24. McKnight TR, Noworolski SM, Vigneron DB, Nelson SJ. An automated technique for the quantitative assessment of 3D-MRSI data from patients with glioma. *J Magn Reson Imaging* 2001;13(2):167-177.
  25. McKnight TR, von dem Bussche MH, Vigneron DB, Lu Y, Berger MS, McDermott MW, Dillon WP, Graves EE, Pirzkall A, Nelson SJ. Histopathological validation of a three-dimensional magnetic resonance spectroscopy index as a predictor of tumor presence. *J Neurosurg* 2002;97(4):794-802.
  26. Chan AA, Lau A, Pirzkall A, Chang SM, Verhey LJ, Larson D, McDermott MW, Dillon WP, Nelson SJ. Proton magnetic resonance spectroscopy imaging in the evaluation of patients



- undergoing gamma knife surgery for Grade IV glioma. *J Neurosurg* 2004;101(3):467-475.
27. Nelson SJ. Magnetic resonance spectroscopic imaging. Evaluating responses to therapy for gliomas. *IEEE Eng Med Biol Mag* 2004;23(5):30-39.
  28. McBride DQ, Miller BL, Nikas DL, Buchthal S, Chang L, Chiang F, Booth RA. Analysis of brain tumors using <sup>1</sup>H magnetic resonance spectroscopy. *Surg Neurol* 1995;44(2):137-144.
  29. Fulham MJ, Bizzi A, Dietz MJ, Shih HH, Raman R, Sobering GS, Frank JA, Dwyer AJ, Alger JR, Di Chiro G. Mapping of brain tumor metabolites with proton MR spectroscopic imaging: clinical relevance. *Radiology* 1992;185(3):675-686.
  30. Preul MC, Caramanos Z, Collins DL, Villemure JG, Leblanc R, Olivier A, Pokrupa R, Arnold DL. Accurate, noninvasive diagnosis of human brain tumors by using proton magnetic resonance spectroscopy. *Nat Med* 1996;2(3):323-325.
  31. Preul MC, Caramanos Z, Leblanc R, Villemure JG, Arnold DL. Using pattern analysis of in vivo proton MRSI data to improve the diagnosis and surgical management of patients with brain tumors. *NMR Biomed* 1998;11(4-5):192-200.
  32. Dowling C, Bollen AW, Noworolski SM, McDermott MW, Barbaro NM, Day MR, Henry RG, Chang SM, Dillon WP, Nelson SJ, Vigneron DB. Preoperative proton MR spectroscopic imaging of brain tumors: correlation with histopathologic analysis of resection specimens. *AJNR Am J Neuroradiol* 2001;22(4):604-612.
  33. Li X, Lu Y, Pirzkall A, McKnight T, Nelson SJ. Analysis of the spatial characteristics of metabolic abnormalities in newly diagnosed glioma patients. *J Magn Reson Imaging* 2002;16(3):229-237.
  34. Gonen O, Gruber S, Li BS, Mlynarik V, Moser E. Multivoxel 3D proton spectroscopy in the brain at 1.5 versus 3.0 T: signal-to-noise ratio and resolution comparison. *AJNR Am J Neuroradiol* 2001;22(9):1727-1731.
  35. Gruber S, Mlynarik V, Moser E. High-resolution 3D proton spectroscopic imaging of the human brain at 3 T: SNR issues and application for anatomy-matched voxel sizes. *Magn Reson Med* 2003;49(2):299-306.
  36. Li Y, Osorio JA, Ozturk E, et al. Considerations in applying 3-D PRESS <sup>1</sup>H MRSI for studies of patients with brain tumors at 3T relative to 1.5T. 2005.
  37. Gruetter R, Weisdorf SA, Rajanayagan V, Terpstra M, Merkle H, Truwit CL, Garwood M, Nyberg SL, Ugurbil K. Resolution improvements in in vivo <sup>1</sup>H NMR spectra with increased magnetic field strength. *J Magn Reson* 1998;135(1):260-264.
  38. Hetherington HP, Pan JW, Chu WJ, Mason GF, Newcomer BR. Biological and clinical MRS at ultra-high field. *NMR Biomed* 1997;10(8):360-371.

39. Jeun SS, Kim MC, Kim BS, Lee JM, Chung ST, Oh CH, Lee SY, Choe BY. Assessment of malignancy in gliomas by 3T 1H MR spectroscopy. *Clin Imaging* 2005;29(1):10-15.
40. Wald LL, Moyher SE, Day MR, Nelson SJ, Vigneron DB. Proton spectroscopic imaging of the human brain using phased array detectors. *Magn Reson Med* 1995;34(3):440-445.
41. Wright SM, Wald LL. Theory and application of array coils in MR spectroscopy. *NMR Biomed* 1997;10(8):394-410.
42. Xu D, Chen AP, Cunningham C, Osorio JA, Nelson SJ, Vigneron DB. Spectroscopic imaging of the brain with phased-array coils at 3.0 T. *Magn Reson Imaging* 2006;24(1):69-74.
43. Frayne R, Goodyear BG, Dickhoff P, Lauzon ML, Sevick RJ. Magnetic resonance imaging at 3.0 Tesla: challenges and advantages in clinical neurological imaging. *Invest Radiol* 2003;38(7):385-402.
44. Schwindt W, Kugel H, Bachmann R, Kloska S, Allkemper T, Maintz D, Pfeleiderer B, Tombach B, Heindel W. Magnetic resonance imaging protocols for examination of the neurocranium at 3 T. *Eur Radiol* 2003;13(9):2170-2179.
45. Kim DS, Garwood M. High-field magnetic resonance techniques for brain research. *Curr Opin Neurobiol* 2003;13(5):612-619.
46. Srinivasan R, Vigneron D, Sailasuta N, Hurd R, Nelson S. A comparative study of myo-inositol quantification using LCmodel at 1.5 T and 3.0 T with 3 D 1H proton spectroscopic imaging of the human brain. *Magn Reson Imaging* 2004;22(4):523-528.
47. Nelson SJ. Analysis of volume MRI and MR spectroscopic imaging data for the evaluation of patients with brain tumors. *Magn Reson Med* 2001;46(2):228-239.
48. Li X, Vigneron DB, Cha S, Graves EE, Crawford F, Chang SM, Nelson SJ. Relationship of MR-derived lactate, mobile lipids, and relative blood volume for gliomas in vivo. *AJNR Am J Neuroradiol* 2005;26(4):760-769.
49. Pruessmann KP, Weiger M, Scheidegger MB, Boesiger P. SENSE: sensitivity encoding for fast MRI. *Magn Reson Med* 1999;42(5):952-962.
50. Barker PB, Hearshen DO, Boska MD. Single-voxel proton MRS of the human brain at 1.5T and 3.0T. *Magn Reson Med* 2001;45(5):765-769.
51. Duyn JH, Gillen J, Sobering G, van Zijl PC, Moonen CT. Multisection proton MR spectroscopic imaging of the brain. *Radiology* 1993;188(1):277-282.
52. Posse S, Schuknecht B, Smith ME, van Zijl PC, Herschkowitz N, Moonen CT. Short echo time proton MR spectroscopic imaging. *J Comput Assist Tomogr* 1993;17(1):1-14.
53. Shungu DC, Glickson JD. Band-selective spin echoes for in vivo localized 1H NMR spectroscopy. *Magn Reson Med* 1994;32(3):277-284.

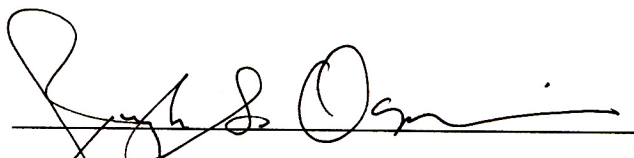
54. Singh S RB, Henkelman RM. Projection presaturation: A fast and accurate technique for multidimensional spatial localization. *Journal of Magnetic Resonance* 1990;87:567-583.
55. Osorio JA O-IE, Xu D, Cha S, Chang S, Berger MS, Vigneron D, Nelson SJ. 3D 1H MRSI of brain tumors at 3.0 Tesla using an 8-channel phased array head coil. IN PRESS - *Journal of Magnetic Resonance Imaging* 2007.
56. Li Y, Osorio JA, Ozturk-Isik E, Chen AP, Xu D, Crane JC, Cha S, Chang S, Berger MS, Vigneron DB, Nelson SJ. Considerations in applying 3D PRESS H-1 brain MRSI with an eight-channel phased-array coil at 3 T. *Magn Reson Imaging* 2006;24(10):1295-1302.
57. Pauly J LRP, Nishimura D, Macovski A. Parameter relations for the Shinnar-Le Roux selective excitation pulse design algorithm NMR imaging. *IEEE Trans Med Imaging USA* 1991;10:53-65.
58. Pickup S, Popescu M. Efficient design of pulses with trapezoidal magnitude and linear phase response profiles. *Magn Reson Med* 1997;38(1):137-145.
59. Shinnar M. Reduced power selective excitation radio frequency pulses. *Magn Reson Med* 1994;32(5):658-660.
60. Le Roux P, Gilles RJ, McKinnon GC, Carlier PG. Optimized outer volume suppression for single-shot fast spin-echo cardiac imaging. *J Magn Reson Imaging* 1998;8(5):1022-1032.

**Publishing Agreement**

*It is the policy of the University to encourage the distribution of all theses and dissertations. Copies of all UCSF theses and dissertations will be routed to the library via the Graduate Division. The library will make all theses and dissertations accessible to the public and will preserve these to the best of their abilities, in perpetuity.*

***Please sign the following statement:***

*I hereby grant permission to the Graduate Division of the University of California, San Francisco to release copies of my thesis or dissertation to the Campus Library to provide access and preservation, in whole or in part, in perpetuity.*

  
\_\_\_\_\_  
Author Signature

09-05-2007

Date